Role of Microstructure in Wear Resistance of Chromium Carbide Overlay

by

Jing Li

A thesis submitted in partial fulfillment of the requirements for the degree of

Doctor of Philosophy

in

Materials Engineering

Department of Chemical and Materials Engineering

University of Alberta

Abstract

Iron-based alloy overlays are extensively utilized in industry to increase the longevity of components that are exposed to wear and corrosion. Welding is a common overlay technique due to its cost-effectiveness and high efficiency. To expedite the overlay design and development process, the button melting method has been compared with wire fabrication and welding. Both methods produce similar microstructures and hardness for the same overlay alloy. Using button melting as a replacement for wire fabrication is feasible. However, button melting does not result in dilution from the base metal, and the microstructure comprises more directionally solidified M_7C_3 grains due to the predominant directional cooling. Moreover, button melting produces faster cooling rates that promote the formation of martensite in the steel matrix.

An accelerated method for alloy design was proposed using a combination of button melting and machine learning. By leveraging existing data, a closed-loop design process was developed that enables the prediction of future experiments and suggests new ones. Through an active database, the influence of Nb, V, and Ti on the hardness of the overlay was established. XRD analysis revealed that Nb promotes the formation of austenite in the matrix, while Ti fosters the formation of martensite. The effectiveness of this method is demonstrated by successfully predicting the combined effects of carbide formers on overlay hardness. This showcases the potential of machine learning in the design of chromium carbide overlays.

The microstructures of two different overlays, namely an as-welded chromium carbide overlay and a novel Fe-Cr-C-B overlay with multiple alloying elements, have been thoroughly examined. The microstructure of the chromium carbide overlay consists of large primary carbides (M_7C_3) along with the presence of austenite and carbide eutectic phases. In contrast, the microstructure of the new overlay is composed of granular primary carbides (MX-type) containing elements such as Nb, Ti, and Mo, along with a dendritic structure of δ-ferrite/austenite. Eutectic phases of austenite and M_2B boride (M = Fe and Cr) are also observed. The overlay's high hardness is attributed to the presence of fine MX-type hard particles, as well as the refined eutectic and matrix microstructure. The non-equilibrium solidification process responsible for the complex microstructure is discussed utilizing Thermo-Calc.

By adding small quantities (0, 0.1, 0.5, and 1 wt.%) of aluminum to a chromium carbide overlay, the size of the large M_7C_3 carbides was effectively reduced. Comparative scratch tests revealed multiple cracks in the large primary M_7C_3 carbides of the 0% aluminum sample, while fewer cracks were observed in the refined M_7C_3 carbides. This refinement process is attributed to the heterogeneous nucleation of carbides on Al_2O_3, which forms prior to M_7C_3 nucleation. The presence of aluminum is found to expedite the growth time of primary M_7C_3 carbides by elevating the eutectic temperature. In terms of mechanical properties, the addition of 1% aluminum resulted in a slightly softer overlay. This is attributed to a decrease in the amount of martensite and an increase in retained austenite within the overlay matrix. Notably, the proposed approach of incorporating a small quantity of aluminum offers a novel method for refining primary M_7C_3 carbides without introducing new hard phases.

Preface

The work presented in the current thesis is conducted by Jing Li under supervision of Dr. Leijun Li at the Department of Chemical and Materials Engineering, University of Alberta. This work has been funded by Mitacs Accelerate Program (IT18992). Parts of the work have been published in peer reviewed journals.

Part of Chapter 2 has been published as Li, J., Wang, Y., Lyu, Z. Sharm, N., Choudhury, S. & Li, L. Fracture of Ni-Cr-Si-B thermal sprayed and fused reciprocating pump rods during straightening. Engineering Failure Analysis 127, 105576 (2021).

Part of Chapter 4 has been published as Li, J., Kannan, R., Shi, M., Lyu, Z. & Li, L. Viability of button melting for accelerated development of chromium carbide overlay. Materials Letters 278, 128455 (2020).

Part of Chapter 5 has been published as Li, J., Cao, B., Chen, H. & Li, L. Accelerated design of chromium carbide overlays via design of experiment and machine learning. Materials Letters 333, 133672 (2023).

Part of Chapter 6 has been published as Li, J., Kannan, R., Shi, M. & Li, L. Solidified Microstructure of Wear-Resistant Fe-Cr-C-B Overlays. Metallurgical and Materials Transactions B 51, 1291–1300 (2020).

Part of Chapter 7 has been published as Li, J., Lyu, Z., Shi, M. & Li, L. Aluminum inoculated overlay microstructure for enhanced scratch resistance. Tribology International

185, 108549 (2023).

To my daughter Larina C. Li, future offspring, and researchers who may read this thesis:
I lived, loved, led, and devoted.

Acknowledgements

I would like to express my sincere gratitude and appreciation to my supervisor, Dr. Leijun Li, for his invaluable guidance and unwavering support throughout the process of completing this thesis. Dr. Li's steadfast support and encouragement have been instrumental in overcoming challenges and achieving significant milestones in my research. I am truly grateful for his mentorship, which has not only shaped my academic and professional development but has also instilled in me a deep passion for the field. Without his guidance, expertise, and faith in me, this thesis would not have been possible.

I would like to express my heartfelt gratitude to Dr. Hani Henien, Dr. Douglas Ivey, Dr. Dongyang Li, and Dr. Hao Zhang for their support in providing lab equipment and engaging in helpful discussions regarding my coursework, research, and career development. I also thank Dr. Qi Liu, Dr. Jing Liu, Dr. Gary Fisher on the committee for providing valuable feedback. I am also grateful for the technical assistance provided by the nanoFAB staff, specifically Dr. Shihong Xu.

I extend my sincere thanks to my colleagues in our group: Dr. Rangasayee Kannan, Dr. Yiyu Wang, Mr. Neil Anderson, Ms. Rebekah Bannister, Mr. Lulu Guo, Dr. Dashuang Liu, Mr. Lieduo Yang, Dr. Minghao Shi, Ms. Yajing Wang, Dr. Nitin Saini, Dr. Nitin Sharma, Mr. Suvan Dev Choudhury, Mr. Zhe Lyu, Mr. Ravikiran Kopparthi, Dr. Waris Nawaz Khan, and Mr. Zachary Tervonen. They have not only been colleagues but also collaborators and friends.

I am deeply grateful for the support I received from my friends, Dr. Lei Wang, Ms. Yue Wu, Mr. Le Zhang, Ms. Wenxia Wan, Dr. Fenglin Liu, Dr. Cong Jin, Mr. Liwei Fu, and Ms. Chunyan Wu. I cherish the memories of the time we spent together in Edmonton.

The unconditional love and support from my family have always been an invaluable asset to me. I would like to express my gratitude to my parents, Yundong Li and Suling Zhao, as well as my sister, Chao Li, for their patience and tolerance.

Lastly, I want to express my utmost appreciation to my wife, Dr. Bing Cao. Starting this Ph.D. journey required a significant commitment, and without her unwavering support, it would not have been possible. We have been together for 17 years, and I eagerly anticipate the exciting future that lies ahead. This journey started before my daughter, Larina Li, was born. You are the most wonderful gift I could ever hope for. Thank you for always supporting me and love you forever!

Table of Contents

List of Tables

List of Figures

Chapter 1

Introduction

Alberta possesses the world's second-largest reserve of oil sands, and as demand for oil continues to increase until 2050, the need for efficient and environmentally friendly extraction methods becomes paramount. However, the current extraction process involves large-scale excavation of the sand, which is then crushed, mixed with water and other additives to form a slurry, and piped to extraction plants for bitumen. This entire process induces severe material loss to equipment due to wear and corrosion. In fact, some data shows that in the Fort McMurray region alone, four commercial oil sands mining operations spent approximately $5 billion on operating costs to replace and maintain equipment. A significant portion of this cost is attributed to material loss due to wear and corrosion [1].

To address this issue, wear-resistant materials have become increasingly popular, with wear-resistant overlays being an integral part of machines and pipelines exposed to wear and corrosion. In order to prevent wear in situations where abrasion is involved, carbides, which are material-carbon compounds with high hardness, are often preferred over metals. However, pure carbides do not perform well under impact loading due to their poor fracture resistance, and they cannot be easily formed into complex shapes or components. Various methods have been developed to apply wear-resistant materials as a hardfacing in which the iron-based overlay (Fe-Cr-C) applied by welding process has been widely utilized because of its low cost and high efficiency.

The examination of cutting-edge welding overlay wire technology reveals that achieving the desired levels of wear resistance, corrosion resistance, and crack resistance hinges on achieving an optimal structure and composition of primary and eutectic carbides. However, understanding the fundamental principles governing carbide type and morphology control in welding overlays remains challenging. This complexity arises from complicated phase transformations, interactions between alloying elements, process variables, and the resultant material performance. In the realm of complex welding overlay alloys involving multi-component carbides and borides, there is a scarcity of well-established guidance and published knowledge.

The objective of this work is to address the technical challenges outlined above through an examination of minor elements, including B, Nb, V, Ti, and Al in relation to chromium carbides during the welding process of the Fe-Cr-C system. The primary focus will be on exploring the chemistry, structure, and mechanical properties that pertain to the resulting overlay microstructure and performance.

Chapter 2

Literature Review

2.1 Wear resistant materials

The selection of the appropriate wear-resistant material for a specific application depends on several factors, including the type and severity of wear, the operating environment, and the properties required for the coating. Some common types of wear-resistant materials include metals, ceramics, and polymers.

Metal coatings are often used for applications where impact and abrasion resistance are required. These coatings can be applied using a variety of spray processes, including arc spraying and HVOF spraying. Common metal coatings include nickel-chromium alloys, stainless steel, and tungsten carbide. Ceramic coatings are known for their excellent wear resistance and high hardness, making them ideal for applications where abrasion and erosion are major concerns. Some common types of ceramic coatings include aluminum oxide, titanium oxide, and zirconia. Polymer coatings are commonly used for applications where wear resistance and chemical resistance are both important. These coatings can be applied using a variety of spray processes. Common polymer coatings include polyurethane, epoxy, and fluoropolymers. This section focusses on the ceramic reinforced metal coating applied by the welding process.

2.2 Application process

One method for combining the excellent wear properties of carbides with the formability of metals is using weld-deposited overlays. These overlays combine the abrasion resistance of carbides with the toughness of a metal matrix and are applied on top of structural steels. These iron-based wear-resistant alloys, deposited using various arc-welding processes, are widely used due to their high flexibility, productivity, and lower cost. The other methods for applying overlays involve using thermal spray processes such as flame spray, high velocity oxygen fuel (HVOF), plasma spray, and cold spray. [2,3].

2.2.1 Applications by thermal spray process

One method of applying wear-resistant overlays is through the spray process, which involves depositing a thin layer of material onto the surface of a substrate using a spray gun. The spray process is a cost-effective and efficient way to apply wear-resistant materials to a variety of substrates, including metals, plastics, ceramics, and composites [3].

There are several types of spray processes used in the application of wear-resistant materials, including flame power spray, plasma spraying, high-velocity oxy-fuel (HVOF) spraying, and arc spraying. Each process has its own unique characteristics and advantages, and the choice of spray process depends on the specific application and the properties required for the coating. Flame powder spray is a thermal spray process used to apply coatings that resist wear and corrosion to various surfaces. This technique involves heating a powder material using a fuel gas and oxygen flame, and then accelerating the molten droplets of the powder material onto a substrate using compressed air or inert gas [4,5]. The flame powder spray process is particularly useful for depositing wear-resistant coatings on large and complex surfaces, including those that are difficult to access using other coating techniques. The coatings produced by flame powder spray are characterized by their excellent adhesion, high density, and low porosity, which contribute to their exceptional resistance to wear and corrosion. As a result, flame powder spray has become an important industrial process in many sectors, including aerospace, automotive, and manufacturing industries. Figure 2.1 shows a scanning electron microscope (SEM) secondary electrons (SE) image of a flame powder spray-and-fused Ni-Cr-Si-B coating.

Flame powder coatings may have higher levels of porosity than HVOF coatings, which can affect their performance in some applications [6]. However, the porosity of flame powder coatings can be minimized by optimizing the spray parameters, such as the particle size, velocity, and temperature of the powder material. The percentage of porosity in flame powder coatings can vary widely, from less than 1% to as high as 10%, depending on the specific application requirements and the spray process parameters used [6]. Figure 2.2 shows some SEM energy dispersive X-ray spectroscopy (EDX) images of the cross-section of the Ni-Cr-Si-B thermal sprayed and fused coating by flame powder thermal spray. As expected from the chemical composition of the spray metal, the coating is rich in Ni, Cr, and Si, together with a small concentration of Mn, while the base steel is rich in Fe as shown in Figures 2.2b to f. Light elements such as boron and carbon are not easy to detect due to the nature of EDX. A crack formed during the manufacturing process can be seen in Figure 2.2a [7].

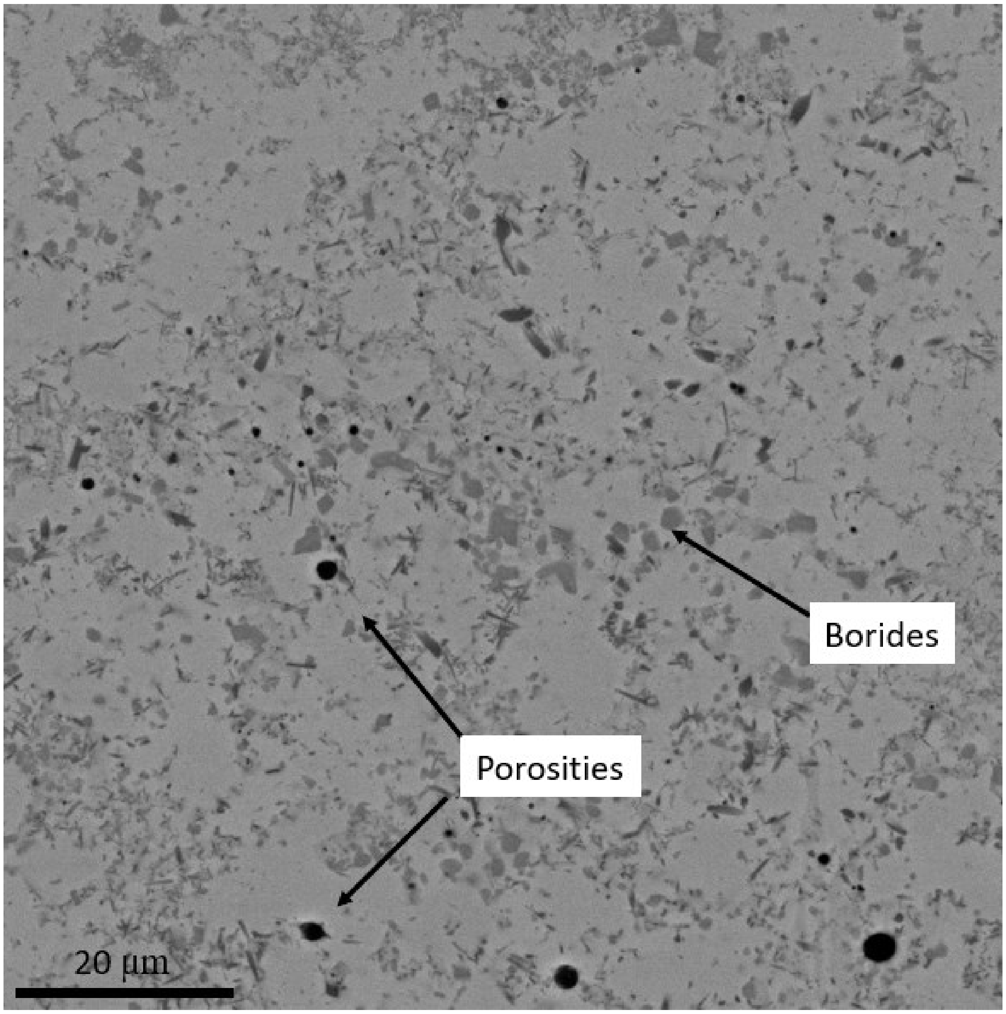

Figure 2.1: SEM SEM image of flame powder sprayed-and-fused Ni-Cr-Si-B coating.

Plasma spraying is a commonly used spray process that involves the use of a high-temperature plasma arc to melt and atomize the coating material. The molten material is then sprayed onto the substrate, where it solidifies to form a dense and highly adherent coating. Plasma spraying is particularly useful for applying wear-resistant materials such as ceramics, which are known for their high hardness and resistance to abrasion.

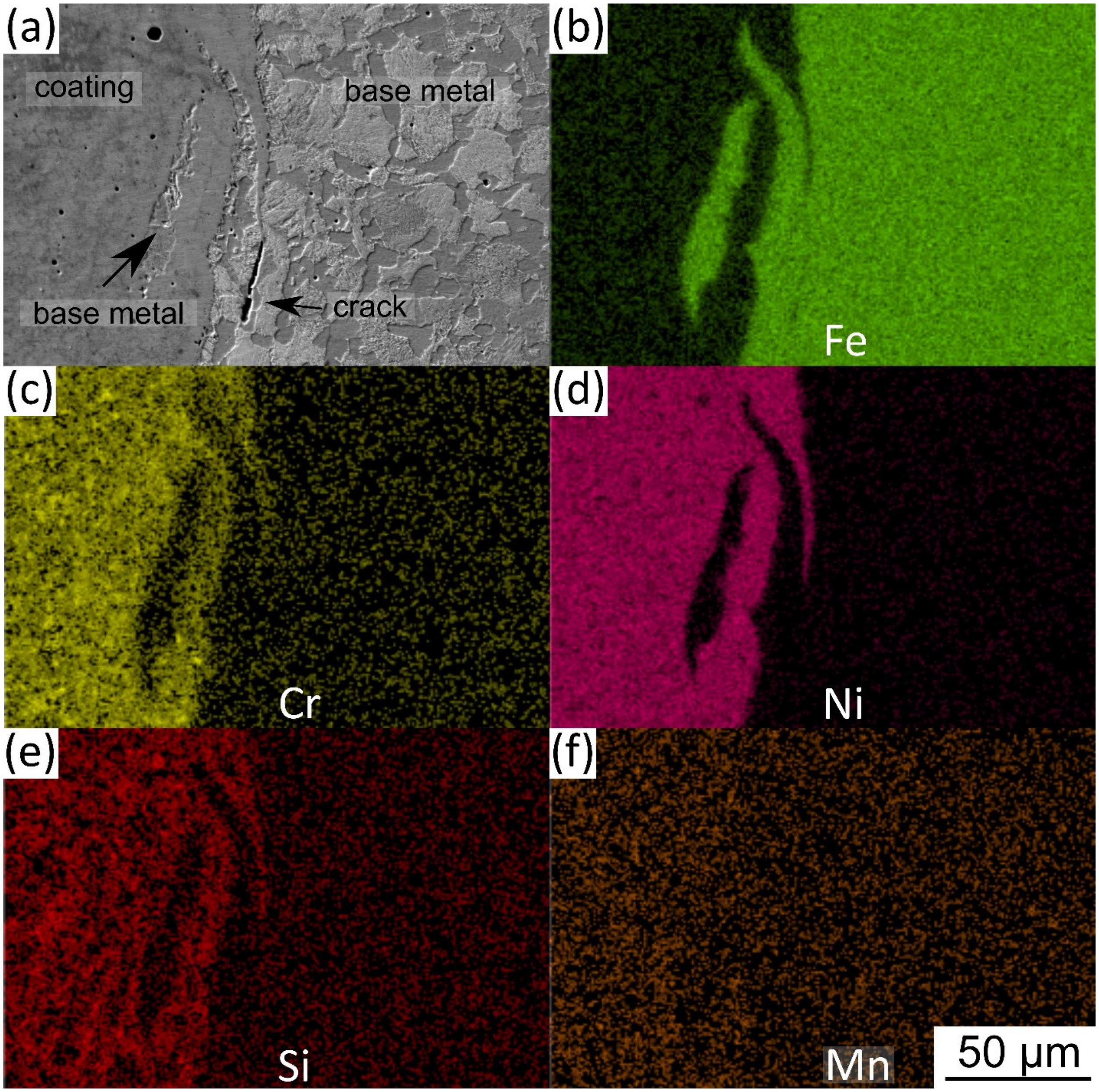

Figure 2.2: SEM/EDX images of the cross-section of the Ni-Cr-Si-B thermal sprayed and fused coating and base material interface. (a) secondary electron image and (b) to (f) are EDX mapping of various elements [7].

Arc spraying is a spray process that uses an electric arc to melt the coating material, which is then atomized and propelled onto the substrate using compressed air. Arc spraying is a cost-effective and versatile method of applying wear-resistant coatings to a variety of substrates, including metals, plastics, and composites.

HVOF spraying is another popular spray process that uses a high-velocity gas stream to propel the coating material onto the substrate. This process produces coatings with high bond strength and density, making it ideal for applications where wear resistance is critical. HVOF coatings are commonly used in the aerospace, automotive, and oil and gas industries. HVOF coatings are typically characterized by their high density, low porosity, and excellent adhesion to the substrate, making them ideal for applications that require high wear resistance and corrosion protection. The porosity of HVOF coatings is typically less than 1% and can be as low as 0.1%, which makes them nearly impermeable to gases and liquids.

2.2.2 Applications by welding process

2.2.2.1 Nickel tungsten carbide (NiWC) overlay

Nickel tungsten carbide (NiWC) wear resistant materials are a type of composite material that combines the properties of tungsten carbide and nickel. This material is known for its exceptional strength, hardness, and wear resistance, making it ideal for a wide range of applications [8]. NiWC wear resistant materials have several unique properties that make them highly desirable for a range of applications. One of the most notable properties of NiWC is its exceptional hardness. This material is known to have a hardness of up to 70 HRC, which makes it highly resistant to wear and deformation [9]. Additionally, NiWC has a high resistance to corrosion, oxidation, and erosion, making it suitable for use in harsh environments [10]. Another important property of NiWC wear resistant materials is their high thermal conductivity [11]. This allows the material to dissipate heat more effectively, which makes it ideal for use in high-temperature applications. Furthermore, NiWC has a low coefficient of thermal expansion, which helps to maintain its dimensional stability even in extreme temperature environments [12].

Due to its exceptional properties, NiWC wear resistant materials are used in a wide range of applications. One of the most common applications of NiWC is in the production of cutting tools [13–15]. These tools are used in a variety of industries, including aerospace, automotive, and manufacturing, to cut and shape materials such as metals, ceramics, and composites. In the mining industry, NiWC wear resistant materials are used to produce wear-resistant components such as drill bits, picks, and other mining tools [16]. These components are subjected to extreme conditions and require exceptional durability and wear resistance. NiWC wear resistant materials are also used in the production of pump components, valve components, and other industrial equipment that require high wear resistance and durability. Plasma transferred arc welding (PTAW) is commonly used for the deposition of these coatings, but for specific components or in-field repairs, gas metal arc welding (GMAW) techniques are utilized [17–19].

While NiWC wear resistant materials offer exceptional properties and performance, there are some limitations to their use. One of the main limitations is their cost. NiWC is a relatively expensive material, which can make it less cost-effective for certain applications. Another limitation of NiWC is its brittleness. NiWC is a very hard and rigid material, which can make it more prone to cracking and fracturing under certain conditions. This can be a limiting factor in some applications where flexibility and toughness are required. Besides, the heat generated during PTAW deposition can cause tungsten carbide particles to dissolve into the metal matrix, leading to reduced corrosion and wear resistance performance and increased brittleness [20–22]. However, WC is more chemically stable than W_2C and less susceptible to this effect.

2.2.2.2 Iron-based chromium carbide overlay (CCO)

Iron-based wear-resistant overlays, in particular, chromium carbide overlays (CCO) are derived from the Fe-Cr-C ternary system. This system offers a wide range of chemical compositions that can be tailored to achieve specific mechanical properties and performance characteristics. The resulting overlays are known for their exceptional hardness, toughness, and resistance to wear and corrosion. This makes them ideal for use in high-stress environments where components are exposed to abrasive or corrosive materials. In this context, this system has become a popular choice for industries such as mining, construction, and manufacturing, where equipment longevity and reliability are critical [23,24].

CCOs are typically applied using arc welding processes, which can be done manually or through automated methods for larger components. Compared to other wear-resistant materials, such as nickel tungsten carbide-based overlays, CCOs are a more cost-effective option. Hence, they are often used for high-volume, larger-scale applications such as wear-plates for truck beds and piping in hydro transport operations. The overlays can be deposited in single or multiple passes, with the subsequent pass to compensate for the hardfacing alloy's dilution with the base material or the previous pass. This also enables the subsequent pass to form large, acicular carbides that are necessary for wear resistance. However, the overlays may contain transverse cracking caused by the weld pool's contraction upon cooling, commonly referred to as "relief" or "check" cracking. Figure 2.3(a) shows a 5’ × 10’ mild steel plate coated by the CCO. The relief cracks can be clearly seen on Figure 2.3(b).

Figure 2.3: (a) chromium carbide overlay on a 5’ × 10’ mild steel plate produced by submerged arc welding and (b) details of the relief cracks on the same plate.

The CCO typically comprises 8-40 wt-% Cr and 2-5 wt-% C, as reported in several references. Three distinct categories of microstructure are typically seen namely hypoeutectic, eutectic, and hyper-eutectic depending on the chemical composition. The microstructures of these categories exhibit significant differences in their mechanical properties. The hypoeutectic overlay, containing smaller quantity of alloying elements, has a primary solidification matrix of austenite, and minimal eutectic carbides. It is known for its excellent resistance to weld cracking and superior corrosion resistance, although it tends to have relatively lower wear resistance. On the other hand, the hypereutectic overlay has the highest amount of alloying elements and is more expensive. Its major phase is a primary solidified carbide, typically M_7C_3 type, with austenite grains as one eutectic component and often networked carbide as the other eutectic component.

Researchers have proposed two crystal structures for the M_7C_3 carbides. Initially, it was thought to have a hexagonal lattice due to its hexagonal shape and XRD results [25–28]. However, so other studies suggest that an orthorhombic lattice may be more accurate [29–33]. In this thesis, both crystal structures are accepted. M_7C_3 carbide in CCO can vary depending on the processing parameters and composition of the material. However, in general, the primary M_7C_3 carbides in CCO have a plate-like or acicular (needle-like) morphology, or have a so called “pencil” shape. Figure 2.4 illustrates the growth mechanism of the hexaganol M_7C_3 by Zhang et al [34].

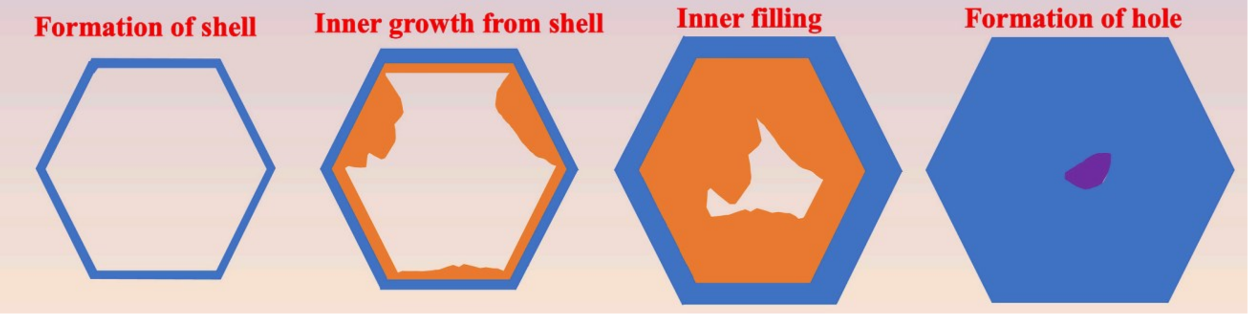

Figure 2.4: The schematic model illustrates the special growth processes of primary M_7C_3 carbide [34].

The growth of primary M_7C_3 carbides can be described in two stages. Initially, a thin hexagonal shell with a thickness of approximately 1 μm is formed rapidly. Subsequently, the interior is filled gradually through epitaxial growth from the inner wall of the shell. However, the diffusion of atoms within the carbide tube is limited, resulting in the formation of structural defects such as cavities [34].

This morphology is a result of the eutectic solidification process during which the primary M_7C_3 carbides nucleate and grow from the liquid phase. The morphology of the primary carbides can have a significant impact on the properties of the CCO, such as wear resistance and toughness. In some cases, the primary M_7C_3 carbides can be modified or refined through post-processing treatments to improve the material's properties. However, in the industrial settings, it is more common to modify the carbide morphlogy by adding other elements.

Some other common carbides that are commonly seen in the CCO include $M_{23}C_6$ and M_3C_2. The typical crystal structure of the three common carbides is shown in Figure 2.5. The transition of Cr to Cr_3C_2 with the increasing concentration of C is represented as below.

$$Cr \xrightarrow{15-20\%\, C} Cr_{23}C_6 \xrightarrow{20-30\%\, C} Cr_7C_3 \xrightarrow{30-45\%\, C} Cr_3C_2$$

Figure 2.5 also shows that $Cr_{23}C_6$ has cubic symmetry with $a = b = c$ and $\alpha = \beta = \gamma = 90^\circ$ while Cr_7C_3 and Cr_3C_2 have orthorhombic symmetry with $a \neq b \neq c$ and $\alpha = \beta = \gamma = 90^\circ$ [33]. It has been found that the carbide transformation enhances the coalescence process of rod like carbides which changes the carbide morphology and distribution. This can cause the microhardness of the core of the primary carbide to decrease [35,36].

A different group of MC carbides may also exist in the CCO due to the addition of other strong carbide forming elements such as W, Ti, and Nb. MC carbides have an FCC structure similar to NaCl and are very stable at high temperatures.

2.2.2.3 Other iron-based overlays

Besides the most commonly used CCOs, there are also some other types of iron-based overlays that have been developed. One of the important overlays is to use boron to replace most of the carbon in the overlay. Scoperta Inc. [37] reported a method of selecting a material composition with target properties using thermodynamic phase calculation. And an iron-based overlay containing multiple types of hard phase such as M_2B, W+Cr bordies, and NbC has been reported with improved impact resistance [38]. NanoSteel Company Inc. reported some wear resistant overlays with similar system in some other applications such as high abrasion wear [39–41]. In a crack resistant hypoeutectic overlay, the alloyed eutectic carbonitrides are found to be non-faceted growth which provides good cracking resistance [42].

2.3 Effect of chemical compositions on CCOs

The chemical composition of the chromium carbide overlay has a significant impact on its properties and performance. Chromium carbide (Cr_7C_3) is the primary hard phase in the overlay, and its chemical composition influences its wear resistance, toughness, and corrosion resistance.

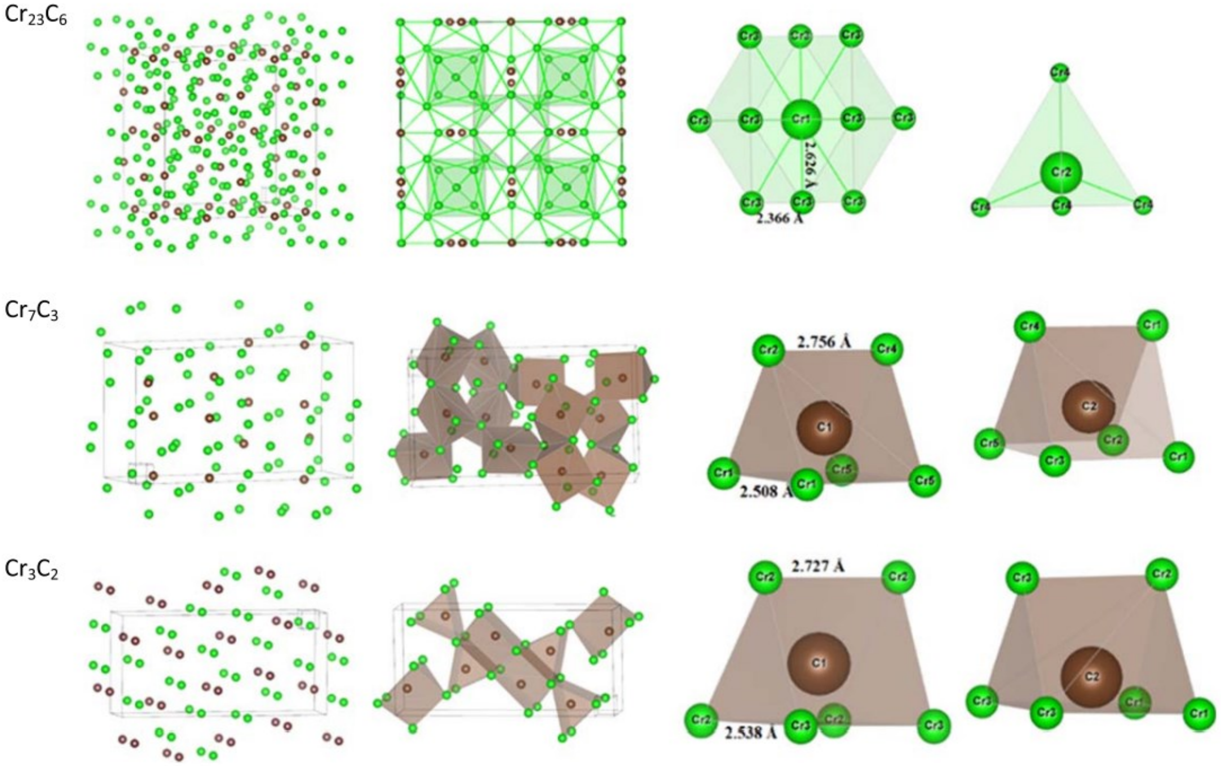

Figure 2.5: The crystal structures of $Cr_{23}C_6$, Cr_7C_3 and Cr_3C_2. The Cr atoms and the graphite atoms are represented by green and brown colour respectively. The rectangular box inset indicates a unit cell [33].

The amount of chromium carbide in the overlay, as well as its distribution and morphology, play a crucial role in determining its wear resistance. A higher volume fraction of chromium carbide generally leads to better wear resistance. The carbide particles should be well-distributed and evenly spaced to ensure maximum wear resistance. The composition of the matrix material in the overlay also affects its wear resistance. Typically, the matrix material is composed of iron and carbon. A higher carbon content in the matrix material can lead to better wear resistance, but it can also make the material more brittle. The chemical composition of the overlay also affects its toughness and resistance to cracking. In addition to wear resistance and toughness, the chemical composition of the overlay can also affect its corrosion resistance. Chromium is a key element in the overlay that provides its corrosion resistance. Careful consideration of these factors is essential in designing and selecting CCO for specific applications. In this section, the effects of some commonly used elements are summarized.

The enthalpy of mixing was reported as the heat of mixing values $\Delta H_{\{AB\}}^{mix}$ for the binary liquid in an A-B system. As shown in Table 2.1 and 2.2, the $\Delta H_{\{AB\}}^{mix}$ for small commonly seen mixing, i.e., Ti-C, V-C, Cr-C, Mn-C, Fe-C, Nb-C, Mo-C, and W-C is -109, -82, -61, -66, -50, -102, -67, and -60 kJ/mol, respectively. Therefore, the tendency to form TiC and NbC in the existence of multiple elements in the CCO is the highest compared to other carbides. In the following sections, the effect of various elements on the microstructure and wear resistance of the CCO will be discussed.

2.3.1 Effect of Cr

Chromium is one of the most feasible alloying elements to add in the welding overlay applications in the form of high carbon and low carbon ferrochrome. As a carbide forming element, it can form various kinds of primary and eutectic carbides during welding solidification. It is generally accepted that in order to obtain a good wear resistance property of the Fe-Cr-C based overlay, Cr content should be more than 10%. In the corrosive environment applications, higher Cr content is also necessary. This effect is through the Cr:C stoichiometry as shown in Figure 2.5. Increasing Cr is reported to reduce the eutectic carbon content in the high chromium white iron. Increasing Cr content without changing the C content will shift the eutectic point to the left which will result in more chromium carbides formation [43,44]. As the one of the most important elements in the chromium carbide overlays, Cr is the main element that forms primary carbide. It has been found that the wear resistance is mainly controlled by the volume fraction of chromium carbides. On the other hand, the corrosion resistance of these materials is largely dependent on the quantity of chromium in the matrix [45].

2.3.2 Effect of Nb

Niobium has a strong affinity for carbon and easily forms niobium carbide during solidification. The NbC has an FCC crystal structure similar to the NaCl crystal structure with 11.1 wt.% carbon and can only dissolve low amounts of other metallic elements. This means that the Nb content can constitute up to 85 wt.% of the total metallic content [46].

There are two main effects of Nb on the overlay. Firstly, NbC will participate first during solidification. The fine and granular NbC will act as heterogeneous nucleation sites for other hard particles that form later, such as the M_7C_3 primary carbide. Moreover, the later-formed hard particles are refined, and more eutectic colonies can precipitate due to the existence of NbC. Secondly, the formation of NbC will consume a lot of carbon during solidification, which may decrease the phase amount of later-formed hard particles and change the microstructure into a more hypoeutectic structure [46–53]. Increasing the Nb content resulted in a more refined microstructure, leading to higher hardness, lower wear rates, and less severe abrasive wear micromechanisms. This improvement in properties is due to the enhanced strengthening of the NbC and Fe-matrix [54].

2.3.3 Effect of Ti

Titanium has been found with a similar effect as niobium in terms of microstructure change which shifts the eutectic points to the right [48,55,56]. Incorporation of TiC particles into the microstructure of high chromium cast iron leads to improved hardness and promotes a transition in the abrasive wear mechanism from M_7C_3 fracture-exfoliation to micro-cutting and fatigue wear [57]. In addition, titanium can also form particles easily with boron and nitrogen. Artem'ev et al [58]. studied the effect of the addition of TiB_2 microparticles and TiCN nanoparticles in the deposition and found that the dissolution and diffusion between the TiB_2 and matrix resulted in the formation of strong chemical bonding and reliable fixation of the particles. As a result, the wear resistance of the deposited overlay is greatly enhanced. In addition, Ti can also form TiN, which can precipitate during solidification and act as heterogeneous nucleation sites for other particles. One fact that needs attention is that Ti can also react easily with oxygen and nitrogen during welding. It is believed that it will need extra caution when Ti is added to the overlay since it may cause welding cracks formation. However, the detailed effect of Ti to induce welding cracks in the overlay process is not well studied yet.

2.3.4 Effect of V

The addition of vanadium to CCO coatings has been found to significantly improve their wear resistance. Vanadium increases the hardness and toughness of the coating, thereby improving its ability to resist wear and abrasion. In fact, research has shown that the addition of just 1-2% vanadium can increase the wear resistance of CCO. This effect is

Table 2.1: The values of $\Delta \mathrm{H}_{\{\mathrm{AB}\}}^{\mathrm{mix}}$ (kJ/mol) calculated by Miedema’s model for atomic pairs between the elements with atomic numbers of (a) 1 to 46 and (b) 46 to 94. The values of $\Delta \mathrm{H}_{\{\mathrm{AB}\}}^{\mathrm{mix}}$ for atomic pairs containing H, C or N are treated as 0 kJ/mol in a previous study [59].

(a) / (b)		1	3	4	5	6	7	11	12	13	14	15	19	20	21	22	23	24	25	26	27	28	29	30	31	32	33	37	38	39	40	41	42	43	44	45	46	(a) / (b)	
		H	Li	Be	B	C	N	Na	Mg	Al	Si	P	K	Ca	Sc	Ti	V	Cr	Mn	Fe	Co	Ni	Cu	Zn	Ga	Ge	As	Rb	Sr	Y	Zr	Nb	Mo	Tc	Ru	Rh	Pd		
46	Pd	-27	-40	-8	-24	-32	-62	-15	-40	-46	-55	-36.5	-9	-63	-86	-65	-35	-15	-23	-4	-1	0	-14	-33	-42	-43.5	-36	-9	-61	-84	-91	-53	-15	4	6	2		Pd	46
47	Ag	-10	-16	6	5	-32	-94	0	-10	-4	-20	-18.5	7	-28	-28	-2	17	27	13	28	19	15	2	-4	-5	-17.5	-8	7	-27	-29	-20	16	37	24	23	10	-7	Ag	47
48	Cd	-6	-13	11	13	-27	-91	-3	-6	3	-13	-11.5	1	-32	-30	-8	9	17	2	17	6	2	6	1	1	-14.5	-4	1	-33	-35	-26	11	28	10	9	-6	-26	Cd	48
49	In	-6	-12	16	18	-27	-98	-5	-4	7	-10	-10.5	-4	-35	-30	-5	12	20	3	19	7	2	10	3	3	-13.5	-3	-4	-37	-36	-25	15	33	11	10	-8	-31	In	49
50	Sn	-4	-18	15	18	-23	-90	-8	-9	4	-11	-7.5	-7	-45	-45	-21	-1	10	-7	11	0	-4	7	1	1	-12.5	-1	-7	-46	-51	-43	-1	20	5	4	-13	-34	Sn	50
51	Sb	-1	-28	18	23	-13	-74	-20	-16	2	-8	2.5	-22	-62	-61	-33	-8	7	-11	10	2	-1	7	-1	-1	-10.5	3	-24	-66	-68	-60	-11	17	8	9	-8	-28	Sb	51
55	Cs	-16	16	29	29	-43	-155	3	25	26	-3	-24.5	0	19	70	104	103	97	71	85	58	48	28	15	14	-19.5	-12	0	14	62	101	135	128	69	64	34	-9	Cs	55
56	Ba	-49	0	-10	-19	-90	-212	-3	-4	-20	-52	-85.5	6	1	28	57	57	50	29	37	11	0	-9	-23	-30	-63.5	-66	9	0	20	52	81	73	11	6	-21	-62	Ba	56
57	La	-60	6	-29	-47	-116	-235	24	-7	-38	-73	-112.5	46	8	2	20	22	17	3	5	-17	-27	-21	-31	-41	-73.5	-81	52	14	0	13	36	31	-23	-28	-50	-82	La	57
58	Ce	-61	7	-30	-48	-116	-234	25	-7	-38	-73	-112.5	47	9	2	18	20	15	1	3	-18	-28	-21	-31	-41	-73.5	-81	53	15	0	12	34	29	-25	-30	-52	-83	Ce	58
59	Pr	-61	7	-31	-49	-117	-233	26	-6	-38	-73	-112.5	49	10	1	17	18	13	0	1	-20	-30	-22	-31	-41	-72.5	-81	55	16	0	10	32	26	-27	-32	-53	-83	Pr	59
60	Nd	-61	7	-31	-49	-116	-235	26	-6	-38	-73	-112.5	49	10	2	17	18	13	0	1	-20	-30	-22	-31	-40	-101.5	-80	55	16	0	10	32	26	-27	-32	-53	-83	Nd	60
61	Pm	-61	8	-33	-51	-118	-233	28	-6	-39	-74	-114.5	51	11	1	15	16	10	-2	-2	-23	-32	-23	-32	-41	-73.5	-81	57	18	0	9	29	23	-30	-35	-56	-86	Pm	61
62	Sm	-61	8	-32	-50	-117	-202	28	-6	-38	-74	-113.5	50	11	1	15	17	11	-1	-1	-22	-31	-22	-31	-40	-72.5	-80	56	17	0	9	30	24	-29	-34	-54	-84	Sm	62
63	Eu	-45	-1	-12	-19	-87	-231	0	-5	-19	-49	-79.5	10	0	21	48	49	43	23	30	7	-3	-10	-21	-27	-58.5	-60	13	0	14	42	69	63	6	2	-24	-61	Eu	63
64	Gd	-61	8	-32	-50	-117	-232	28	-6	-39	-73	-113.5	50	11	1	15	17	11	-1	-1	-22	-31	-22	-31	-40	-72.5	-80	56	17	0	9	30	24	-29	-34	-54	-84	Gd	64
65	Tb	-61	9	-33	-51	-118	-232	29	-6	-39	-74	-113.5	52	12	1	14	15	9	-3	-3	-23	-32	-23	-31	-40	-72.5	-80	58	18	0	8	28	22	-30	-35	-56	-85	Tb	65
66	Dy	-61	9	-32	-51	-117	-231	29	-6	-38	-74	-112.5	51	12	1	14	15	9	-3	-3	-23	-32	-22	-31	-40	-71.5	-80	58	18	0	8	27	22	-30	-35	-55	-84	Dy	66
67	Ho	-60	8	-32	-50	-116	-229	28	-6	-38	-73	-111.5	51	11	1	14	16	10	-2	-2	-22	-31	-22	-30	-39	-71.5	-79	57	18	0	9	28	22	-29	-34	-54	-83	Ho	67
68	Er	-61	9	-33	-52	-118	-230	30	-5	-38	-74	-113.5	53	13	0	13	14	8	-4	-5	-24	-34	-23	-31	-40	-71.5	-79	59	20	0	7	26	20	-32	-37	-57	-85	Er	68
69	Tm	-61	9	-33	-52	-117	-229	30	-5	-38	-74	-112.5	52	13	0	12	13	8	-4	-5	-24	-34	-23	-30	-39	-71.5	-79	59	20	0	7	25	19	-32	-37	-56	-85	Tm	69
70	Yb	-45	-1	-14	-22	-88	-199	2	-6	-20	-51	-80.5	12	0	16	41	43	37	19	25	2	-7	-12	-21	-27	-58.5	-59	16	1	10	36	61	55	1	-4	-28	-62	Yb	70
71	Lu	-61	10	-35	-54	-119	-231	31	-5	-39	-75	-114.5	55	14	0	11	11	5	-6	-7	-27	-36	-24	-31	-40	-71.5	-80	61	21	0	6	23	17	-35	-40	-59	-87	Lu	71
72	Hf	-63	30	-37	-66	-123	-218	63	10	-39	-77	-117.5	92	39	5	0	-2	-9	-12	-21	-35	-42	-17	-24	-34	-65.5	-75	98	50	11	0	4	-4	-47	-52	-63	-80	Hf	72
73	Ta	-46	48	-24	-54	-101	-173	89	30	-19	-56	-89.5	119	60	16	1	-1	-7	-4	-15	-24	-29	2	-3	-10	-37.5	-45	125	73	27	3	0	-5	-35	-39	-45	-52	Ta	73
74	W	-24	50	-3	-31	-60	-103	97	38	-2	-31	-46.5	124	57	9	-6	-1	1	6	0	-1	-3	22	15	11	-7.5	-9	129	70	24	-9	-8	0	-7	-10	-9	-6	W	74
75	Re	-18	29	0	-25	-42	-72	73	21	-9	-31	-32.5	95	28	-17	-25	-13	-4	-1	0	2	2	18	8	3	-7.5	-6	98	39	-4	-35	-26	-7	0	-1	1	6	Re	75
76	Os	-19	11	-2	-24	-35	-60	52	5	-18	-36	-29.5	70	4	-39	-41	-23	-11	-9	-4	0	1	10	-1	-7	-14.5	-11	72	13	-28	-55	-39	-14	0	0	2	8	Os	76
77	Ir	-20	-9	-5	-26	-32	-54	28	-13	-30	-43	-30.5	42	-23	-62	-57	-34	-18	-18	-9	-3	-2	0	-13	-21	-24.5	-19	44	-16	-53	-76	-53	-21	-2	-1	1	6	Ir	77
78	Pt	-24	-33	-10	-28	-30	-52	-1	-35	-44	-53	-34.5	9	-55	-89	-74	-45	-24	-28	-13	-7	-5	-12	-29	-38	-37.5	-31	9	-50	-83	-100	-67	-28	-3	-1	-2	2	Pt	78
79	Au	-8	-37	0	-2	-20	-58	-14	-32	-22	-30	-13.5	-9	-60	-74	-47	-19	0	-11	8	7	7	-9	-16	-19	-21.5	-11	-10	-59	-74	-74	-32	3	14	15	7	0	Au	79
80	Hg	-3	-19	15	19	-20	-81	-11	-10	4	-10	-4.5	-10	-43	-37	-10	10	21	4	22	12	8	8	1	1	-11.5	0	-11	-45	-43	-31	11	32	18	18	2	-18	Hg	80
81	Tl	-3	-15	23	27	-19	-91	-11	-3	11	-4	-1.5	-13	-40	-28	2	22	31	11	31	18	13	15	6	6	-9.5	3	-14	-44	-35	-19	26	46	25	24	5	-21	Tl	81
82	Pb	-1	-21	25	30	-13	-82	-18	-8	10	-2	4.5	-21	-52	-40	-8	15	28	7	29	17	13	15	5	5	-7.5	6	-23	-56	-48	-33	17	42	26	25	6	-18	Pb	82
83	Bi	0	-23	26	31	-12	-80	-20	-10	10	-2	5.5	-24	-56	-46	-14	10	24	3	26	14	10	15	4	4	-7.5	7	-26	-61	-54	-40	12	38	23	23	3	-21	Bi	83
90	Th	-61	14	-37	-57	-123	-237	39	-3	-40	-77	-119.5	65	19	0	8	9	2	-8	-11	-30	-39	-24	-30	-39	-72.5	-82	72	27	1	4	20	13	-39	-45	-63	-91	Th	90
92	U	-53	30	-27	-54	-105	-189	65	14	-30	-66	-98.5	93	37	3	0	1	-3	-5	-11	-23	-29	-7	-15	-25	-52.5	-60	99	48	11	-3	4	2	-31	-36	-46	-59	U	92
94	Pu	-54	21	-25	-50	-102	-188	49	6	-33	-66	-95.5	72	24	-1	2	4	2	-4	-6	-19	-25	-9	-20	-29	-56.5	-62	77	33	4	-3	9	8	-26	-30	-42	-58	Pu	94
(b) / (a)		H	Li	Be	B	C	N	Na	Mg	Al	Si	P	K	Ca	Sc	Ti	V	Cr	Mn	Fe	Co	Ni	Cu	Zn	Ga	Ge	As	Rb	Sr	Y	Zr	Nb	Mo	Tc	Ru	Rh	Pd	(b) / (a)	
		1	3	4	5	6	7	11	12	13	14	15	19	20	21	22	23	24	25	26	27	28	29	30	31	32	33	37	38	39	40	41	42	43	44	45	46		

Table 2.2 The values of $\Delta H^{mix}_{\{AB\}}$ (kJ/mol) calculated by Miedema' s model for atomic pairs between the elements with atomic numbers of (a) 1 to 45 and (b) 47 to 94. The values of $\Delta H^{mix}_{\{AB\}}$ for atomic pairs containing H, C or N are treated as 0 kJ/mol in a previous study [59].

(b)			(a)	1	3	4	5	6	7	11	12	13	14	15	19	20	21	22	23	24	25	26	27	28	29	30	31	32	33	37	38	39	40	41	42	43	44	45	(a)	
				H	Li	Be	B	C	N	Na	Mg	Al	Si	P	K	Ca	Sc	Ti	V	Cr	Mn	Fe	Co	Ni	Cu	Zn	Ga	Ge	As	Rb	Sr	Y	Zr	Nb	Mo	Tc	Ru	Rh		(a)
47	Ag	Ag		H	-25	2	5	-3	-18	-16	-19	-8	-19	0.5	-16	-46	-60	-54	-39	-28	-34	-23	-23	-23	-6	-8	-8	-14.5	-1	-16	-45	-61	-69	-46	-28	-21	-20	-23	H	1
48	Cd	-2	Cd		Li	-5	-6	-61	-145	4	0	-4	-30	-45.5	11	-1	12	34	37	35	19	26	8	1	-5	-7	-9	-34.5	-29	13	0	8	27	51	49	8	5	-14	Li	3
49	In	-2	0	In		Be	0	-15	-39	18	-3	0	-15	-3.5	27	-14	-36	-30	-16	-7	-10	-4	-4	-4	0	4	5	-3.5	7	28	-10	-32	-43	-25	-7	-3	-3	-6	Be	4
50	Sn	-3	0	0	Sn		B	-10	-28	18	-4	0	-14	0.5	27	-22	-55	-58	-42	-31	-32	-26	-24	-24	0	4	6	-0.5	10	28	-18	-50	-71	-54	-34	-25	-24	-25	B	5
51	Sb	-4	-2	-4	-1	Sb		C	-2	-45	-55	-36	-39	-4.5	-43	-89	-118	-109	-82	-61	-66	-50	-42	-39	-33	-32	-33	-29.5	-14	-44	-87	-117	-131	-102	-67	-39	-35	-35	C	6
55	Cs	8	1	-4	-7	-25	Cs		N	-141	-134	-92	-81	-24.5	-152	-201	-224	-190	-143	-107	-119	-87	-75	-69	-84	-88	-95	-78.5	-59	-154	-206	-232	-233	-174	-115	-68	-61	-63	N	7
56	Ba	-28	-36	-42	-51	-72	12	Ba		Na	10	13	-11	-26.5	1	1	34	68	73	71	49	62	41	32	16	6	5	-21.5	-14	2	-2	28	59	93	93	47	44	19	Na	11
57	La	-30	-36	-39	-53	-71	57	16	La		Mg	-2	-26	-39.5	20	-6	-3	16	23	24	10	18	3	-4	-3	-4	-4	-26.5	-21	23	-4	-6	6	32	36	3	0	-17	Mg	12
58	Ce	-30	-36	-38	-52	-70	59	17	0	Ce		Al	-19	-20.5	23	-20	-38	-30	-16	-10	-19	-11	-19	-22	-1	1	1	-14.5	-6	25	-18	-38	-44	-18	-5	-20	-21	-32	Al	13
59	Pr	-30	-35	-37	-52	-69	60	18	0	0	Pr		Si	-25.5	-4	-51	-74	-66	-48	-37	-45	-35	-38	-40	-19	-18	-17	-14.5	-17	-4	-49	-73	-84	-56	-35	-38	-38	-46	Si	14
60	Nd	-29	-35	-37	-51	-69	60	18	0	0	0	Nd		P	-24.5	-81.5	-112.5	-100.5	-70.5	-49.5	-57.5	-39.5	-35.5	-34.5	-17.5	-17.5	-18.5	-17	-2.5	-24.5	-81.5	-113.5	-127.5	-89.5	-53.5	-33.5	-30.5	-34.5	P	15
61	Pm	-30	-35	-37	-52	-69	63	20	0	0	0	0	Pm		K	12	58	94	96	91	66	81	55	45	25	13	12	-19.5	-11	0	7	50	88	123	120	65	60	31	K	19
62	Sm	-30	-35	-36	-51	-68	62	20	0	0	0	0	0	Sm		Ca	17	43	44	38	19	25	2	-7	-13	-22	-28	-59.5	-61	15	1	11	37	63	56	1	-4	-28	Ca	20
63	Eu	-27	-32	-35	-44	-63	16	0	11	12	13	13	14	14	Eu		Sc	8	7	1	-8	-11	-30	-39	-24	-29	-38	-69.5	-77	64	25	1	4	18	11	-39	-44	-61	Sc	21
64	Gd	-29	-35	-36	-51	-68	62	20	0	0	0	0	0	0	14	Gd		Ti	-2	-7	-8	-17	-28	-35	-9	-15	-23	-51.5	-60	100	53	15	0	2	-4	-39	-43	-52	Ti	22
65	Tb	-29	-34	-35	-50	-67	64	21	0	0	0	0	0	0	15	0	Tb		V	-2	-1	-7	-14	-18	5	-2	-8	-31.5	-35	100	54	17	-4	-1	0	-21	-25	-29	V	23
66	Dy	-29	-34	-35	-50	-67	63	21	0	0	0	0	0	0	15	0	0	Dy		Cr	2	-1	-4	-7	12	5	-1	-18.5	-19	94	47	11	-12	-7	0	-9	-12	-13	Cr	24
67	Ho	-29	-33	-35	-49	-66	62	20	0	0	0	0	0	0	15	0	0	0	Ho		Mn	0	-5	-8	4	-6	-13	-31.5	-31	69	27	-1	-15	-4	5	-8	-11	-16	Mn	25
68	Er	-29	-33	-34	-49	-66	65	22	1	0	0	0	0	0	16	0	0	0	0	Er		Fe	-1	-2	13	4	-2	-15.5	-14	83	34	-1	-25	-16	-2	-3	-5	-5	Fe	26
69	Tm	-29	-33	-34	-49	-66	65	22	1	0	0	0	0	0	16	0	0	0	0	0	Tm		Co	0	6	-5	-11	-21.5	-18	57	10	-22	-41	-25	-5	0	-1	-2	Co	27
70	Yb	-28	-31	-34	-43	-61	19	1	8	8	9	9	11	10	0	10	11	11	11	12	12	Yb		Ni	4	-9	-15	-23.5	-19	47	-1	-31	-49	-30	-7	1	0	-1	Ni	28
71	Lu	-30	-33	-34	-49	-66	67	24	1	1	0	0	0	0	18	0	0	0	0	0	0	14	Lu		Cu	1	1	-11.5	-3	27	-9	-22	-23	3	19	8	7	-2	Cu	29
72	Hf	-13	-19	-18	-35	-50	104	54	15	14	13	13	11	11	44	11	10	10	10	9	9	38	8	Hf		Zn	0	-15.5	-6	14	-21	-31	-29	-1	12	-4	-5	-17	Zn	30
73	Ta	15	9	13	-3	-13	130	77	33	31	29	29	27	27	66	27	25	25	26	23	23	58	21	3	Ta		Ga	-15.5	-6	13	-27	-40	-40	-8	7	-10	-11	-25	Ga	31
74	W	43	33	38	27	25	132	74	32	29	26	26	23	24	64	24	21	21	22	19	19	56	16	-6	-7	W		Ge	-12.5	-19.5	-59.5	-72.5	-72.5	-36.5	-13.5	-18.5	-18.5	-29.5	Ge	32
75	Re	38	25	29	20	23	101	42	3	0	-2	-2	-5	-4	34	-4	-7	-7	-5	-9	-9	28	-12	-30	-24	-4	Re		As	-12	-61	-80	-85	-44	-16	-15	-14	-24	As	33
76	Os	28	14	16	9	14	74	15	-21	-24	-26	-26	-29	-28	9	-28	-30	-29	-28	-31	-31	4	-34	-48	-38	-10	-1	Os		Pb	10	56	95	130	125	67	62	33	Rb	37
77	Ir	16	0	0	-5	1	45	-14	-48	-50	-52	-51	-55	-53	-18	-53	-55	-55	-53	-56	-56	-22	-59	-68	-52	-16	-3	-1	Ir		Sr	17	48	76	69	10	5	-22	Sr	38
78	Pt	-1	-18	-21	-25	-17	10	-50	-80	-81	-82	-82	-85	-84	-51	-83	-85	-84	-83	-86	-85	-54	-88	-90	-66	-20	-4	0	0	Pt		Y	9	30	24	-29	-34	-54	Y	39
79	Au	-6	-11	-11	-10	-4	-9	-60	-73	-73	-73	-73	-75	-74	-58	-74	-74	-74	-72	-74	-74	-59	-75	-63	-32	12	20	18	13	4	Au		Zr	4	-6	-53	-59	-72	Zr	40
80	Hg	-1	0	-1	0	-1	-11	-49	-45	-44	-43	-43	-43	-43	-43	-43	-42	-42	-41	-41	-41	-42	-41	-23	9	38	33	23	9	-9	-4	Hg		Nb	-6	-36	-41	-46	Nb	41
81	Tl	3	2	0	2	-1	-15	-49	-38	-37	-36	-36	-35	-35	-41	-35	-34	-34	-33	-33	-32	-39	-32	-11	24	52	44	30	14	-8	-2	1	Tl		Mo	-11	-14	-15	Mo	42
82	Pb	3	2	-1	2	1	-25	-62	-51	-50	-49	-49	-49	-48	-53	-48	-47	-46	-46	-45	-45	-50	-45	-23	15	49	44	32	16	-5	2	1	-1	Pb		Tc	0	0	Tc	43
83	Bi	2	1	-1	1	1	-27	-68	-58	-57	-56	-55	-55	-54	-58	-54	-53	-53	-52	-52	-51	-55	-51	-30	9	45	40	29	14	-8	2	1	-1	0	Bi		Ru	1	Ru	44
90	Th	-29	-32	-31	-48	-65	78	30	3	2	2	2	1	1	23	1	1	1	1	1	1	18	0	6	18	12	-16	-39	-64	-94	-78	-39	-28	-41	-48	Th		Rh	Rh	45
92	U	0	-8	-7	-23	-34	104	52	15	14	12	12	10	11	43	11	10	9	10	8	8	36	7	-2	3	1	-17	-33	-50	-68	-43	-10	1	-9	-15	4	U			(a)
94	Pu	-6	-16	-16	-30	-42	81	36	7	6	5	5	4	4	29	4	3	3	3	2	2	24	1	-1	8	8	-10	-26	-44	-63	-45	-18	-10	-20	-26	0	1	Pu		
(b)		Ag	Cd	In	Sn	Sb	Cs	Ba	La	Ce	Pr	Nd	Pm	Sm	Eu	Gd	Tb	Dy	Ho	Er	Tm	Yb	Lu	Hf	Ta	W	Re	Os	Ir	Pt	Au	Hg	Tl	Pb	Bi	Th	U	Pu		
	(b)	47	48	49	50	51	55	56	57	58	59	60	61	62	63	64	65	66	67	68	69	70	71	72	73	74	75	76	77	78	79	80	81	82	83	90	92	94	(b)	

due to the formation of V-rich carbides that act as additional hard phases in the coating. Additionally, When V is introduced into a material containing M_7C_3 carbides, it can partially replace Cr in their structure, leading to the formation of $(Cr,Fe,V)_7C_3$ type carbides with some V atoms may also dissolve into the austenitic phase. Once the V concentration in both the austenite and M_7C_3 carbides has reached saturation, V-rich MC carbides can precipitate from the austenite phase [60].

2.3.5 Effect of B

A previous study [61] has shown that compared to carbide-based overlays, boride-based overlays show superior abrasion and particle erosion resistance with higher overlay hardness. When increasing the system boron concentration to some point, the primary borides will start to precipitate [62]. It is common to add boron in the overlay material to refine the austenite. Under certain welding conditions, boron can form Fe_2B fine crystals oriented perpendicular to the wearing surface which will contribute largely to the improvement of wear resistance [63].

2.3.4 Effect of Si

Si is only dissolved in the matrix [64]. Increasing the Si content is found to result in a significant refinement of primary carbides in hypereutectic high chromium cast iron. This refinement contributes to an improvement in the material's hardness and wear resistance. However, when the Si content exceeds 1.9%, the wear resistance begins to decrease. As a ferrite stabilizer, the Si also transfers the matrix structure gradually from austenite to ferrite [64,65]. As an inexpensive material, Si also has a high affinity for oxygen and is easily oxidized to improve the porosity formation tendency in the weld pool. Thus, a small amount up to 3 wt.% of Si is typically favorable to add to the commercial CCO.

2.3.5 Effect of Mo

To prevent pearlitic transformation, the molybdenum content in typical white high chromium cast iron is generally kept below 3 wt.%. However, studies suggest that adding more than 3 wt.% of molybdenum can lead to the formation of new carbides (M_2C, M_6C) that significantly improve high-temperature wear resistance [66–68]. When Mo content is lower, the effect of Mo seems complicated. First of all, Mo is more enriched in the eutectic carbides instead of the primary carbides. The carbide fraction in hardfacing alloys containing molybdenum (Mo) is higher compared to Mo-free hardfacing alloys. However, the carbide fraction remains similar across all hardfacing alloys with Mo addition because the driving force per unit increase in Mo content exhibits a significant increase when the Mo content is raised from 0 to 1.35 wt.%. Further increases in Mo content do not result in the same extent of change in the driving force [69]. Similarly, Mo can also incorporated into other carbides such as MC carbides.

2.3.6 Effect of Mn

Similar to Cr, Mn content is typically concentrated in the primary and eutectic M_7C_3 carbides. It has been found that an increase in the microhardness of the matrix and carbides can be observed with a variation in the quantity of manganese. This rise in hardness is linked to the formation of secondary precipitates in the matrix following heat treatment, and the dissolution of manganese in M_7C_3 carbides during the eutectic reaction [70]. As a commonly used element for steel making at an inexpensive price, Mn provides important functions such as deoxidation and desulfurization which is a go-to additive in the welding application.

2.4 Challenges and knowledge gaps

The influence of chemical composition on the solidification of welding overlays is widely recognized. Previous studies have explored the individual effects of commonly used elements, as mentioned earlier. However, the traditional approach to overlay material design limits the investigation to a maximum of two elements, thereby neglecting the simultaneous effects of multiple elements. Most welding overlay materials consist of several elements that collectively influence the solidification process and the resulting microstructure. Furthermore, the chemical composition significantly affects the formation of welding defects, including cracks. Therefore, it is crucial to systematically study the combined effects of multiple elements in this complex system to achieve the desired microstructure, performance, and weldability. New approaches are needed in assisting the study of simultaneous effect of multiple elements.

The primary carbide has been proven to play a crucial role in the wear performance of the overlay material. Achieving an optimized morphology and composition of primary and eutectic carbides/carbonitrides is essential for ensuring satisfactory wear resistance, corrosion resistance, and crack resistance.

Numerous studies have intentionally focused on creating a complex system with primary hard phases consisting of M_7C_3 and MC carbides. The formation of MC type carbides, which typically include NbC and TiC, has been shown to offer several advantages. Notably, MC carbides exhibit higher microhardness compared to M_7C_3 carbides, as indicated in

Table 2.3. However, the precise control of complex carbide morphology and composition, both theoretically and experimentally, remains unclear. This is primarily due to the intricate metallurgical phase transformations that occur during solidification from the molten state, as well as the interactions between alloying elements, process parameters, and the resulting material performance.

Table 2.3: Typical primary carbide and their hardness values as summarized by Berns and Fischer [46].

Carbide	Crystal Structure	Hardness (HV)	C atomoic %
M_3C	Orthorhombic	800-1600	25%
M_7C_3	Hexagonal	1190-1800	30%
$M_{23}C_6$	FCC		20.7%
MC (TiC)	FCC	2500-3300	50%
MC (NbC)	FCC	1900-2000	50%
Martensite	BCT	400-900	
Austenite	FCC	430-600	

2.5 Objectives of the thesis

The motivation behind this thesis is to provide a fundamental understanding of the "chemical composition – application method – microstructure – wear resistance" relationship of the chromium carbide of overlays. This thesis aims to address the following objectives:

1. Investigate new approaches using arc furnace button melting to accelerate the traditional wire making process for new chromium carbide overlay formulation.
2. Design of Experiments and Machine Learning approach to help understand the

simultaneous effect of Nb, V, and Ti on the overlay hardness.

3. Gain the ability to design new crack-free overlay formulations to serve new application requirements of wear and corrosion.
4. Explore a new method to modify the microstructure of the overlay without adding new hard phase by using small levels of aluminum.

2.6 Outline of the thesis

This thesis consists of 8 chapters. Chapters 1 is the Introduction. Chapter 2 dis the Literature Review and Chapter 3 is Materials and Methodology used to address the objectives. A brief outline of each chapter is included below.

1. Chapter 4 focuses on the development and validation of using arc furnace button melting to simulate the welding process. Multi-scale characterizations using SEM and XRD are used to understand the difference in microstructure and phase constituent for materials prepared using the two methods. Numerical simulation of the temperature field is used to understand the cause of differences. This Chapter will be the methodology foundation for the following chapters.
2. Chapter 5 focuses on the development of new methods to understand three common carbide forming elements in the chromium carbide overlays using Design of Experiments and Machine Learning. A model was developed to visualize the relationship between the chemical composition input and hardness output. It provides quantitative guidance on how the strong carbide formers contribute to the overlay hardness in the same matrix. The method developed in this Chapter will

be used to assist the design of new formulas for the following chapters.

3. Chapter 6 focuses on the development of a novel chromium carbide overlay with a complex microstructure to serve the neEDX of wear resistance and corrosion resistance. A proper chemical composition to form a crack-free chromium carbide is designed with a fine primary MX and a eutectic of M_2B and austenite in a martensite/retained austenite matrix.
4. Chapter 7 focuses on the modification of primary carbide morphology in order to improve the scratch resistance of the commercial chromium carbide overlay. This is a follow-up work of chapter 5 when the core-shell structure was detected with aluminum core inoculated microstructure. The scratch tests will be performed to compare the wear resistance between the samples with 0 and 1 wt.% aluminum addition.
5. Chapter 8 summarizes the work and provides some future work.

Chapter 3

Materials and Methodology

3.1 Materials

Various industrial-grade powders were used to formulate the designed chemical compositions for the chromium carbide overlays. The chemical composition of the main elements in the powder used is listed in Table 3.1.

3.2 Arc furnace button melting

After the powders were weighed based on various designed chemical compositions, they were mixed for 120s in the ball mill. 10 g of the mixed powder materials were loaded into an arc furnace (MRF Furnaces, Model SA-200) as shown in Figure 3.1. After loading the sample, the furnace chamber was vacuumed and backfilled with argon to atmospheric pressure. The argon was kept on during the melting to maintain a positive argon pressure and protective atmosphere. A direct current with tungsten electrode-negative was used with an amperage of 120 - 180 A. The stick-out and contact tip to work distance was manually manipulated so that the electrode tip was approximately 6 mm from the workpiece. To obtain a homogeneous mixing, melting was repeated 5 times. On each melting, the button was turned upside down to ensure uniform mixing. Once repeatedly melted, the button was cooled in the copper hearth with water cooling for a few minutes to room temperature to prevent any contamination or oxidization. The cross-sectional and top surfaces of both welded and button melted samples were prepared for characterization.

Table 3.1: Chemical composition of the powder used (wt.%).

Materials	C	Cr	Mn	Si	Mo	Nb	Ti	V	W	Al	Fe
High-Carbon Ferrochrome	9	68									Remaining
Low-Carbon Ferrochrome		65									Remaining
Ferromanganese			75								Remaining
Ferrosilicon				75							Remaining
Ferromolybdenum					55						Remaining
Ferroniobium						50					Remaining
Ferrotitanium							30				Remaining
Ferrovanadium								50			Remaining
Ferrotungsten									70		Remaining
Aluminum										100	
Iron Powder											100

3.3 Microstructure characterization

3.3.1 Optical Microscopy

To characterize the microstructure, the melted samples were prepared by mounting, grinding, and polishing with the use of an automatic mechanical polisher. The grinding process involved the use of SiC sandpapers with grit sizes of 80, 180, 320, 600, and 1200.

Polishing was performed using diamond suspensions of 3, 1, and 0.25 μm particle size and colloidal silica suspensions of 0.05 and 0.02 μm particle sizes. After polishing, the samples were subjected to ultrasonic cleaning for 5 minutes and dried using compressed air. For optical and electron microscope analysis, the polished specimens were etched with Villela reagent, which consisted of 1 g picric acid, 5 ml hydrochloric acid, and 100 ml ethanol. The optical microscope, namely Zeiss Axio Vert.A1, was utilized for the optical examinations.

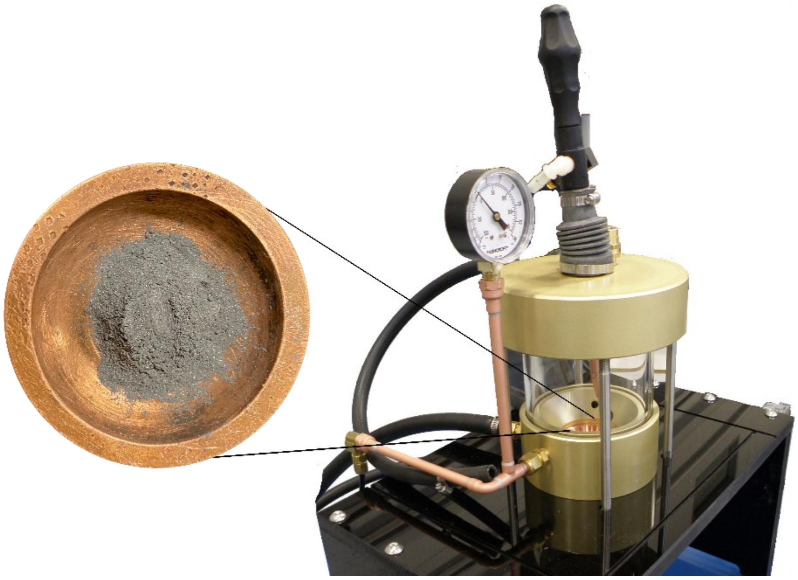

Figure 3.1: Arc furnace used to melt the raw powder and the magnified view of powder in the copper hearth.

2.3.2 Hardness measurements

The microhardness tests across the samples were conducted with various test forces as shown in the later sections and dwell time of 10 s on a Wilson VH3100 hardness tester. More details were mentioned in the later sections. At least 5 hardness tests were performed on each sample to obtain the average readings and the standard deviation.

The overlay microstructure typically consists of phases with significantly different hardness, i.e., the carbides are hard, and the austenite is soft. Therefore, using a large load could eliminate the non-uniformity of the hardness measurement and lower the measurement bias.

3.3.3 Scanning Electron Microscopy and Electron Backscatter Diffraction

The microstructure of the samples was analyzed using a TESCAN Vega-3 Scanning Electron Microscope, a Zeiss Evo Scanning Electron Microscope, and a Zeiss Sigma Field Emission Scanning Electron Microscope (FESEM). The TESCAN Vega-3 and Zeiss Evo SEM were both equipped with a secondary electron detector, a backscattered electron detector, and an Energy Dispersive Spectroscopy (EDX) detector. The secondary electron (SE) detector was utilized for surface morphology analysis, while the backscatter electron (BSE) detector was used to distinguish between light and heavy elements with varying atomic Z numbers. The energy dispersive spectroscopy detector was employed for chemical analysis including point, line, and map analysis.

To obtain microstructure observations at a finer scale on the etched surface, the Zeiss Sigma FESEM was utilized. The FESEM was equipped with a range of detectors, including a secondary electron detector, an Inlens secondary electron detector, a backscattered electron detector, an energy dispersive spectroscopy detector, and an electron backscatter diffraction detector. A 30 μm objective aperture and an accelerating voltage of 10 - 20 kV were used for topographic and chemical analysis. Besides the use of SE, BSE, and EDX detector described, the electron backscatter diffraction (EBSD) detector was used to identify phases and measure crystal orientation. A 60 μm objective aperture and an accelerating voltage of 20 kV were used for EBSD analysis. EBSD mapping was conducted with step sizes ranging from 20-80 nm. To assess and visualize the magnitude of local strain or deformation within grains, misorientation maps were processed. This was achieved by calculating the kernel average misorientation (KAM) between groups of pixels or kernels within the grains. The Channel 5 and Aztec Crystal processing software were utilized for EBSD data processing and reconstruction of maps.

2.3.4 X-Ray diffraction

X-ray diffraction (XRD) was performed to identify the phases of the overlay. The scanning range was from 20° to 100° with a scan rate of 2° per minute on a Rigaku Ultima IV X-ray diffractometer with a Cu Kα X-ray source. XRD could obtain all the phase information of the bulk material inclusively; therefore, it was helpful to extract the matrix phase signal and improve the identification of primary carbide and eutectic phases. The overlay specimen was immersed in the Villela reagent for 2 to 7 days at room temperature. It was then washed and dried and underwent XRD scanning on the same surface to compare with the bulk analysis. Rietveld refinement of raw XRD data was carried out using an open-source software Profex-BGMN [71] to de-convolute the peaks sharing similar 2h ranges and to identify and quantify the phases present in the overlay system. A quantitative phase fraction was therefore obtained.

3.3.5 Image Analysis with ImageJ

ImageJ was employed for various image post-processing tasks, such as image format conversion, contrast/brightness adjustment, and resizing. Additionally, the area fractions of various phases and carbide size were measured using ImageJ software.

3.4 Thermodynamic Calculation

Thermodynamic calculations were carried out using Thermo-Calc Software (2016a to 2021b version) with the TCFE6/ TCFE10 (Steels/Fe-alloys) and SLAG2 (Fe-containing slag) databases. The equilibrium phase fraction of various samples as a function of temperature was calculated. The calculations considered various phases, such as liquid, BCC-iron, FCC-iron, $M_{23}C_6$ carbide, M_7C_3 carbide, MC carbide, M_2B boride, etc. Furthermore, Gibbs free energy and Scheil solidification were also calculated. In Thermo-Calc calculations, a complete mixing of all elements in liquid and solid-state diffusion of two fast-diffusing elements, carbon and boron, were assumed. Some mismatch was expected between phase fractions from the equilibrium Thermo-Calc predictions and the actual phase fractions following the non-equilibrium flux-cored arc welding process.

3.5 Nano Scratch Analysis

To test the wear-resistant properties of the overlay samples at a local micro level, a nano scratch test was performed on the samples using an Anton Paar Revetest Scratch Tester (RST3) in the Material Property Assessment Laboratory (MPAL) at McMaster University. The bottom surface of the melted overlay sample was chosen since it would be parallel to the wear surface in a real-world application. The surface was prepared by grinding, polishing, and light etching before the scratch tests. A 1 mm line was scratched 5 passes by a diamond indenter with a 20 μm tip radius, under a load of 1500 mN and at a constant speed of 5mm/min. The normal force, friction force, acoustic emission, penetration depth, and friction coefficient data were collected for each pass. After the tests, the scratch marks were examined by a Zeiss Sigma field emission scanning electron microscope (FESEM).

3.6 Finite Element Analysis

Finite element analysis was conducted using the commercial simulation software COMSOL and Abaqus to investigate the temperature fields and stress distribution of various samples. A model consisting of multiple phases, including the austenite matrix and primary carbide was built. The stress distribution of each phase was therefore shown. More details of the methods were discussed in the following sections.

Chapter 4

Viability of button melting for accelerated development of chromium carbide overlay

4.1 Introduction

The chromium carbide overlay of the Fe-Cr-C system is widely used in tribological applications due to its good wear and corrosion resistance [72,73]. Depending on the operational environment, various alloying elements, such as Nb, Ti, Mn, Si, Mo, V, B, and W, are added for enhanced performance [47,56]. Depending on the welding processes for overlay, the welding filler metal is either in powder form, such as for plasma transferred arc welding, or in wire form, such as for flux-cored arc welding and gas metal arc welding. Flux-cored wire making requires a manufacturing process that wraps the powder ingredients with a sheath metal skin. The wire developing process involves costly and time-consuming iterations of adjusting the alloying and flux ingredients, wire drawing, welding test, and performance evaluations. What complicates the design iteration is the effect of welding parameters on dilution from the base metal. The dilution demands further adjustments of the mass percentage of main alloying powders in the welding wire. For the microstructure and performance of the overlay, critical parameters such as cooling rate, primary carbide size and volume fraction, hardness, and wear resistance need to be evaluated in wire design. The most time-consuming step in new wire development is wire fabrication.

A tungsten arc melting furnace has been used to melt and cast small ‘‘buttons” of alloys [74,75]. Small samples (10 to 100 g) of different compositions are melted using the arc furnace in a water-cooled copper hearth under an argon atmosphere. Advantages relevant for alloy design are that the dilution can be avoided, cooling rate can be controlled, and the amount of powder needed is small. Button melting has proved to be a good representation of actual welding by Balmforth and Lippold by creating constitutional diagrams for weld solidification [76,77]. Because the viability of replacing wire fabrication and welding with button melting has never been established, this chapter aims to quantitatively compare button melting and welding applied to the same overlay alloy. Significant cost and time saving can be achieved if button melting is proved as a viable process for welding wire alloy design.

4.2 Materials and methods

Two types of chromium carbide overlay samples with the same chemical composition (wt.%), 3–5% C, 25–35% Cr, 1–4% Mn, 1–4% Si, balance Fe, were prepared for this study: (1) A commercial CCO wire with 1.6 mm diameter from Trimay Wear Plate Ltd was used for welding experiments. In the welding test, a self-shielded flux cored arc process was used with a current of 180 to 200 A and voltage of 26 to 30 V. Two layers of deposition were welded on a low carbon steel plate base metal. (2) The same wire was used in the button melting test, in which 10 g of the welding wire was cut into 2-mm long pieces and loaded into an arc furnace. The button melting method used in this chapter was described in the previous section. The cross-sectional and top surfaces of both welded and button melted samples are prepared for characterization. Optical microscopy, hardness measurements, and X-ray diffraction (XRD) were used to characterize the welding and button melting samples. Detailed sample preparation and analysis procedures can be found in the previous section.

4.3 Microstructure Evaluation

The microstructure of the button-melted overlay is hypereutectic, consisting of uniformly distributed hexagonal-shaped primary carbides surrounded by a eutectic matrix (Figure 4.1). The growth of primary carbide is along the vertical direction of the button-melting furnace. This directional solidification feature has not been reported before. The basal plane of the primary Cr_7C_3 hexagonal carbide is believed to be perpendicular to the growth direction [78]. It has been reported that the wear performance of chromium carbide overlays depends on the carbide orientation [79,80]. This is due to the plastic deformation and failure path occurred with respect to the orientation of carbides and the wear surface.

For comparison, the microstructure of the welded sample is shown in Figure 4.2. Since the base metal is low in carbon and alloying elements, the first overlay layer is diluted, which has resulted in a hypoeutectic microstructure in the first layer, where the primary phase upon solidification is austenite (Figure 4.2a and 4.2c). As the second layer is deposited, the dilution effect from the base metal has decreased, leading to a microstructure transition to eutectic (Figure 4.2b and 4.2d), and hypereutectic (Figure 4.2e), where the primary phase upon solidification is carbide. Compared to the microstructure from button melting, the welded sample has randomly oriented primary carbide in both top and cross-sectional views (Figure 4.2e and 4.2f). The size, distribution, and orientation of primary carbides in the welded overlay are in agreement with previous studies [80,81]. The eutectic constituents seem to uniformly partition and surround the primary carbide or austenite dendrites meaning that an adequate wetting must have happened upon the solidification, as shown by Straumal et al [82] Good interfacial wetting between the primary phases and matrix has great significance in determining the mechanical properties of the overlay, as shown by Konyashin et al in the WC-Co wear-resistant system [83].

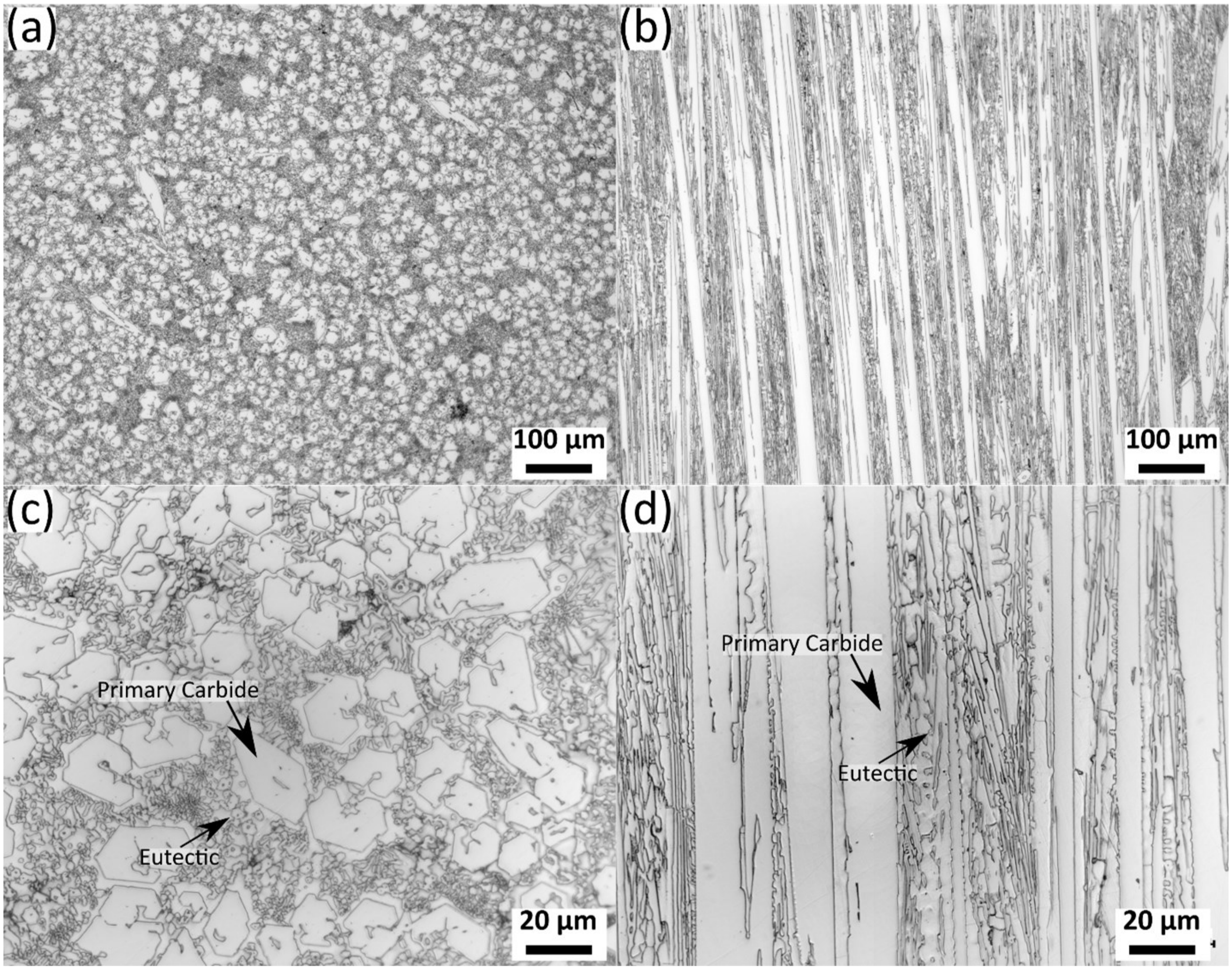

Figure 4.1: Microstructure of the button melted wire, top view (a), and cross-sectional view (b). Microstructure of top view (c), and cross-sectional view (d) at a higher magnification, showing details of the eutectic.

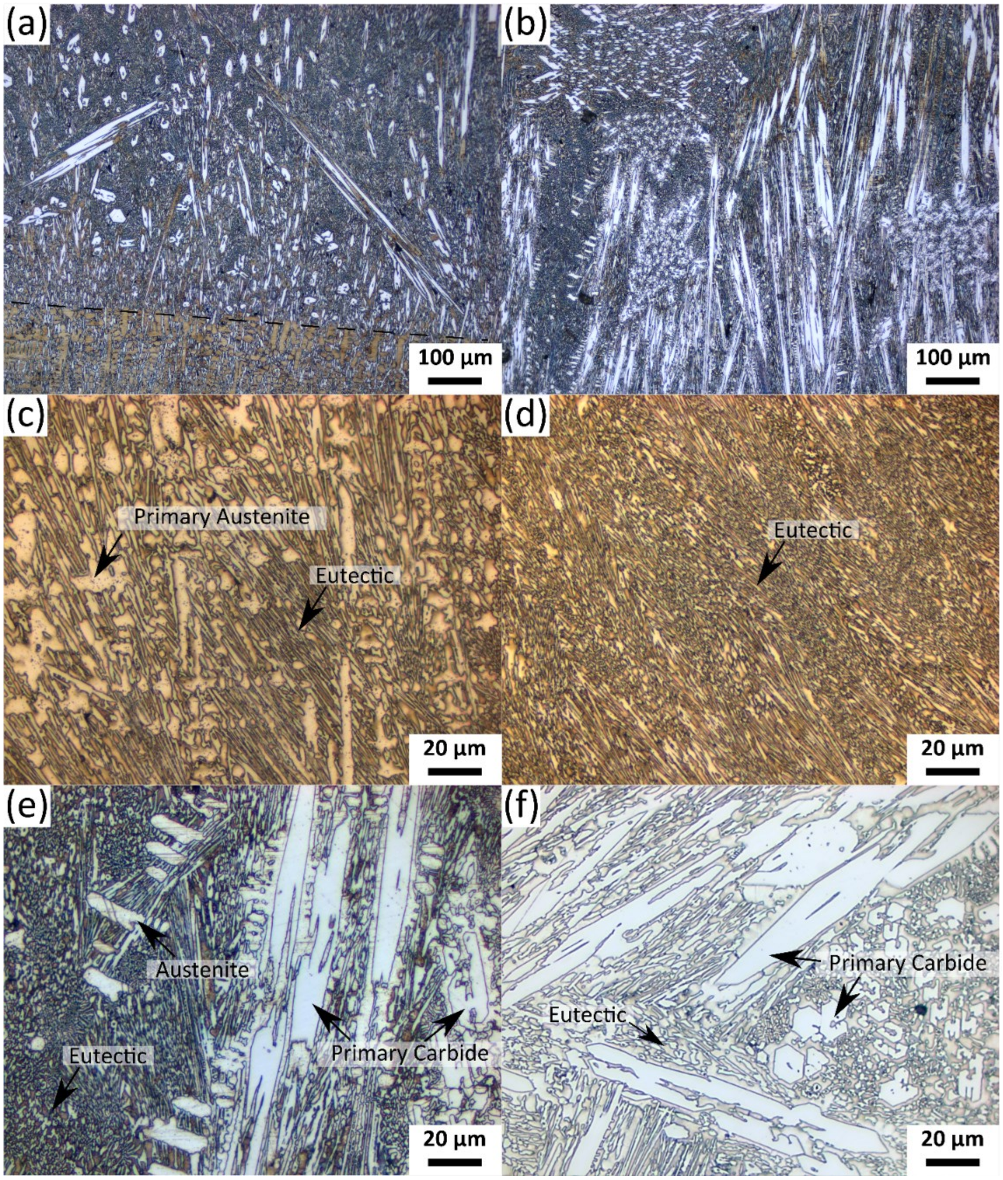

Figure 4.2: Optical microstructure of the overlay by welding, (a) cross-sectional plane view of the transition zone at low magnification. The dashed line shows the transition from the hypoeutectic and eutectic zone to the hypereutectic zone. (b) cross-sectional plane view of the second overlay layer at low magnification, (c) cross-sectional plane view of hypoeutectic region at high magnification, (d) cross-sectional plane view of eutectic region at high magnification, (e) cross-sectional plane view of hypereutectic region at high magnification, and (f) top view of hypereutectic region at high magnification. Note that the up and down direction in a to e corresponds to the top surface and bottom surface direction of the sample.

4.4 Hardness

A hardness survey is shown in Table 4.1 to illustrate this effect. The hardness on the top surface is greater than that on the cross-section for both button melting and welding sample. This result is consistent with previous reported work with a controlled high cooling condition [80]. However, the corresponding hardness values of the button melting sample falls within the wire manufacturer's original design target which is greater than the hardness values of the welding sample. The higher hardness of the button melted sample can be attributed to the uniformity of the microstructure and the preferred orientation of primary carbides. As the morphology of M_7C_3 carbides exhibits a pencil-like shape, the hardness on the basal plane is greater than the plane along c axis [80]. If the growth condition of the M_7C_3 carbides is controlled well like the button melting condition, the carbide would orient along the heat flux direction, which is the vertical top-down direction in the images. However, in the welding condition, there are more complex heating and cooling conditions microscopically in the multi-layer deposition process, which is not ideal to achieve the best performance of designed wires.

Table 4.1: Microhardness (HV5) measurement of the overlay at various planes.

Method	Plane	HV5
Welding	Cross Section	626±16
	Top	695±24
Button Melting	Cross Section	693±12
	Top	821±23

4.5 Phase Analysis

The volume fraction of primary carbides can be assumed similar between the welding and button melting conditions due to the same chemical composition and the back diffusion of substitutional solutes is negligible. This is confirmed by the volume fraction of primary carbide phases in XRD in Table 4.2. However, the volume fraction of austenite and martensite varies a lot due to the cooling condition during solid state phase transformation. As shown in Figure 4.3, the button melting XRD pattern shows a significant martensite peak at ~44.4° while the welding curve exhibits a great austenite peak with barely any martensite peak. The quantitative phase fraction analysis in Table 4.2 has shown that the primary phases of the welding and button melting samples are similar with (35.4±1.5) % and (32.3±1.3) %, respectively. In other words, the total phase fraction of martensite and austenite in the two samples is similar. While the welded sample consists of a large amount of austenite (54.2 %) and small amount of martensite (10.4 %), the button melting sample shows roughly equal amounts of austenite and martensite. Besides the martensite peak, there is no other major difference between the two plots due to the same chemical composition. It is also believed that the phase fraction difference between the button melted sample and the welded sample can also contribute to the hardness difference as mentioned in section 4.4.

Table 4.2: Phase fraction of different phases for the welding and button melting samples.

Phase	Welded sample	Button melted sample
Martensite	10.4±1.3	35.2±1.5
Austenite	54.2±0.3	32.5±1.7
M_7C_3	31.5±1.1	30.0±1.0
$M_{23}C_6$	3.9±1.0	2.3±0.8

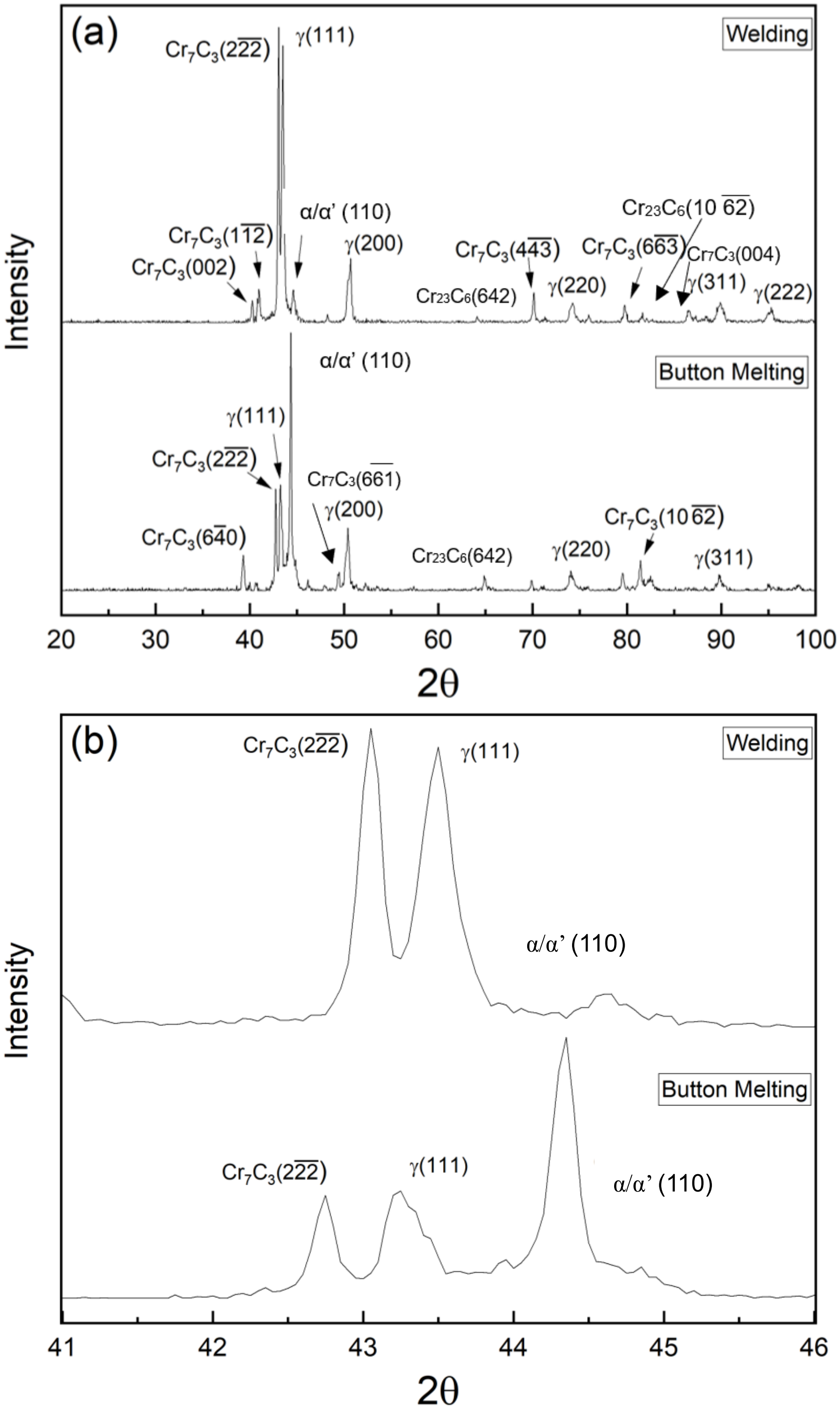

Figure 4.3: XRD patterns of top surface of (a) welding sample and button melting sample and (b) magnified plots for 2theta from 41 to 46 degrees.

4.6 Cooling Temperature Fields

The temperature fields of the button melting and welding experiments at the beginning of cooling are simulated using COMSOL software as shown in Figure 4.4. The material properties of the steel base metal in welding and the copper hearth in button melting used in the simulation are listed in Table 4.3 and 4.4. The data used was listed in the Material Contents in COMSOL Multiphysics [84]. The initial temperature of the button and weld is 1500°C which is higher than highest temperature of the first solidified carbide phase as predicted previously by Thermo-Calc simulation [85]. The initial temperature of the copper base is set as 25°C. The convective boundary condition was applied on the surface of both assemblies. In the case of water-cooled button melting, a 25°C temperature boundary condition was applied at the bottom of copper to simulate the water cooling during the experiment. A dilution of 40% volume was used for the welding sample while keeping the total volume the same. As shown in Figure 4.4, the temperature gradient in the button melting sample is mostly vertical due to the water cooling in the copper hearth, while the welding sample shows directional temperature gradient. In the real welding condition, the temperature gradient will be more random due to the influence of adjacent passes. Water cooling promotes the primary carbides to be preferentially oriented perpendicular to the surface [80]. However, there has not been any work that can strictly control the growth of primary carbides on the large scale as shown in Figure 4.1. The simulation has further justified that the temperature gradient difference in the different settings is the key to the control of primary carbides growth direction.

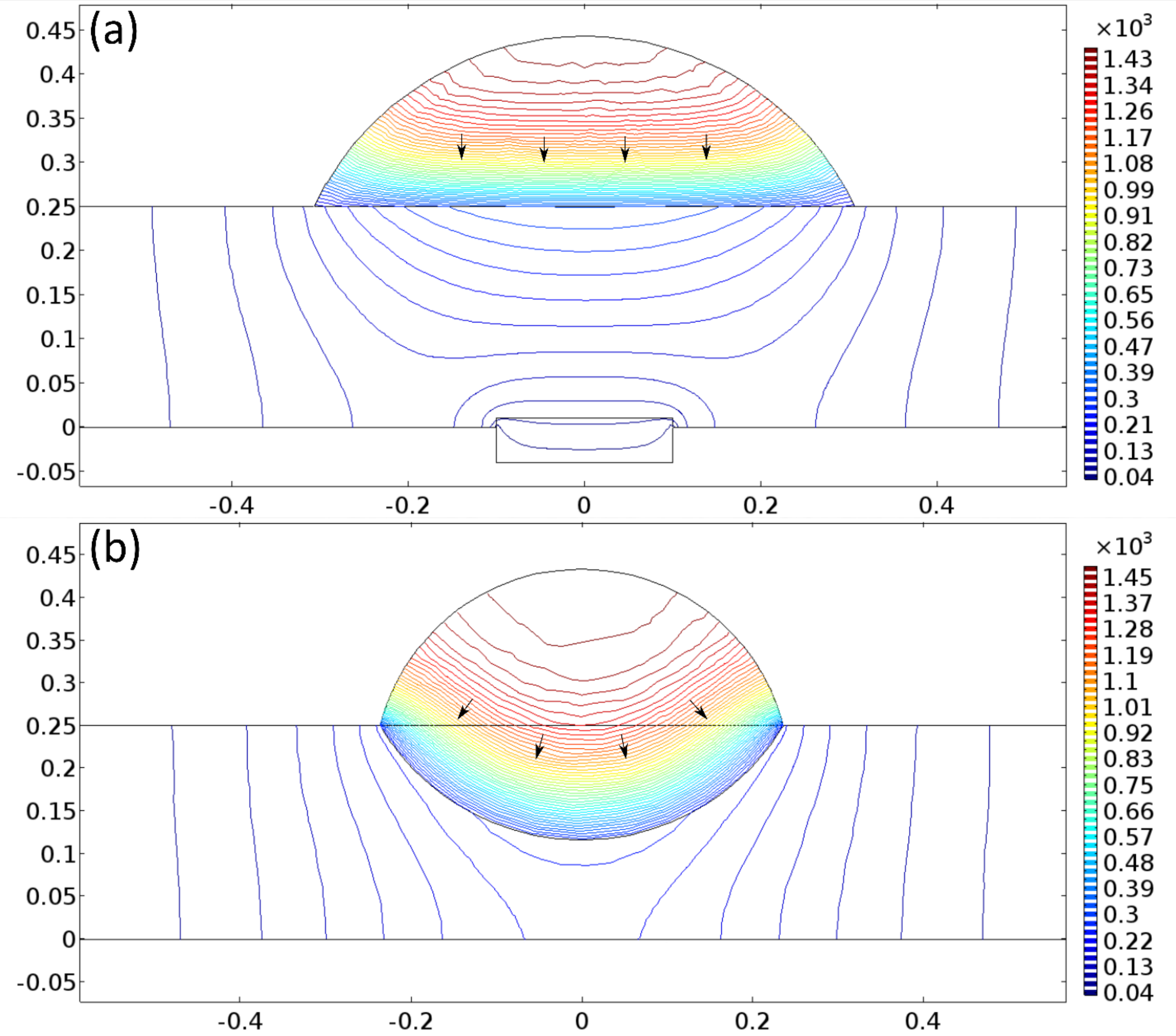

Figure 4.4: Simulated temperature fields of the button melted (a) and welded samples (b) near the solidus temperature of the overlay alloy. Arrows point to the temperature gradient directions. The cross-section area of the overlay is the same.

Table 4.3: Material properties used in COMSOL simulation.

Parameters	Steel	Copper
Heat capacity at constant pressure J/(kg·K)	475	Cp
Density kg/m^3	7850	8960
Thermal conductivity W/(m·K)	44.5	σ
Relative permeability	1	1
Electrical conductivity S/m	4.03×10^{6}	6.00×10^{7}
Coefficient of thermal expansion 1/K	1.23×10^{-5}	1.70×10^{-5}
Relative permittivity	1	1
Young's modulus Pa	2.05×10^{11}	$1.10E\times10^{11}$
Poisson's ratio	0.28	0.35

Table 4.4: Heat capacity (Cp) and Thermal conductivity (σ) values with respect to temperatures for copper used in Table 4.3.

Temperature K	Cp J/(kg·K)	Temperature K	σ W/(m·K)
200	356.1	100	482
250	374.1	200	413
298.15	385	250	406
350	392.6	300	401
500	407.7	350	396
600	416.7	400	393
		500	386
		600	379
		800	366
		1000	352
		1200	339

In summary, a welding overlay sample is obtained by flux-cored arc welding of the commercial CCO wire. The button melting method is developed to melt the commercial CCO short wire pieces. Button melting has proven to be a valid method to simulate the welding overlay with higher efficiency and lower design cost. The button melting method has shown more advantages over welding tests in overlay design in regard to raw material preparation and validation. Additionally, the obtained button melted microstructure shows uniformly distributed primary carbides and eutectics without any dilution from the base metal as in the welding condition. The orientation of primary carbide is in the vertical direction thanks to the fast cooling of the bottom copper hearth. The top surface of all the samples shows higher hardness than their cross-sectional surface. Therefore, the button melted sample shows superior hardness than the welding sample due to well-controlled primary carbide orientation and higher martensite fraction from fast cooling. As the button melting method may overestimate the performance of the designed CCO, it remains a valid and efficient method for the CCO design. This method will provide guidance on the benchmark performance given a chemical composition with the benefit of fast microstructure verification, no dilution, and controlled cooling. Therefore, the design and testing of various chemical compositions can be achieved in a fast and inexpensive way.

Chapter 5

Accelerated Design of Chromium Carbide Overlays via Design of Experiments and Machine Learning

5.1 Introduction

Chromium carbide overlays with MC-type primary carbides have shown great potential in wear and corrosion-resistant application with no crack formation in the welding application compared to traditional CCO with M_7C_3 primary carbides [86,50,87]. A lot of qualitative studies have shown that the MC-type primary carbides solidify before the primary M_7C_3 carbides resulting in the improvement of overall wear resistance [47,50,56]. However, there is no work to quantify the chemical composition influence of the carbide formers on the wear resistance due to the difficulties in controlling all other inputs during welding. Besides, hundreds of wear data with a variety of composition formulas are typically required to study the synergistic effects of the carbide-forming elements which is a tedious and costly process.

In this chapter, multiple overlay formulas that contain MC-type primary carbides and eutectic phases were designed and the samples were prepared using the arc furnace button melting method as described previously. Hardness is used as an indicator of wear resistance due to the good correspondence in this system [48,88]. In recent years, design of experiments (DOE) and machine learning techniques have proven to accelerate the materials discovery, and the traditional time-consuming and trial-and-error methods for wear rate prediction and experimental work can be eliminated [89–92]. However, no work has been done to develop an active database to show the influence of multiple MC carbide formers on the wear resistance of the CCOs quantitatively.

5.2 Material and Methods

A series of CCO formulas containing the same matrix was developed using the DOE approach as shown in Table 5.1. The objectives of the experiments, i.e., outputs, were defined as the hardness value of each formula. The variables, i.e., inputs, were the molar percentage of Nb, Ti, And V in the formulas, which were manipulated during the experiments. The molar percentage of Nb, Ti, and V varies from 0 to 100% with a total of 0.03 mole. A constant amount of high-carbon ferrochromium, ferromanganese, ferrosilicon, and pure iron powder was added for each formula. The total powder weight for each formula was about 50g. Since all MC carbides have a stoichiometric ratio of 1:1 (M:C), it was more valuable to compare their effects using the molar ratio instead of the weight ratio which is still used in most studies [48,93]. Besides, different elements were considered with various transfer coefficients during the melting or welding process. For example, Ti is so active that it will react with the air easily which prohibits Ti to transfer to the weld metal. Therefore, more Ti and V powders were added to compensate for the loss ratio of 33.3% for Ti and 10% for V [48]. To reduce bias and ensure that the results were not influenced by unknown variables, the order was randomized in which the experimental conditions are tested. The arc furnace button melting method was used to prepare the overlay samples and the details are reported previously. Vickers hardness tests were carried out using a 3kg load and 10s dwell time in order to obtain hardness results from the bulk of each sample.

When building the machine learning model, three-fold cross validation was used to choose between first and second order polynomial featurization using the negative root mean square error (RMSE) for scoring. First order polynomial features correspond to the original features, while creating second order polynomial features introduces the squares of each original feature, as well as interaction terms between each pair of original features as inputs for the model. Mean RMSE values across the three folds were 27.2 HV and 25.4 HV for the first and second order polynomial features respectively and so second order polynomial featurization was used in the final model, which was refit on the entire dataset. The machine learning model used was a linear regression with an intercept term, and since polynomial featurization was used this may be referred to as a generalized linear model.

Table 5.1: Overlay chemical compositions from DOE and machine learning model. ID #1 through #13 were used as input for machine learning to establish the model. ID #A, B, and C were randomly picked from the model predictions for model verification.

	Molar Ratio (%)	wt. % in overlay								Measured HV5		Predicted HV5	Prediction Variance
ID#	Nb:Ti:V	C	Cr	Mn	Si	Fe	Nb	Ti	V	mean	σ	mean	
1	60:30:10	3.1	23.4	2.1	2.1	64.7	3.5	0.9	0.3	550.0	16	-	-
2	60:10:30	3.1	23.4	2.1	2.1	64.6	3.5	0.3	0.9	546.8	16	-	-
3	30:60:10	3.1	23.7	2.1	2.1	65.1	1.8	1.8	0.3	581.6	14	-	-
4	30:10:60	3.1	23.8	2.1	2.1	64.9	1.8	0.3	1.9	602.2	28	-	-
5	10:60:30	3.2	24.0	2.1	2.1	65.2	0.6	1.8	1.0	630.0	15	-	-
6	10:30:60	3.2	24.0	2.1	2.1	65.1	0.6	0.9	1.9	642.4	16	-	-
7	50:50:0	3.1	23.5	2.1	2.1	64.9	2.9	1.5	0.0	574.4	5	-	-
8	0:50:50	3.2	24.1	2.1	2.1	65.3	0.0	1.5	1.6	626.4	21	-	-
9	50:0:50	3.1	23.5	2.1	2.1	64.7	2.9	0.0	1.6	578.0	13	-	-
10	100:0:0	3.0	23.0	2.0	2.0	64.3	5.6	0.0	0.0	503.4	7.9	-	-
11	0:100:0	3.2	24.1	2.1	2.1	65.5	0.0	3.0	0.0	698.2	27	-	-
12	0:0:100	3.2	24.2	2.1	2.1	65.1	0.0	0.0	3.3	662.6	23	-	-
13	33:33:33	3.1	23.7	2.1	2.1	65.0	1.9	1.0	1.1	639.0	11	-	-
A	29:68:3	3.1	23.7	2.1	2.1	65.1	1.7	2.0	0.1	606.6	11	607.4	-0.1%
B	18:39:43	3.2	23.9	2.1	2.1	65.1	1.0	1.2	1.4	629.6	13	608.6	3.5%
C	31:3:66	3.1	23.8	2.1	2.1	64.9	1.8	0.1	2.1	607.0	5	606.8	0.0%

5.3 Results

A Thermo-Calc calculation is used to design and verify the target microstructures. Due to the high formation energy, the MC carbides (FCC_A1#2) are the first phases that solidify from the liquid. From Figure 5.1(a) and (b), the formation temperatures are 1619°C and 1707 °C for NbC and TiC, respectively. Following the solidification of MC carbides, the eutectic phases, i.e., austenite (FCC_A1) and M_7C_3 carbides, form at almost the same temperature (about 1300°C). For a more generic case (ID#1) in which all three types of carbide formers exist, the formation temperature of primary MC carbides and eutectic phases are similar at 1690 °C and 1300 °C (Figure 5.1(c)), respectively. The pro-eutectic M_7C_3 is small in fraction and negligible. Therefore, a microstructure with a single primary phase (MC) is achieved.

A typical microstructure of ID #1 with EDX maps of Nb, Ti, and V is shown in Figure 5.2. The overlay exhibits a microstructure with primary MC-type carbide with a matrix of eutectic phases consisting of austenite and M_7C_3 carbides. As predicted by Thermo-Calc simulations, no visible M_7C_3-type primary carbides were detected. The partition for the three carbide formers is very strong. Due to the relatively low concentration of Nb, Ti, and V, the MC phase cannot be detected by XRD analysis. The sample was then immersed in the Villela reagent for 168 hours to dissolve the Fe-rich phases. As seen in Figure 5.3, the eutectic M_7C_3 network with MC carbides has been obtained after the dissolution. The XRD plots in Figure 5.4 have rarely shown austenite peaks and the eutectic M_7C_3 and NbC phases have dominated.

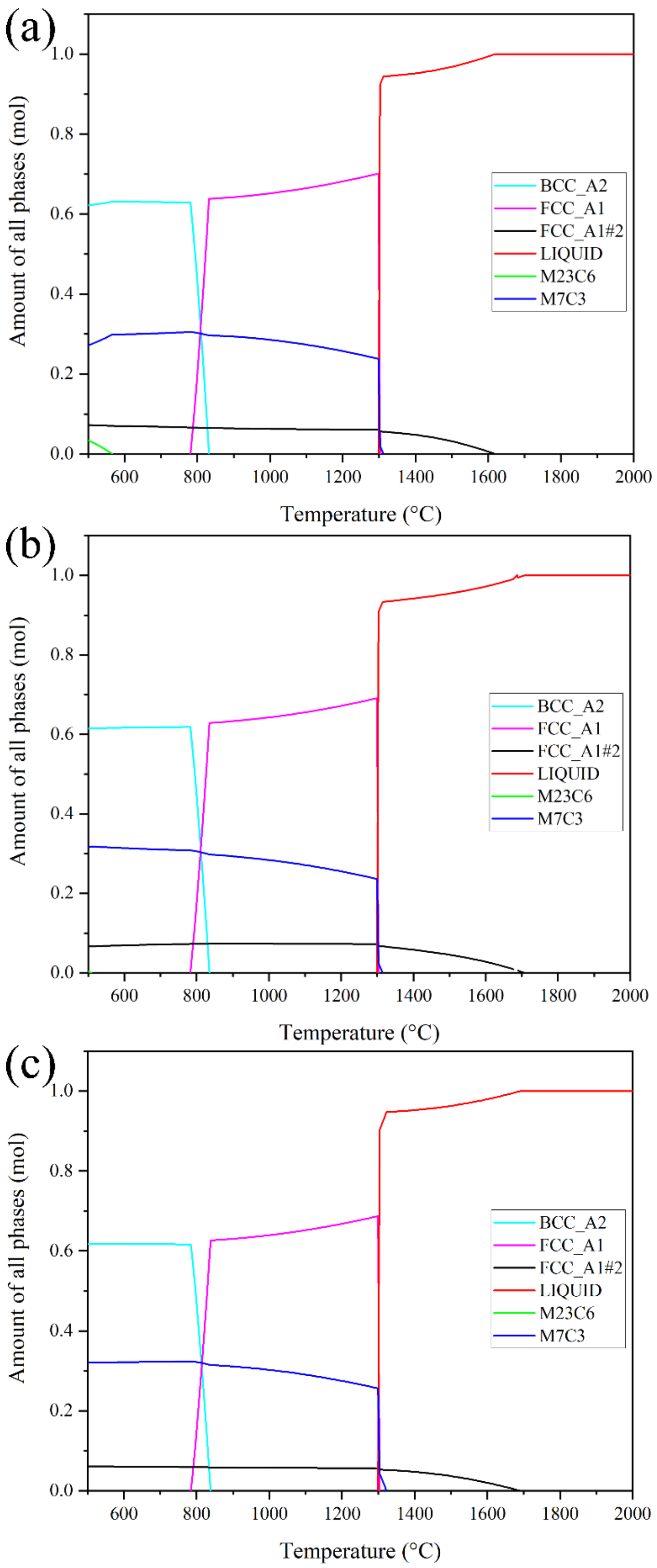

Figure 5.1: Thermo-Calc calculation of overlay sample ID #10 (a), #11 (b), and #1 (c).

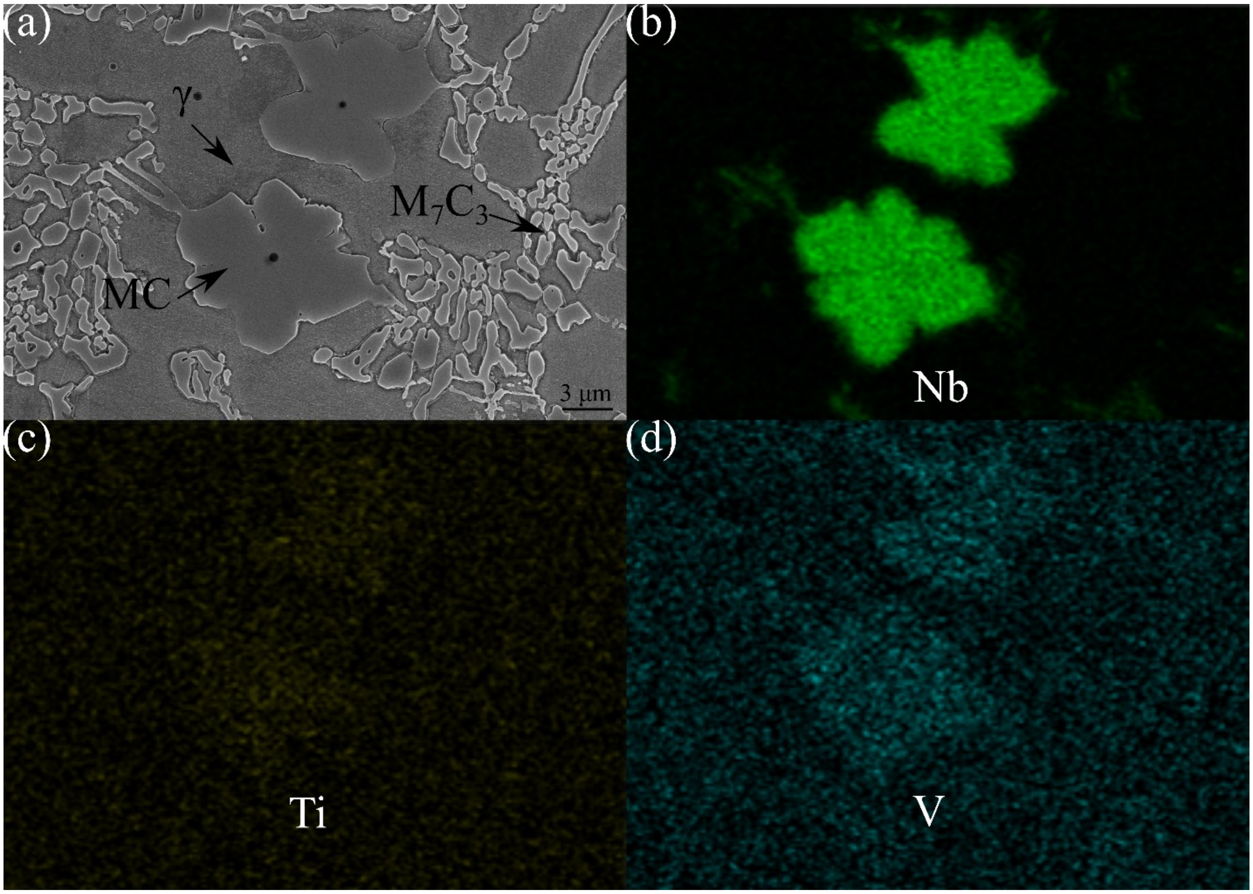

Figure 5.2: Secondary electron image of the as-melted structure of (a) ID #1 sample, (b), (c), and (d) are Nb, Ti, and V EDX maps for sample #1 with the same magnification as (a), respectively.

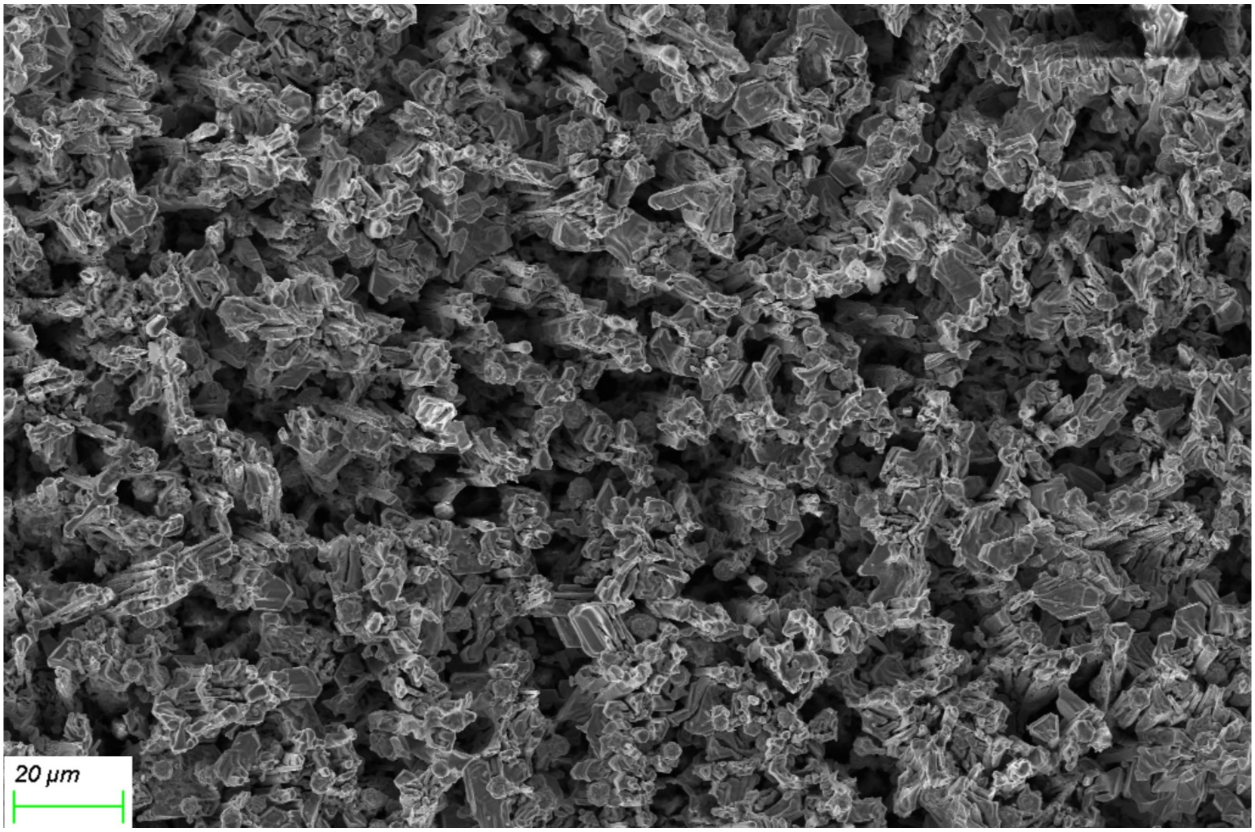

Figure 5.3: Secondary electron image of ID #1 sample after deep etching.

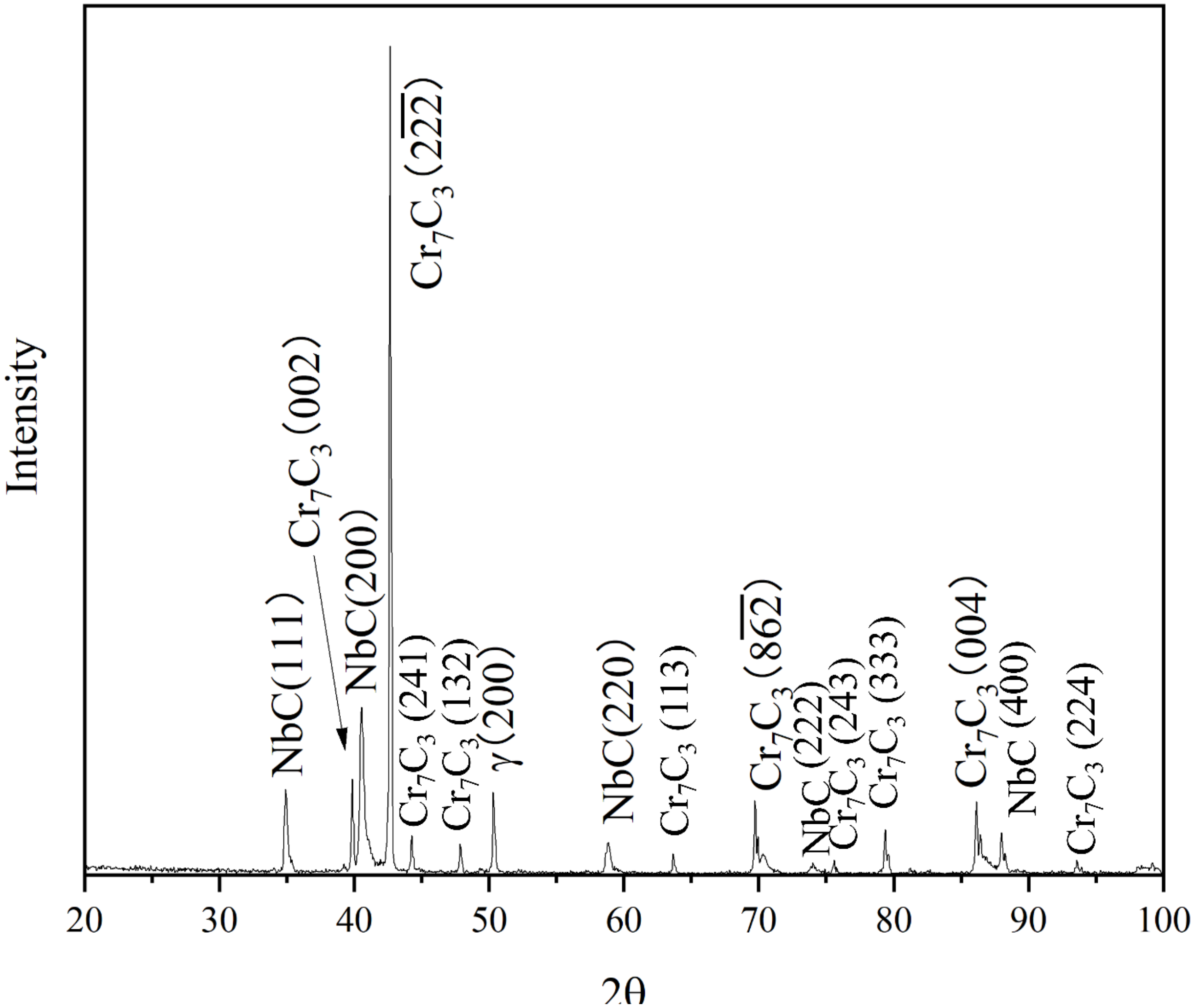

Figure 5.4: XRD pattern of the deep etched ID #1 sample.

The 13 data sets in Table 5.1 were used as input for machine learning by a simple generalized linear model strategy. As seen in Figure 5.5(a), the prediction matches the measurement very well. Analysis of variance (ANOVA) was used to evaluate the relative importance of each parameter given by the percent contribution to the overall hardness (Figure 5.5(b). Nb contributes the most (roughly 51%) to the hardness, meaning adding or eliminating Nb will have the biggest effect on the final hardness. Ti and V contribute about 31% and 18% to the overall hardness, respectively.

To build the machine learning model, a standard scaler is used to process the data, followed by creating the polynomial input features and applying all the features to a regularized linear model as shown in the Appendix. The triangular map is then plotted to visualize the relationship between three carbide formers and the overlay hardness as shown in Figure 5.5(c). The edges of the triangle stand for the molar concentration of Nb, Ti, and V from 0 to 100%. With the increase of Ti concentration, the hardness increases the most, followed by V and Nb. The model predicts the hardness by providing the chemical composition. And from another perspective, within a target hardness range, it allows for choosing the desired chemical compositions.

To test the model, 3 points in the same hardness band were randomly chosen on the map with the hardness as ID #A, B, and C in Table 5.1. The overlay is then prepared using the same method and the measured hardness values are listed in Table 5.1.

The difference between the predicted values in the model and the measured values is considerably low within ±3.5%. By using the three sets of new data as new inputs, a feedback loop is developed to update and tune the model. As shown in Figure 5.2(d), the new hardness contour near the area of sample ID #A and #C remains almost unchanged. The curvature of the contour is increased due to the underestimation of hardness for ID #B. In this way, an interactive closed feedback loop is built to serve the design purposes. In the real-life application, this model is to be more accurate for prediction as more data are added.

X-ray diffraction (XRD) was used to analyze the phase formation that contributes to the overall hardness. As seen in Figure 5.6, the overlay shows similar types of phases of austenite and Cr_7C_3. Since the percentage of carbide formers is low, there are no MC peaks with intensity distinctions except for NbC. Sample #10 shows the strongest austenite peak followed by sample #12. Even though sample #11 shows the weakest austenite peak, the ferrite/martensite peak appears the strongest. As retained austenite is the softest phase in the overlay between (430 and 600 HV) [46], more austenite tends to lead to lower hardness. On the other hand, Ti promotes the formation of martensite (hardness between 600 and 850 HV [46]) during air cooling to harden the matrix which is believed to be the main reason why the Ti corner in Figure 5.5(c) shows the highest hardness.

Another factor is that the intrinsic hardness order is TiC > VC > NbC for the three types of carbides [94–96]. Therefore, under the assumption that the as-received overlay contains the same molar fraction of MC carbide, sample #11 has the highest hardness followed by #12 and #10.

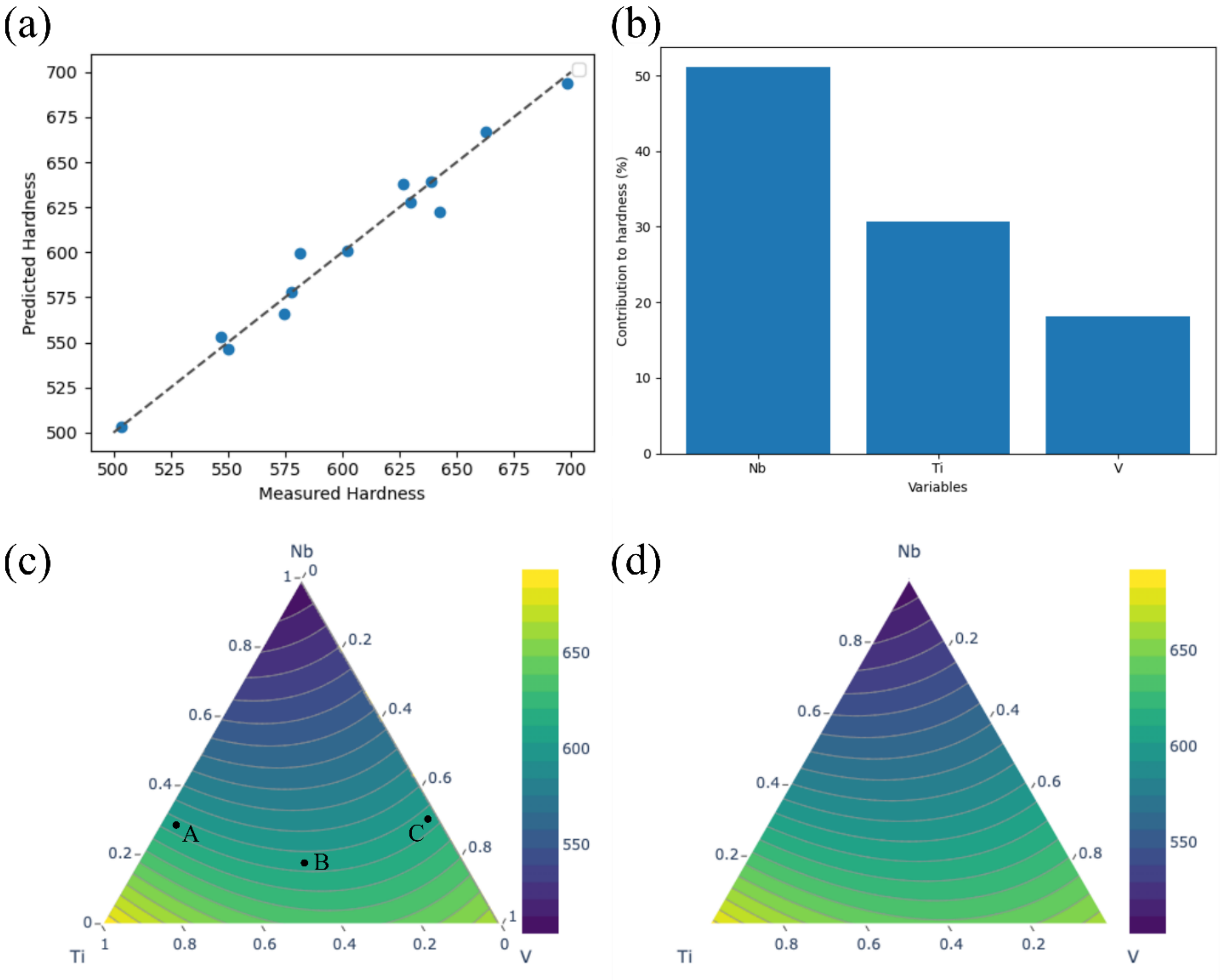

Figure 5.5: (a) The predicted hardness as a function of the observed hardness. (b) ANOVA analysis showing the individual contribution of the three elements to hardness. (c) Contour map of microhardness as a function of chemical composition. (d) Updated contour map after adding the new data of samples ID #A, #B, and #C.

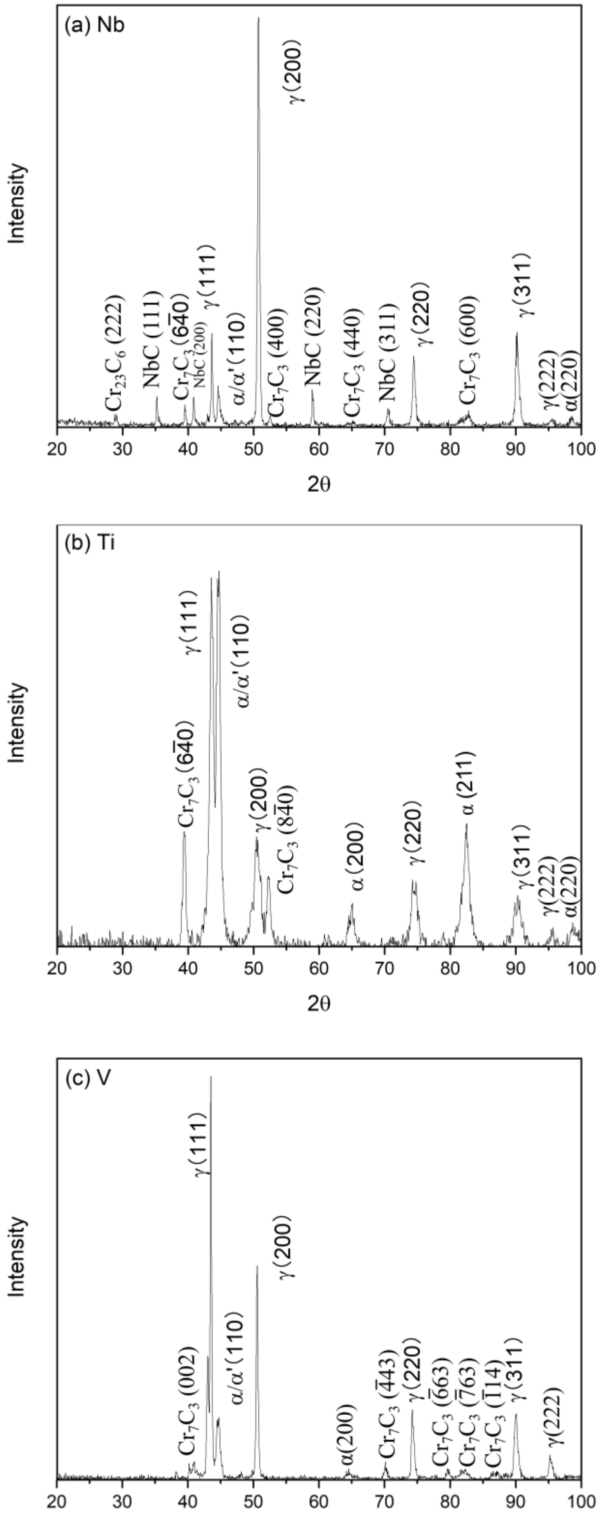

Figure 5.6: XRD pattern of (a) sample #10 with only Nb addition, (b) sample #11 with only Ti addition, and (c) sample #12 with only V addition.

5.4 Conclusions

In summary, a series of overlays with MC-type primary carbides and eutectic matrix were designed to study the effect of chemical composition on overlay hardness by using DOE. The partition of Nb, Ti, and V formers is very strong to form MC-type primary carbides. A machine learning model was developed to visualize the relationship between the chemical composition input and hardness output. This model provides quantitative guidance on how the strong carbide formers contribute to the overlay hardness in the same matrix. With the same amount of carbide formers, Ti addition increases the overlay hardness the most followed by V and Nb. New data was extracted from the tool to verify and tune the model to establish a closed feedback loop. XRD analysis shows that Nb would promote the formation of austenite in the matrix while Ti would foster the formation of martensite to harden the overlay. This method provides a new approach to the fast design of the chemical composition of chromium carbide overlay.

Chapter 6

Solidified Microstructure of a Novel Wear-Resistant Fe-Cr-C-B Overlay

6.1 Introduction

Overlaying is a surface treatment that applies a metallic coating on the engaging surface of a given component. There are various methods to apply the overlay, among which welding overlay is efficient and inexpensive. Common welding overlay methods include, but are not limited to, flux-cored arc welding [97], submerged arc welding [98,99], plasma transferred arc welding [20,100], and gas metal arc welding [101,102]. Depending on the composition, the as-solidified overlay can have a hypoeutectic, eutectic or hypereutectic microstructure. The hypereutectic overlay contains higher levels of alloying elements and is often used in severe wear applications. The hypereutectic microstructure consists of carbides as the primary phase, austenite or ferrite as one eutectic component and often a networked carbide as the other eutectic component [103]. The main hard phase for the chromium carbide overlays is generally the M_7C_3 carbide. The strong but brittle M_7C_3 carbide has a hexagonal cross section and can grow relatively long in the c-axis to form a “pencil”-shaped morphology. It has been reported that the hypereutectic overlays tend to contain relief cracking in the transverse direction of the overlay because of the contraction of the weld pool upon solidification cooling [104] and poor ductility of the carbides; as a result, the cracked coating will show premature failure in a corrosive environment when the corrosive solution can penetrate into the base metal through the cracks.

The nickel tungsten carbide (Ni-WC) system is another commonly used hypereutectic system. Due to the high-volume fraction of tungsten carbide hard particles and nickel matrix in the overlay, it usually shows good wear and corrosion resistance [105]. However, it is generally also the most expensive system. Compared with the Ni-WC overlays, the iron-based chromium carbide overlay system has a lower cost, great flexibility as a welding filler metal and potential for excellent erosion-corrosion resistance due to its high chromium content.

The hypoeutectic overlay, on the other hand, consisting of a lower level of alloying elements, solidifies into primary austenite or ferrite and the eutectics. As a consequence, the hypoeutectic overlay shows a superior weld cracking resistance but relatively low wear resistance due to the lower volume fraction of hard phases [106].

The chemical composition of major alloying elements and additions of minor alloying elements have complex effects on the eutectic alloy microstructure. The effect of Ti, Nb and Mo on the steel welding coating was studied in strong carbides for the enhanced wear resistance [56,64]. As strong carbide formers, these elements would consume the carbon in the molten pool in the early stage during cooling. The eutectic phases would form after the formation of primary hard phases. It is reported that the oriented M_2B boride

(M represents Cr and Fe) crystals would show excellent slurry erosion resistance compared with carbides [61,63,107]. If controlled well, the M_2B eutectic structure has the potential to provide an excellent combination of properties. However, the challenge is still how to design an overlay solidified microstructure that has welding crack resistance as good as that of a hypoeutectic system and wear performance as good as that of a hypereutectic system.

A balance is required considering that a higher content and greater size of carbides in an overlay would give greater wear resistance but also would lead to a higher crack tendency, higher cost and often a lower corrosion resistance [72]. Thus, the optimized overlay system should contain a fair amount of primary hard phases that provide the wear resistance. In addition, the morphology and size of the primary hard particles need to be optimized so that they will not break easily during abrasion wear. The overlay should contain a significant fraction of primary austenite (a steel matrix) that is relatively ductile to help prevent crack formation. The networked eutectics should be uniformly distributed, which bridges other phases together. A good selection of the chromium level is also critical to the corrosion performance.

In this chapter, we report a novel iron-based overlay system produced by flux-cored arc welding to apply in the wear and corrosion environment. The primary MX-type hard particles are formed first, followed by formation of austenite dendrites and lastly M_2B-containing eutectics. The overlay microstructure is fully characterized as hypereutectic based on the primary carbide dendrites; paradoxically, it can also be considered hypoeutectic based on the solidification of primary δ-ferrite/austenitic dendrites. The formation mechanism of this complex microstructure in the novel overlay is discussed.

6.2 Material and Methods

Two custom-designed overlay weld wires were applied to a 1/2 inch (12.5 mm)-thick mild steel tube inner diameter by self-shield flux-cored arc welding. The chemical composition of Wire 1 was that of a typical chromium carbide overlay, roughly consisting of 30.0% Cr, 4.0% C, 2.0% Mn and Si each, and balance Fe. The main alloying elements in Wire 2 included 20.0% Cr, 1.0 to 2.0% C, 1.0 to 4.0% Nb, 2.0% Mn and Si each, < 2.0% Ti, Mo and B each, and balance Fe. Note that the amounts mentioned in this chapter were all based on weight percent. As a composition containing very complex chemical composition, Wire 2 provides a unique formula that is different from any stainless-steel consumables or hardfacing consumables such as Lincon Weartech SHS 9800U and 9700U, Stoody 965-G and 965-O, Welding Alloys Hardface Aprail-O, etc. As a result, the overlay can exhibit a more complex microstructure as discussed in the later sections. The 2-mm-diameter wires were welded using 200-240 A and 20 V arc voltage without any preheat or post-weld heat-treatment. Multiple welding layers were deposited. The cross-sectional samples of the overlayed steel tube were cut using the abrasive saw with water cooling and then prepared for metallurgical samples as described in Chapter 3. The microhardness tests across the weldment cross section were conducted with test force of 0.5 kgf and dwell time of 10 s on a Wilson VH3100 hardness tester. A matrix of indentations was made to collect multiple hardness data across different zones including base metal, HAZ, the first overlay layer and second overlay layer. The microstructure of the sample was examined by an optical microscope, scanning electron microscope, and electron backscatter diffraction as mentioned previously.

The area fractions of various phases and carbide size were measured using ImageJ software. Phase identification of the top surface of the overlay was performed by X-ray diffraction (XRD) with a scanning angle (2h) of 20 to 100° with a sampling width of 0.05° on a Rigaku Ultima IV X-ray diffractometer with a Cu Ka source at a scan rate of 1°/min. XRD could obtain all the phase information of the bulk material inclusively; therefore, it was helpful to extract the matrix phase signal and improve the identification of primary carbide and eutectic phases. The overlay specimen was immersed in the Villela reagent for over 2 days at room temperature as described previously. It was then washed and dried and underwent XRD scanning on the same surface to compare with the bulk analysis. Rietveld refinement of raw XRD data was carried out using an open-source software Profex-BGMN [71] to deconvolute the peaks sharing similar 2θ ranges and to identify and quantify the phases present in the overlay system. It is noted that the ferrite phase (α) and martensite phase (α’) share similar lattice parameters and the peaks for the two phases are typically overlapping. The overlapping peak indexed in this thesis have been marked as α/ α’. The semi-quantitative phase fraction was produced by deconvoluting the peaks by the software where the goodness of fit (GOF) value is close to 1 in order to provide non bias results.

6.3 Results

The as welded overlays produced using Wire 1 and 2 are shown in Figure 6.1. It is well acknowledged that the commercial CCO by Wire 1 shows transverse cracks as shown in Figure 6.1 (a). The overlay produced by Wire 2 shows no cracks on the surface as shown in Figure 6.1 (b).

The microstructure of the CCO produced by Wire 1 is shown in Figure 6.2. The as-solidified overlay shows a typical hypereutectic microstructure with large hexagonal M_7C_3 carbide particles surrounded by a matrix of finer eutectic M_7C_3 carbide and eutectic austenite.

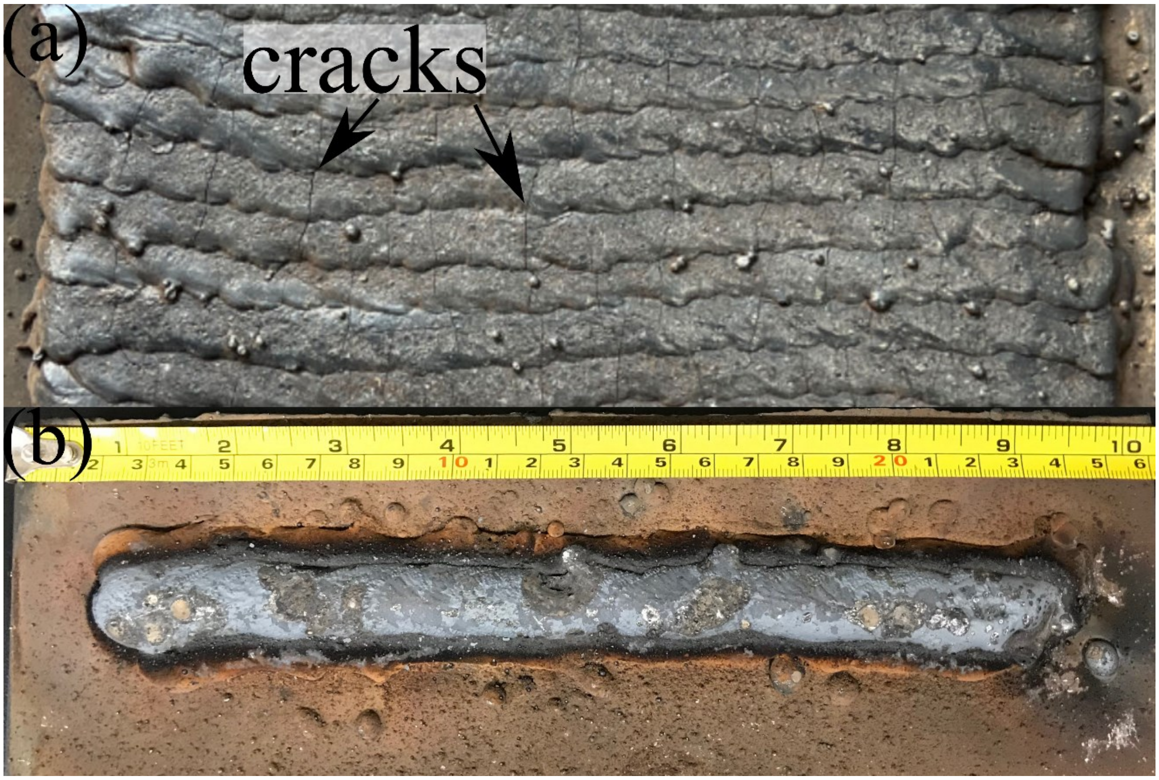

Figure 6.1: As welded overlay by (a) Wire 1 and (b) Wire 2.

However, the microstructure of the Wire 2 overlay displays a complex hypereutectic microstructure that consists of a fine granular primary phase, a dendritic austenite (which later has transformed into martensite) and a eutectic network of austenite and secondary hard phases (Figure 6.3). Measured using the ImageJ software, the primary hard phase and eutectic phases have an area percentage of 4.7 ± 0.4% and 22.4 ± 0.2%, respectively. The primary hard phase has an average size of 2.1 ± 0.1 μm and is found to have the MX-type (M = Nb, Ti, Mo; X = C, B) crystal structure in later sections. The dendritic austenite regions appear bright in Figure 6.3(b). No cracks are observed in any of the overlay cross sections.

The microhardness values measured on the top surface of the Wire 1 overlay and various locations at the first layer, second layer and top surface of the Wire 2 overlay are summarized in Table 6.1. The average hardness of the Wire 1 overlay is 867 HV0.5. For the Wire 2 overlay, due to the base metal dilution effect, the hardness of the first overlay layer is less than that of the second layer with an average Vickers hardness of 600 and 732 HV0.5, respectively. At the top surface, the dilution effect is minimized, which results in a higher microhardness value of 825 HV0.5.

Table 6.1: Microhardness (HV0.5) of Typical Chromium Carbide Overlay by Wire 1 and Overlay by Wire 2.

Wire 1 Overlay		Wire 2 Overlay	
Top Surface	1st Layer	2nd Layer	Top Surface
867 ± 32	600 ± 23	732 ± 32	825 ± 33

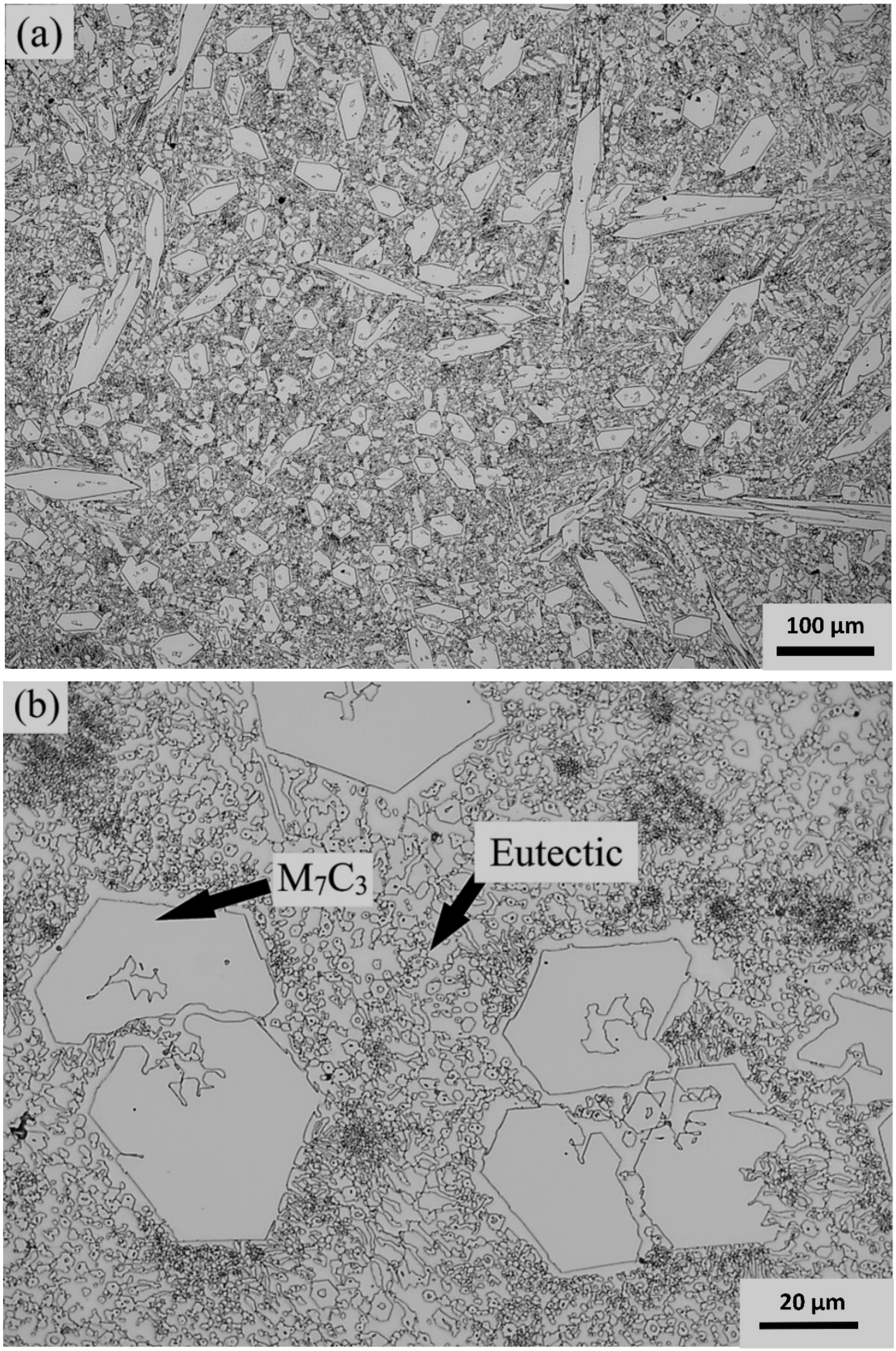

Figure 6.2: Optical microstructure of the Wire 1 overlay, showing a traditional chromium carbide overlay structure, (*a*) at low magnification and (*b*) at higher magnification.

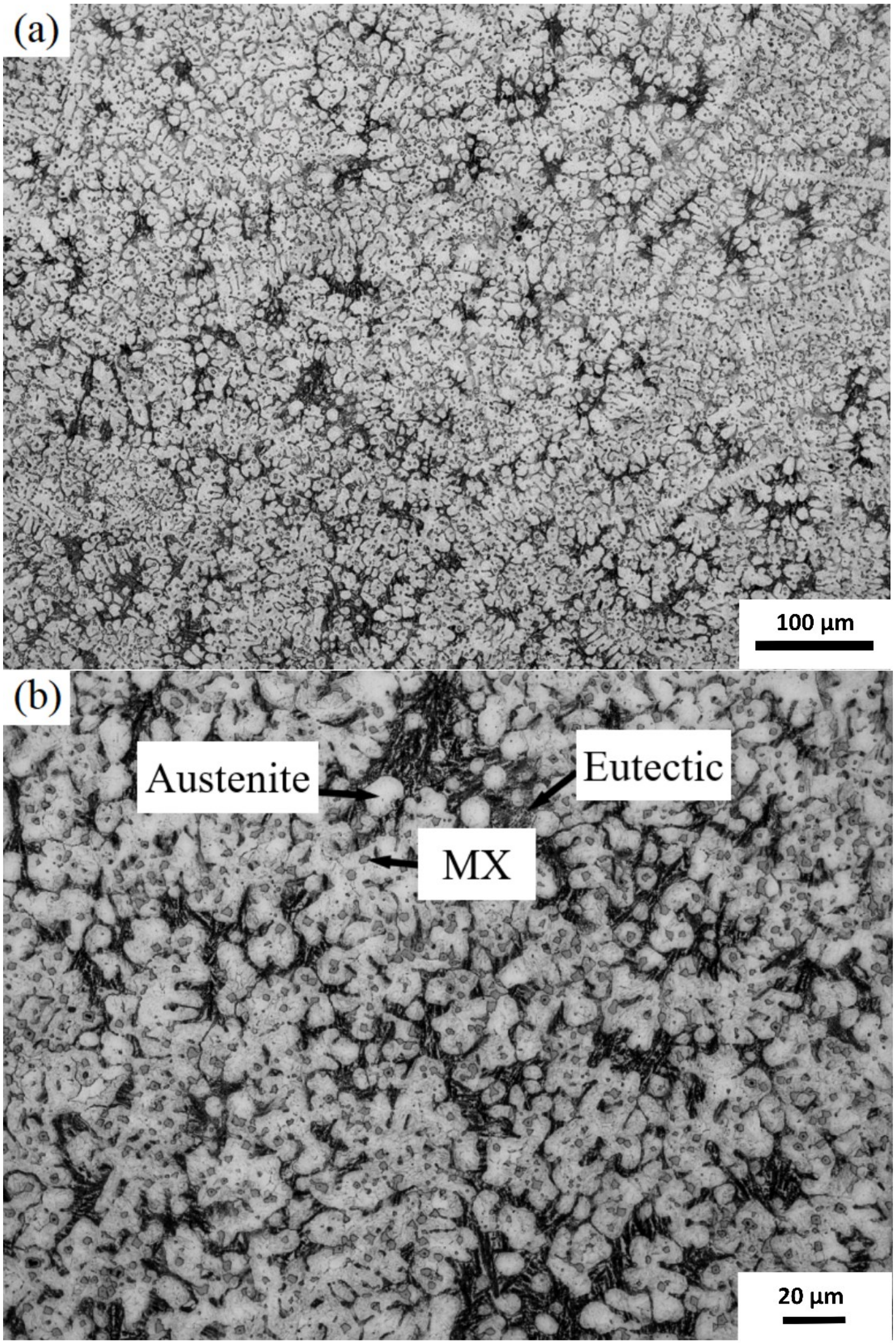

Figure 6.3: Optical microstructure of the Wire 2 overlay top surface at (*a*) lower magnification and (*b*) higher magnification.

XRD phase identification was conducted on both the Wire 1 and Wire 2 overlay samples. First, in the Wire 1 overlay, it was confirmed that M_7C_3 is the primary and eutectic carbide (Figure 6.4). The strongest diffraction peak is for austenite (111); the second strongest diffraction peak is for ferrite/martensite.

The Wire 2 overlay sample, on the other hand, shows the strongest diffraction peaks for the (110) $\alpha/\alpha'$and (211)α/α'planes of martensite, and minor peaks for Fe_2B, NbC and austenite (Figure 6.5(a)). Deep etching of the Wire 2 overlay was carried out to dissolve the matrix martensite. Figure 6.5(b) shows that when the matrix has been dissolved by deep etching, the NbC and Fe_2B peaks are prominent. No peaks from martensite are observed anymore; however, weak austenite peaks are still visible after deep etching.

Figure 6.6(a) shows the backscattered electron image of the top layer of the Wire 2 overlay with a hypereutectic microstructure consisting of primary MX-type carbide particles, austenite/martensite dendritic grains and eutectic networks. After deep etching, the iron-rich phases such as austenite, ferrite, and martensite have been dissolved and left with a three-dimensional eutectic network and some remnant primary particles adjacent to the eutectic (Figure 6.6(b)). At a higher magnification, the lamellar structure of the eutectic consisting of eutectic carbides and austenite is clearly seen in Figure 6.7.

The distribution of various elements and phases in the Wire 2 overlay is shown in Figure 6.8. The EBSD phase map in Figure 6.8(b) confirms that the primary hard phases consist of MX phases (green region). To evaluate the local strain distributions in the overlay, a kernel average misorientation map is plotted in Figure 6.8(c). It shows that there is large misorientation in the prior austenitic dendritic regions, indicating that the BCC ferrite detected by EBSD (red regions in Figure 6.8(b)) is martensitic in nature, further confirming the XRD results. As shown in Figure 6.8(d)–(i), the primary MX carbide is found to be rich in Nb, Ti, Mo, C and B, while the eutectic M_2B boride is found to be rich in Cr and B.

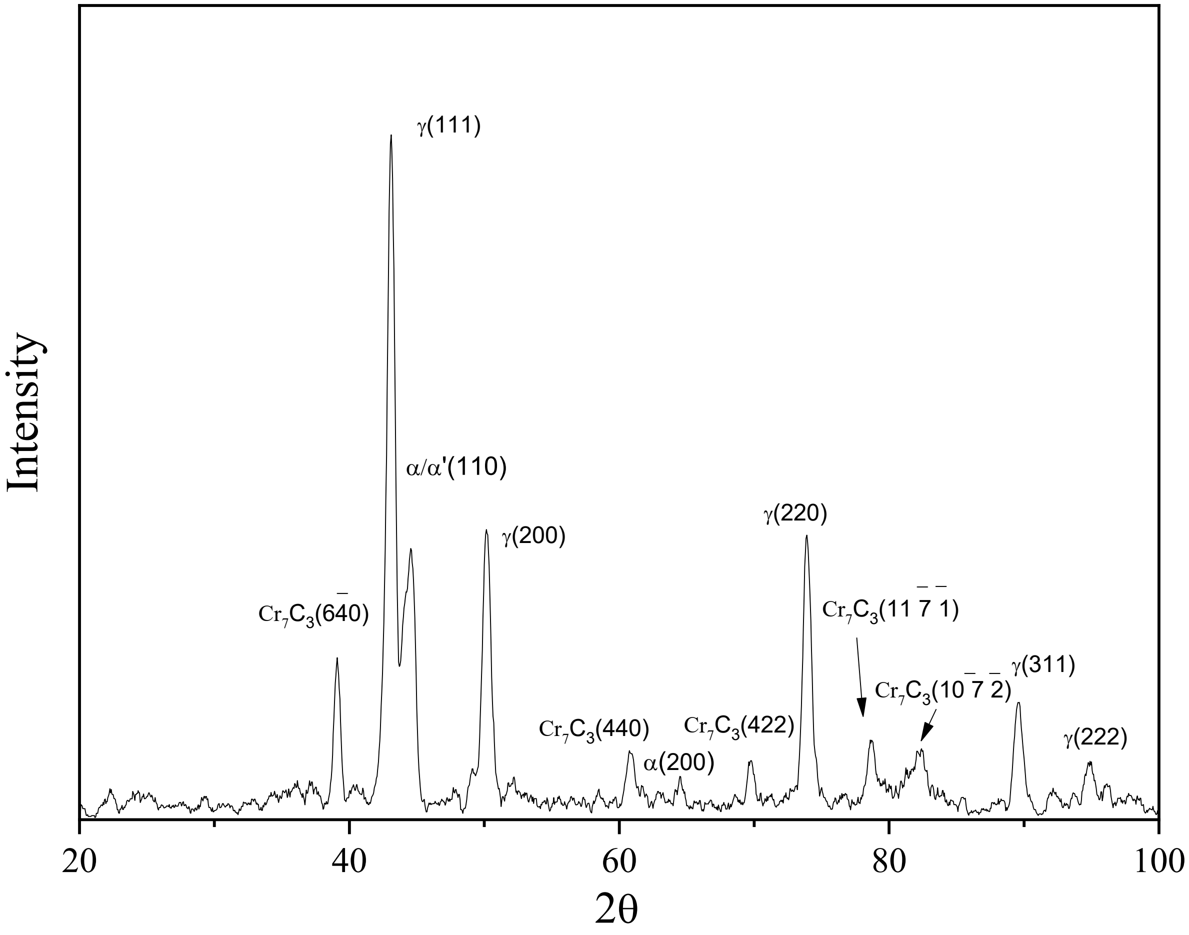

Figure 6.4: X-ray diffraction patterns of typical CCO overlay by Wire 1.

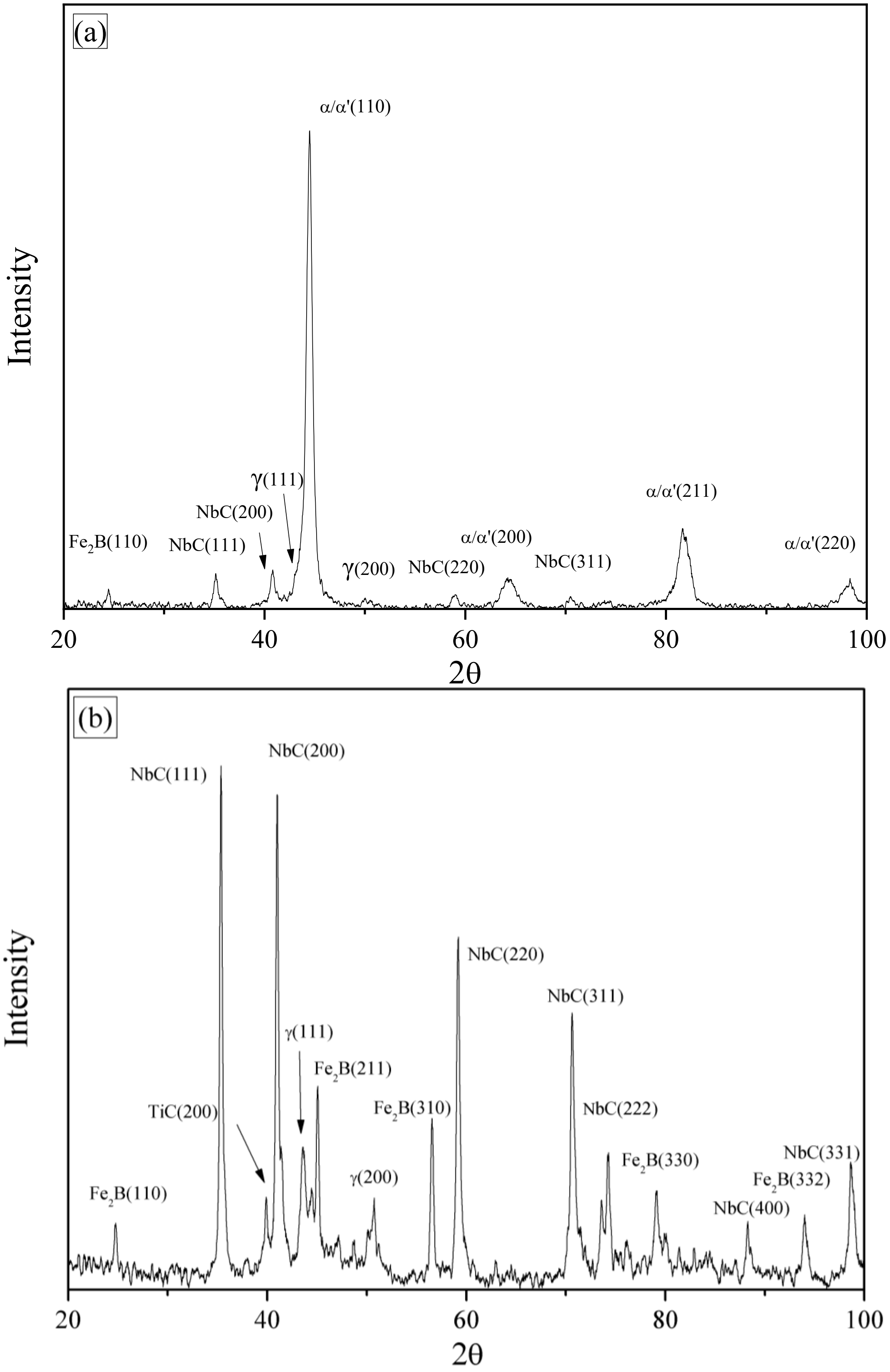

Figure 6.5: X-ray diffraction patterns of Wire 2 overlay (a) without matrix dissolution and (b) with matrix dissolution by deep etching.

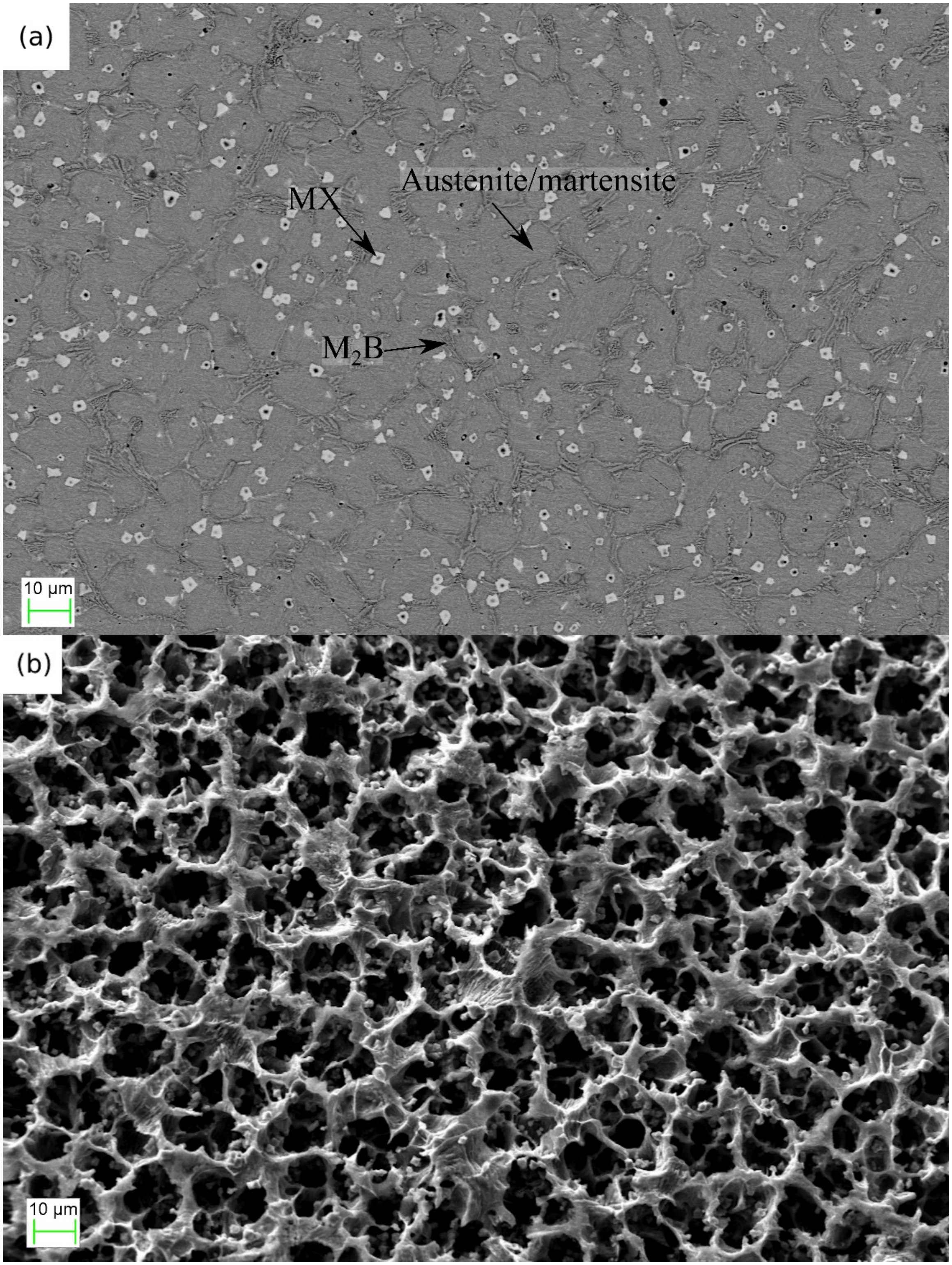

Figure 6.6: SEM images of the overlay top layer of Wire 2: (a) backscattered electron image before deep etching, (b) secondary electron image after deep etching, under the same magnification as for (a).

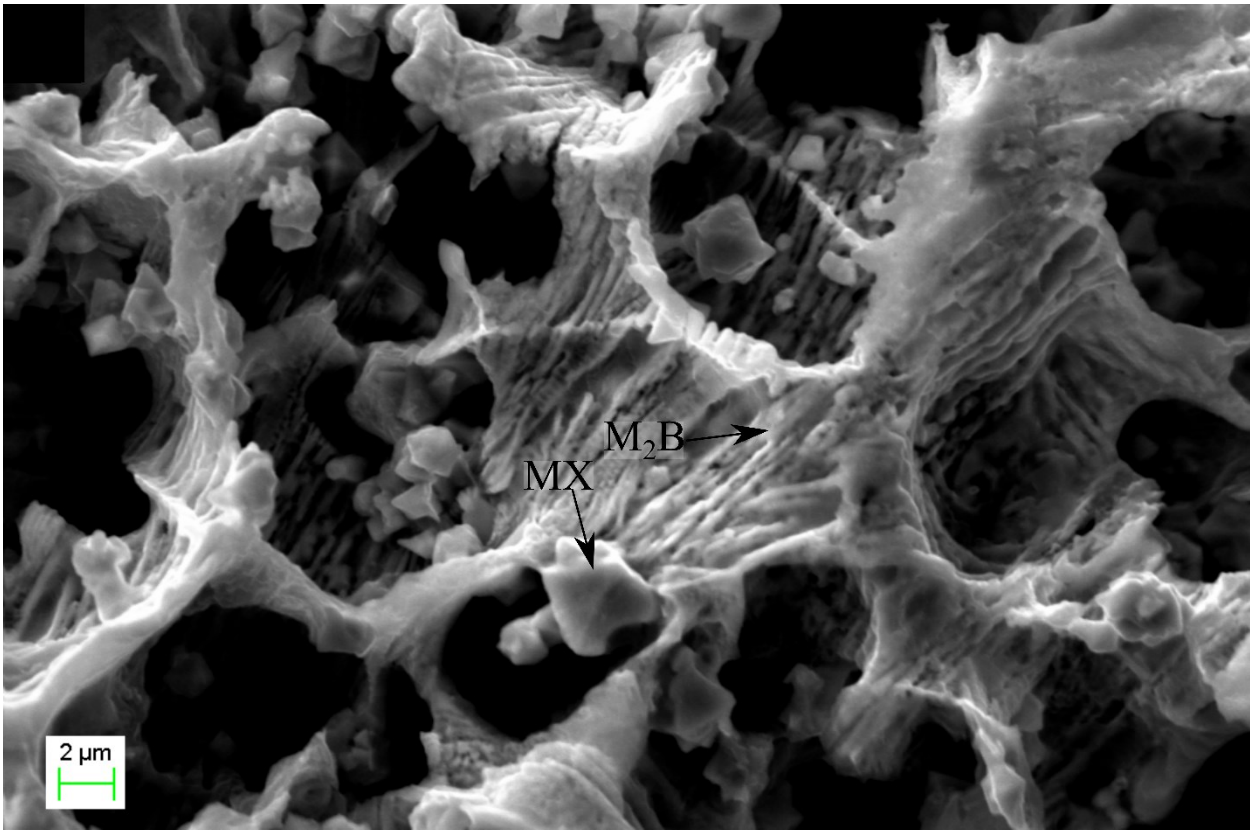

Figure 6.7: Secondary electron image after deep etching, showing the lamellar eutectic network with primary carbides under higher magnification.

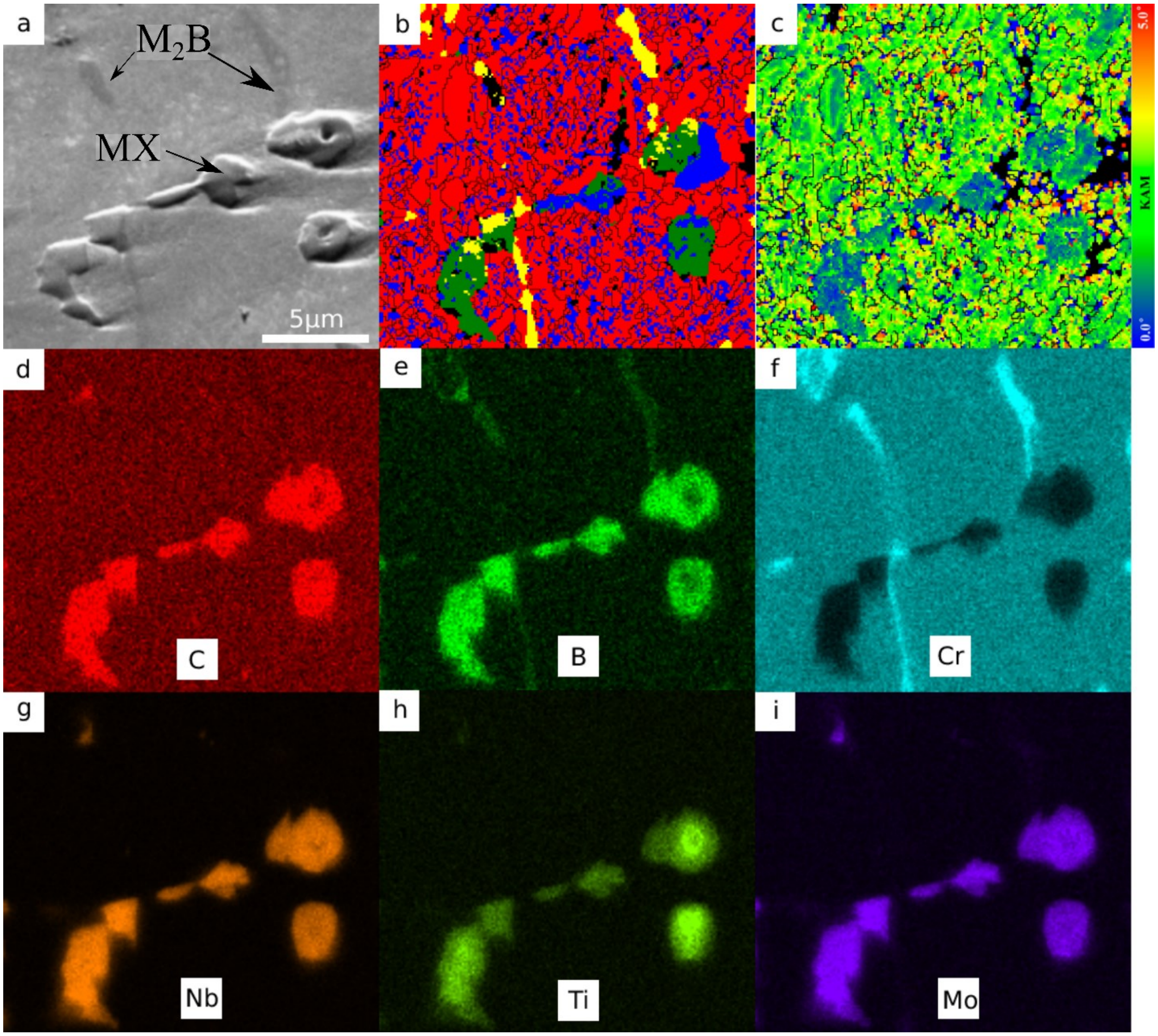

Figure 6.8: EBSD and SEM/EDX analysis of the top overlay layer of Wire 2. (a) SEM secondary electron image, (b) EBSD phase map of the selected area in which red represents BCC phases, green represents MX phases, yellow represents M_2B phases, blue represents other carbides including $M_{23}C_6$ and M_7C_3, and black represents non-indexed areas. (c) Kernel average misorientation map of the selected eutectic area. (d)–(i) EDX maps of various elements, C, B, Cr, Nb, Ti and Mo, respectively.

An EDX line-scan analysis of the primary carbide particles in the Wire 2 overlay is presented in Figure 6.9. It confirms that the MX phases are rich in C, Nb and Ti, while it also finds that the core of the MX particle is rich in Al and O, which suggests the core to be Al_2O_3. Comparing the Ti and Nb scans, it is found that the outer surface of the particle is richer in Nb and the inner surface is richer in Ti. It is noted that some MX primary particles contain a darker core, which indicates a segregation of lighter elements under the backscattered electron mode. Some studies have identified similar structures in the M_7C_3-type primary carbide [103,108].

The size of Al_2O_3 is found to be up to 1 μm. Except for the Al_2O_3 found in the core of primary carbides, there were no isolated Al_2O_3 particles detected in the microstructure of the bulk overlay. Aluminum was not intentionally added as an alloying element, but rather as a common deoxidizer to the flux-cored welding wire to protect the overlay from oxidization. It is believed that the high melting point (2072 °C) Al_2O_3 inclusions may have served as the first solid phase during welding solidification [109]. These inclusions may act as nucleation sites for the primary MX particles. During this process, TiX forms first followed by NbX on the outer surface. However, no systematic study has been done to study the effect of Al on the carbide size. This will be further investigated in the later section. It is also believed that TiN may form during this process. However, no clear evidence was found in the samples.

Figure 6.10 shows the SEM micrograph and EBSD analysis of the selected area containing a eutectic colony in the Wire 2 overlay. As shown in Figure 6. 10(b), M_2B (M = Fe, Cr) is confirmed as the main hard phase in the eutectic. Figure 6.10(c) confirms the large misorientation in the martensite of the prior austenite regions of the eutectic. Enrichment of B and Cr, and depletion of Fe are clearly visible in the EDX maps of the eutectic, shown in Figure 6.10(d) and (e).

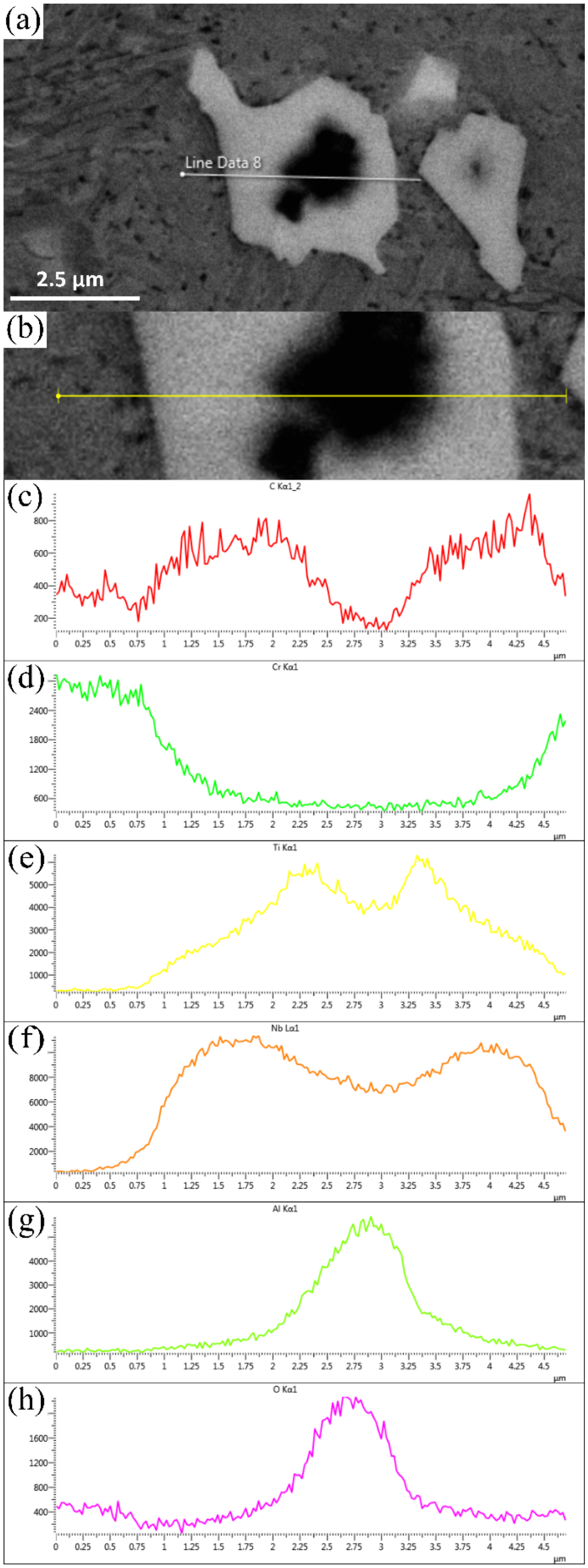

Figure 6.9: SEM backscattered electron (BSE) image of Wire 2 overlay, showing MX-type particles (a), and corresponding line-scan (b) of various elements, C (c), Cr (d), Ti (e), Nb (f), Al (g) and O (h).

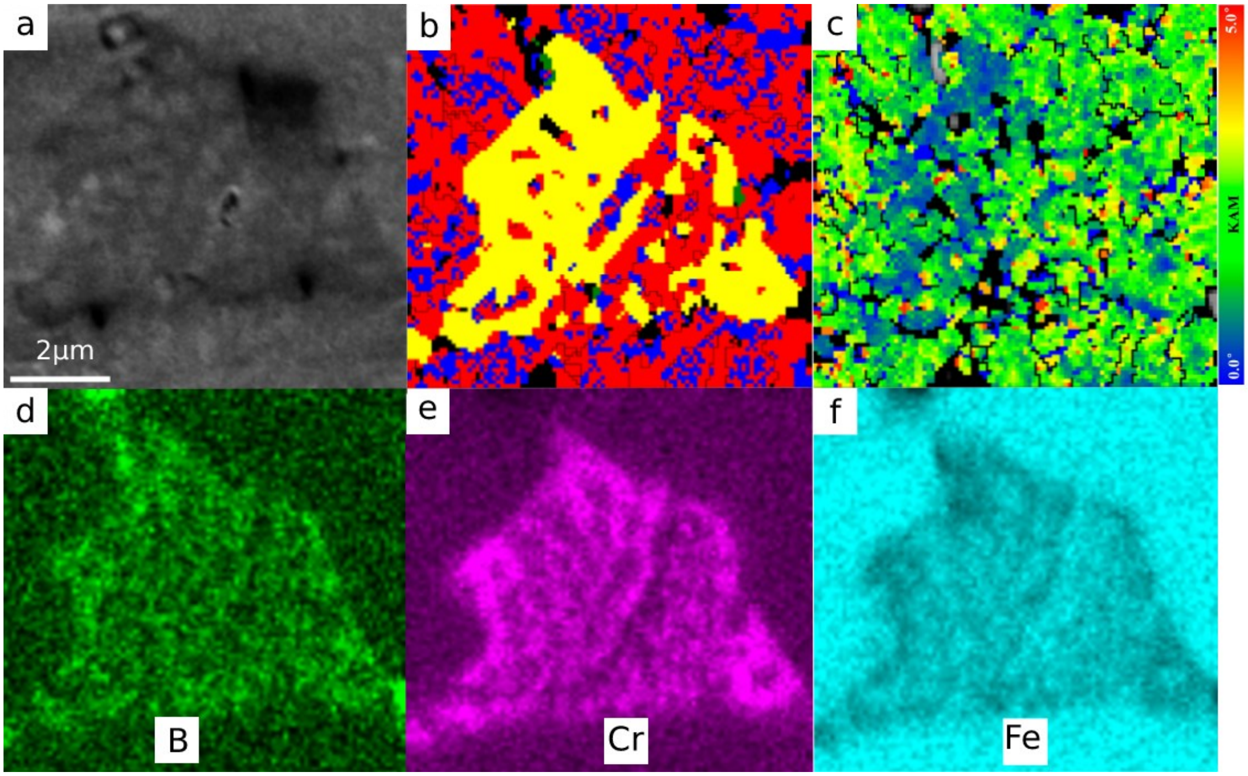

Figure 6.10: Secondary electron image of a eutectic colony in the Wire 2 overlay (a); EBSD phase map of the selected eutectic area in which red represents BCC phases. Green represents MX (Nb(C,B) and Ti(C,B)) phases, yellow represents M_2B phases, blue represents other carbides including $M_{23}C_6$ and M_7C_3, black represents non-indexed areas (b), Kernel average misorientation map (c) and (d)–(f) EDX maps of boron, chromium and iron.

6.4 Discussion

Thermo-Calc analysis of Wire 1 overlay and Wire 2 overlay is shown in Figs. 6.11 and 6.12, respectively. Compared with the new Wire 2 overlay system, the traditional overlay Wire 1 shows a simpler hypereutectic system, as shown in Figure 6.11(a). The M_7C_3 primary carbides nucleate first at 1420 °C from the liquid followed by a eutectic reaction. The eutectic reaction occurs at a narrow temperature range around 1300 °C where liquid transforms into carbide M_7C_3 and austenite (FCC_A1). Upon further cooling, an allotropic reaction at 860 °C produces a ferritic phase (i.e., if rapidly cooled, martensite phase) from austenite.

Figure 6.11(b) shows the calculated equilibrium solidification and Scheil solidification curves of the Wire 1 overlay. In Thermo-Calc calculations, a complete mixing of all elements in liquid and solid-state diffusion of two fast diffusing elements, carbon and boron, is assumed. The Wire 1 overlay shows the formation of 32% mole fraction of primary M_7C_3 carbide and 68% mole fraction of eutectics. Some mismatch is expected between phase fractions from the equilibrium Thermo-Calc predictions and the actual phase fractions following the non-equilibrium flux cored arc welding process. The Fe-Cr-C hypereutectic system has been well studied for the last half century [108,110–112]. Most researchers have focused on the refinement of the microstructure and the control of M_7C_3 carbides [113,114]. As reported by Berns and Fischer [46], TiC and NbC carbides can reach 2500 HV and 1900 HV hardness, respectively. Nevertheless, the M_7C_3 phase only showed hardness values varied from 1190–1800 HV. Some studies [115,116] of longitudinal growth mechanisms of M_7C_3 have shown that the M_7C_3 can easily grow to over 50 microns in size. The hard and brittle primary phase can cause welding cracks and premature wear failure of the hypereutectic hardfacing.

In Wire 2 overlay, the solidification starts from 1480 °C when the MX-type primary phase (with the FCC_A1#3 crystal structure, and mole fractions of 0.48 C, 0.34 Nb, and 0.18 Ti for chemical composition) forms (Figure 6.12(a)). At 1357 °C, the δ-ferrite (with the BCC_A2 crystal structure) dendrites start to form. At 1275 °C, a peritectic reaction starts to transform the δ-ferrite and liquid to austenite (with the FCC_A1 crystal structure). By

1200 °C, all δ-ferrite has been consumed. Between 1170 °C and 1145 °C, a eutectic reaction transforms the remaining liquid to austenite and two borides (M_2B_TETR crystal structure with a chemical composition of mole fractions of 0.33 B, 0.32 Cr, 0.27 Fe, 0.07 Mo and 0.01 W and Cr_2B_ORTH crystal structure with a composition of mole fractions of 0.40 Cr, 0.33 B and 0.27 Nb). In solid state, at a temperature near 1040 °C, $M_7(C, B)_3$-type carbide starts to precipitate, and at a temperature near 938 °C, $M_{23}C_6$-type carbides start to precipitate, associated with the dissolution of Cr_2B_TETR boride and growth of Cr_2B_ORTH boride. Although the Cr_2B tetragonal to orthogonal phase transformation mechanism is not clear, the total M_2B content is almost constant at about 10% mole fraction. Upon further cooling, an allotropic reaction at 840 °C produces a ferritic phase (i.e., if rapidly cooled, martensite phase) from austenite.

Scheil calculations of Wire 2 overlay shown in Figure 6.12(b) indicate a 3% mole fraction of primary carbide, 63% mole fraction of δ-ferrite and austenite, and 34% mole fraction of eutectics. This microstructure composition seems to agree with the actual micrograph in Figure 6.3(b). There are $M_{23}C_6$ and $M_7(C, B)_3$ forming and $M_{23}C_6$ dissolving at the final, eutectic, stage of liquid-to-solid transformation based on the Scheil solidification model in Figure 6.12(b), which is not predicted in the equilibrium phase calculations in Figure 6.12(a). When the δ-ferrite dendrites were forming, they engulfed the primary carbide particles, as shown by the distribution of the primary carbides within the δ-ferrite/austenite dendritic regions (Figure 6.3(b)). It clearly shows that the eutectic distributes at the d-ferrite/austenite dendritic interfacial regions, not continuously, but in a fragmented and networked pattern. A continuous networked eutectic would have resulted in a deteriorated toughness and crack resistance.

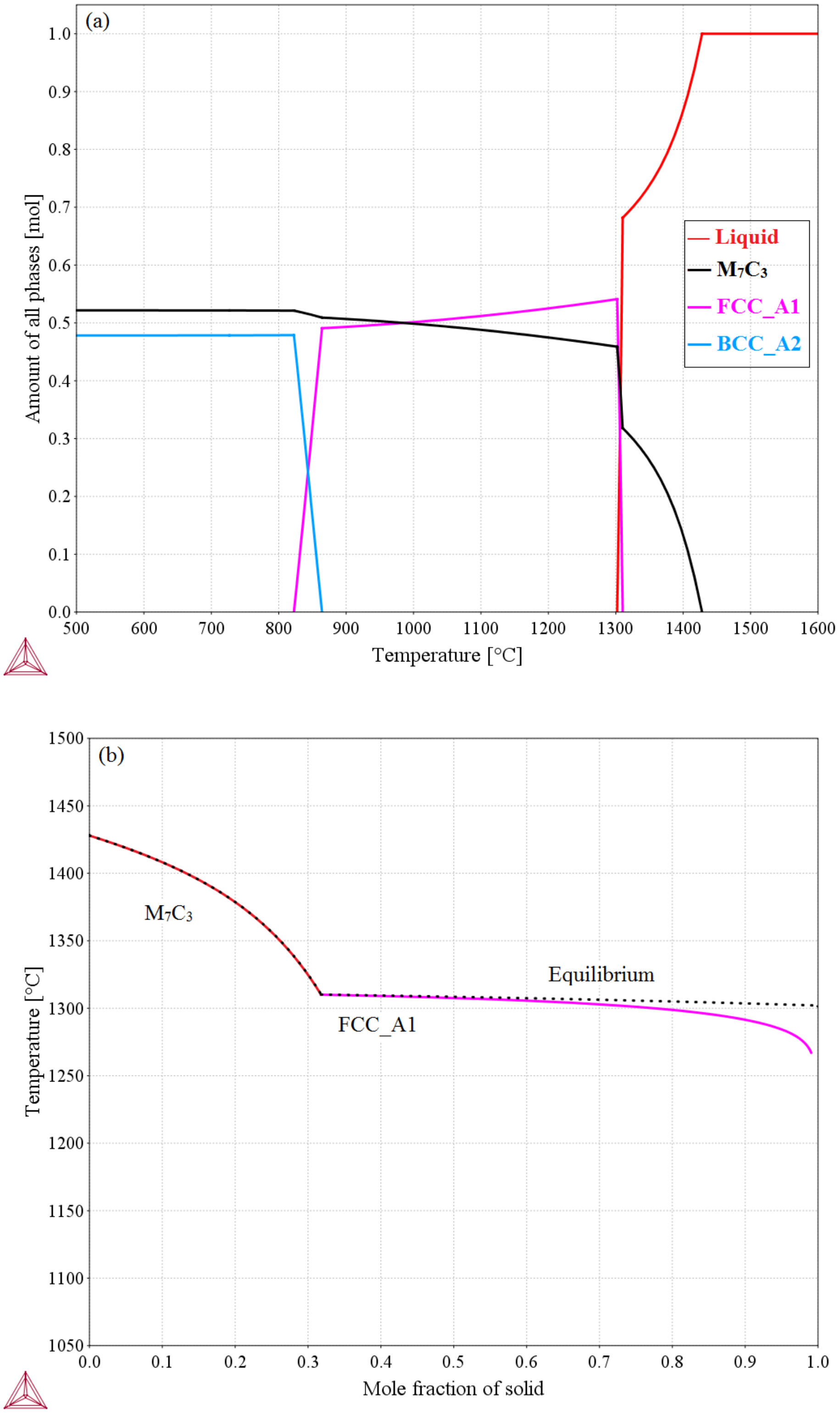

Figure 6.11: Thermo-Calc analysis of chromium carbide overlay by Wire 1. (a) Equilibrium phase constitution as a function of temperature and (b) Scheil solidification diagram.

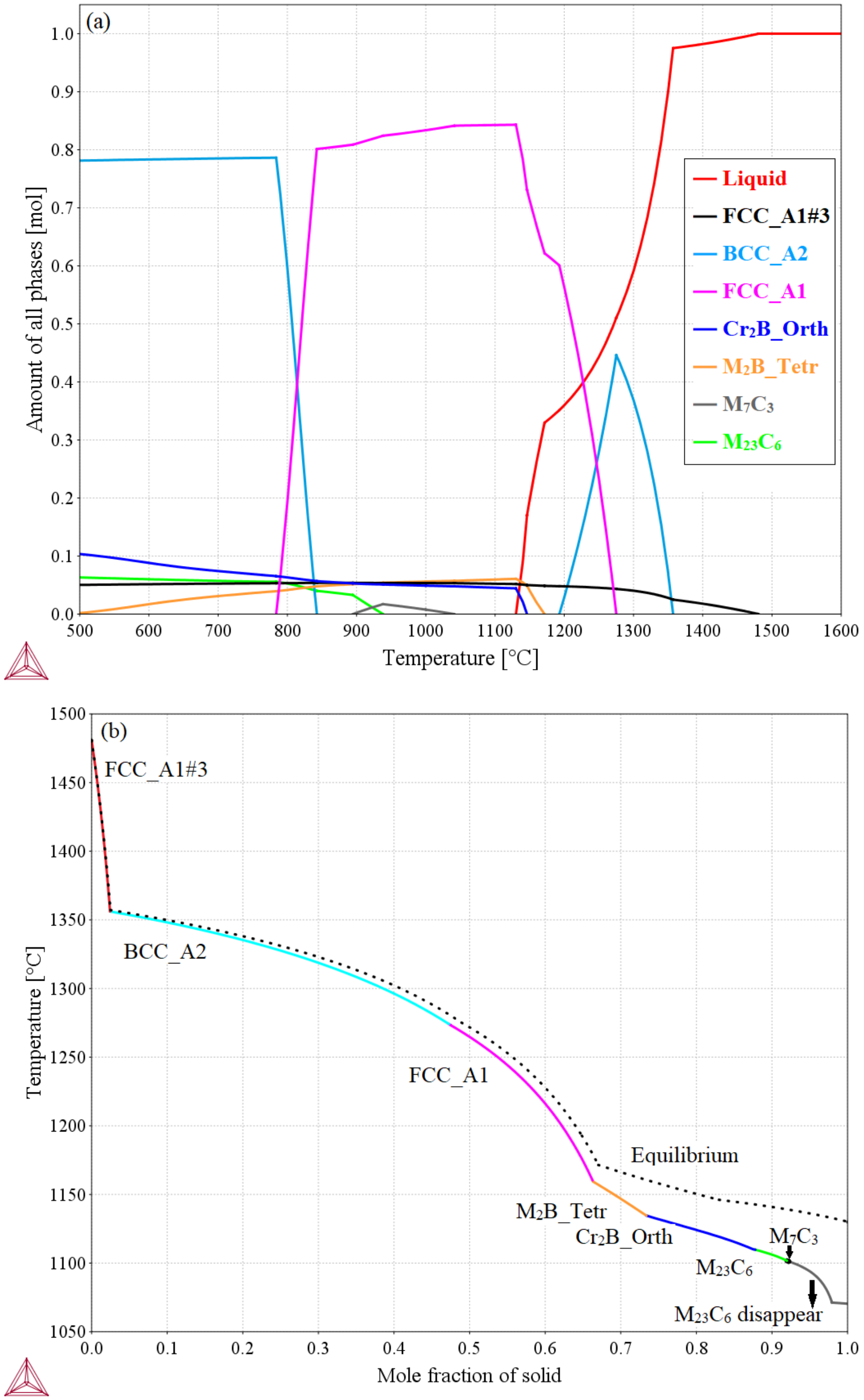

Figure 6.12: Thermo-Calc analysis of the Wire 2 overlay sample, (a) equilibrium phase constitution as a function of temperature, and (b) Scheil solidification diagram.

6.5 Conclusions

In this study, a novel Fe-Cr-C-B overlay system has been characterized and compared with conventional Fe-Cr-based chrome carbide overlays using XRD, EBSD and associated thermodynamic calculations. Results showed that the novel Fe-Cr-C-B overlay system has primary MX (M = Nb, Ti; X= C, B) type carbides/borides with a eutectic of M_2B and austenite in a martensite/retained austenite matrix. Compared with the conventional chromium carbide overlay system, where coarse M_7C_3 acts as a primary carbide, the proposed Fe-Cr-C-B overly system has a finer, harder and uniform distribution of MX primary carbides, more ductile austenitic dendrites, and a networked eutectic matrix, which may offer an improved welding crack and overlay wear resistance. The novel overlay microstructure is fully characterized as hypereutectic based on the primary carbide dendrites; paradoxically, it can also be considered hypoeutectic based on the solidification of primary δ-ferrite/austenitic dendrites. These conclusions are mostly based on thermodynamics analysis; the significant effect of welding parameters, and associated chemical kinetics, including oxidation loss of alloying elements during welding, will need to be further quantified.

Chapter 7

Aluminum Inoculated Overlay Microstructure for Enhanced Scratch Resistance

7.1 Introduction

Chromium carbide overlay has been widely used in oil and gas, mining, and agriculture applications to enhance wear resistance and component lifetime. It is generally applied by various welding methods such as submerged arc welding [98,117] and flux-cored arc welding [118]. The CCO microstructure is typically hypereutectic, consisting of primary M_7C_3 carbide and a eutectic matrix of austenite and secondary M_7C_3 carbide. M_7C_3 carbide has a hexagonal crystal structure and often grows along the zone axis [0 0 0 1] as long rods during solidification [119]. In service conditions involving high sliding and impact, the large primary M_7C_3 carbide tends to crack due to its low toughness. Such cracking sometimes results in overlay spallation that gives rise to premature failure.

Various studies have been conducted to solve the primary carbide issue. One method is to control the nucleation of the primary M_7C_3 carbides by adding pre-formed heterogeneous nucleation sites. The criterion for choosing the inoculator is that the added elements must form new phases that solidify before primary M_7C_3 carbides in the molten pool on cooling. Zhou et al [120] used a 2% Ti additive in the high chromium cast iron by forming TiC as heterogeneous nuclei to refine the M_7C_3 carbides and improved the dry wear resistance. Similarly, Liu et al [47] found that NbC could similarly refine the microstructure and improve the wear resistance. It was found that the wear loss reached the minimum when the ferroniobium was added to a large amount at 18 wt. %. Previous studies had shown that NbC and TiC were harder and more wear-resistant than the M_7C_3 carbide [46] . Besides, NbC and TiC were smaller in size (typically around 10 μm diameter) with a cuboidal shape. Even though the Nb and Ti additions could refine the microstructure, particularly the size of primary M_7C_3 carbide, they also react with carbon in the molten pool to form the more wear-resistant MC-type carbides as well as harden the matrix phase. The enhanced wear resistance is therefore contributed by two mechanisms – finer microstructure and hardening of the matrix phases. It must be noted that a hardened matrix may lead to a lower resistance to impact wear and a lower resistance to solidification cracking during the welding of the CCO. Previous work has demonstrated that the capability of deformation or the fracture toughness of the wearing material is very important in addition to hardness by second phases embedded in the matrix [121,122]. Therefore, it will be of great interest to find a method that refines the primary M_7C_3 carbides, but not introduces hardening of the matrix by the second phases.

As a common deoxidizer in welding, aluminum has been widely used to react with oxygen to form Al_2O_3 as a slag [123]. Forming at a very high temperature, the majority of Al_2O_3 slag will float up to the surface of the weld pool. Some will remain in the solidified weld as oxide inclusions with a small size (around 1 μm diameter) [124]. Few studies have been reported on the effects of aluminum addition on carbide formation. Zhi et al [125] reported the effect of aluminum on M_7C_3 in a high-chromium iron prepared by casting. It was suggested that the primary M_7C_3 was refined by aluminum addition. However, it is not clear how aluminum has changed the solidification of primary carbides and the phase transformations of the matrix. This chapter introduced a new approach to refine the primary M_7C_3 carbides by using a small amount of Al addition without introducing new hard phases. During the scratch test, it was found that large primary M_7C_3 were more easily to fracture, resulting in premature failure of the CCO. The mechanism of the refinement was further explored by two main factors, i.e., aluminum oxides act as heterogeneous nuclei, and aluminum increases of eutectic temperature. It was also found that Al suppressed the fraction of martensite in the matrix and softened the hardness. The importance of retained austenite was therefore explored.

7.2 Material and Methods

Four custom designed CCO powder mixtures were prepared with various aluminum levels, i.e., 0 wt.%, 0.1 wt.%, 0.5 wt.%, and 1.0 wt.%. Aluminum was commonly added to welding alloys for its strong deoxidation effect. However, when the aluminum content was too high in the molten pool, there was a tendency to form larger aluminum oxide inclusions in the weld metal. High-carbon ferrochromium, ferromanganese, ferrosilicon, and pure iron powder were mixed with pure aluminum powder with the same baseline chemical composition containing 30 wt.% Cr, 4 wt.% C, 2 wt.% Mn, 2 wt.% Si, and balanced Fe. The button melting method using an arc furnace has proven its capability of simulating welding overlay with the benefits of controlled cooling and no dilution [126]. Before melting, the chamber was pumped to around -50 kPa vacuum, which left some air in the chamber but not too much to cause the over-oxidization of the entire sample. The four mixtures were melted in the chamber of an arc furnace (MRF Furnace, model SA-200) 5 times, after each melting, the button was flipped upside down in the hearth to obtain a uniform melting and mixing. Direct current with the tungsten electrode negative was used with an amperage of 100A, under a pure Ar shield. The electrode contact tip was positioned at approximately 6 mm from the Cu hearth, which had the cooling water running through the entire melting process. Therefore, a controlled cooling direction was established in the vertical direction through the melted button. After the samples were fully cooled down to room temperature, they were cut and mounted in epoxy for characterization.

Both the bottom surface (perpendicular to the cooling direction) and the cross-section (parallel to the cooling direction) were mounted and prepared for metallography using the method described in Chapter 2. An optical microscope (Zeiss Axio Vert. A1) and scanning electron microscope (Zeiss EVO) with EDX were used to examine the microstructures. Microhardness tests used a Wilson VH3100 hardness tester with a load of 5 gf and a dwell time of 10 s. At least 5 hardness tests were performed on each sample to obtain the average readings and the standard deviation. The overlay microstructure is typically consisting of phases with significantly different hardness, i.e., the carbides were hard, and the austenite was soft. Therefore, using a large load could eliminate the non-uniformity of the hardness measurement and lower the measurement bias.

X-ray diffraction (XRD) was performed to identify the phases of the overlay. The scanning range was from 20° to 100° with a scan rate of 2° per minute on a Rigaku Ultima IV X-ray diffractometer with a Cu Kα X-ray source. The open software Profex-BGMN [71] was used to conduct Rietveld refinement and deconvolute the peaks. A quantitative phase fraction was therefore obtained.

To test the wear-resistant properties of the overlap samples at a local micro level, a nano scratch test was performed on the samples using an Anton Paar Revetest Scratch Tester (RST3). The bottom surface of the melted overlay sample was chosen since it would be parallel to the wear surface in a real-world application. The surface was prepared by grinding, polishing, and light etching before the scratch tests. A 1 mm line was scratched 5 passes by a diamond indenter with a 20 μm tip radius, under a load of 1500 mN and at a constant speed of 5mm/min. The normal force, friction force, acoustic emission, penetration depth, and friction coefficient data were collected for each pass. After the tests, the scratch marks were examined by a Zeiss Sigma field emission scanning electron microscope (FESEM).

7.3 Results

7.3.1 Microstructure refinement

The overlay samples exhibit a hypereutectic microstructure consisting of primary M_7C_3 carbide and eutectic austenite and secondary M_7C_3 carbides (Figure 7.1). The primary carbides display a plate morphology on the cross-section parallel to the growth direction. For the 0.1 wt.% aluminum specimen in Figure 7.1(b), the width of the primary carbide plates does not show any significant changes. When the aluminum content is increased to 0.5 wt.% (Figure 7.1(c)), the width of the primary carbides shows a significant decrease. This decrease in the carbide plate width continues when aluminum is further raised to 1.0 wt.% (Figure 7.1(d)). Besides the decrease in the size of primary carbides, the eutectic phases are also refined with the increase in aluminum levels.

The microstructure of the cross-section perpendicular to the cooling direction has confirmed the same trend (Figure 7.2). Interestingly, more information about the morphology of the primary carbides has been shown beside the smaller sizes. In the 0 to 0.1 wt.% aluminum specimens, the primary carbides exhibit hexagonal cross-sections with some core-shell features, the shell being M_7C_3 primary carbides, and the core being a layered eutectic structure made of austenite and secondary M_7C_3 carbides. When the aluminum level reaches 0.5 wt.%, some "H" shaped primary carbides have formed (indicated by the H arrows). The volume fraction of "H" shaped primary carbides increased when the aluminum level reaches 1.0 wt.%. The change and control of primary carbide shapes have not been fully understood with a change of a single element. Wu et al [119] reported that using TiC could improve the morphology of M_7C_3 carbides since the disregistry by Bramfitt's theory for TiC was only 1.32%. However, the morphology changes reported in the literature are on size changes, not on the shape changes for M_7C_3 [103].

Due to the small additions of aluminum, any Al_2O_3 residual is not observable in the optical microscopy. To verify the physical presence of residual alumina in the overlay samples, higher magnification microscopy is used. As shown in Figure 7.3, the primary and eutectic M_7C_3 carbides are rich in Cr while the eutectic austenite is rich in Fe. To avoid any Al contamination during the sample preparation, no Al-containing polishing powder was used. As shown in Figure 7.3d, the aluminum-rich phases have been observed under the SEM. Due to the nature of EDX, oxygen as a light element does not show strong contrast in the EDX mapping. An EDX line scan across one of the Al-rich particles in Figure 7.3a is shown in Figure 7.4. The line scan has shown a better result with concentration peaks for Al and O across the particle, while the concentration of Cr, and Fe show a valley at the corresponding location. It suggests the particle is aluminum oxide.

A microhardness survey using Vicker’s hardness has been performed on both the bottom and the longitudinal cross-section for all four overlay samples (Figure 7.5), For a given specimen, the microhardness values taken on the bottom cross-section are always higher than that on the longitudinal cross-section. This is in agreement with the previous study [126], which verified the cooling direction and M_7C_3 carbide growth orientation for button melting. With aluminum levels increasing from 0 to 1 wt.%, the microhardness decreases on both the bottom and longitudinal cross-sections from 732 HV to 654 HV, and 669 HV to 613 HV, respectively.

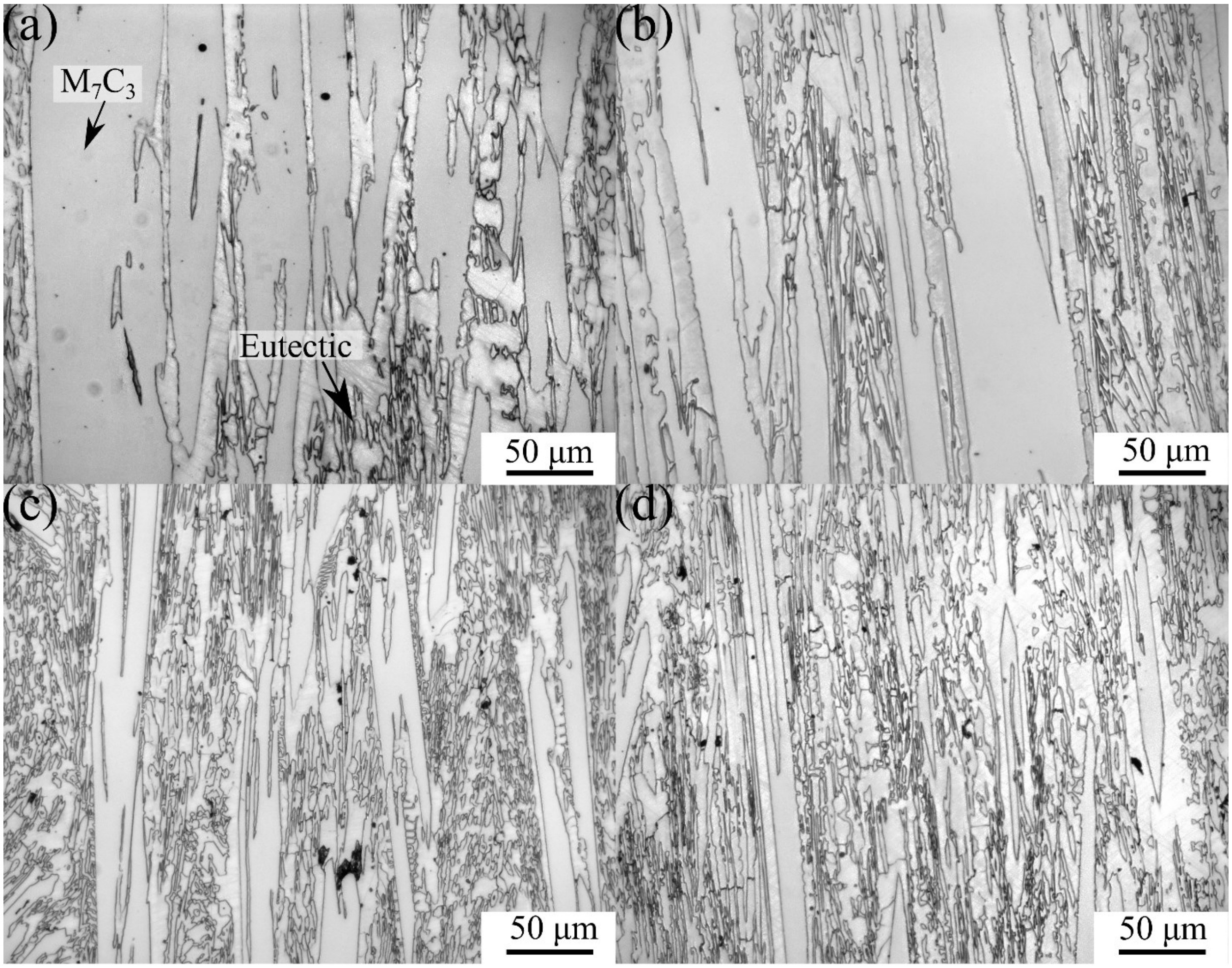

Figure 7.1: Optical microscopy of the cross-section parallel to the cooling direction of the melted overlay samples with (a) 0 wt.%, (b) 0.1 wt.%, (c) 0.5 wt.%, and (d) 1.0 wt.% aluminum.

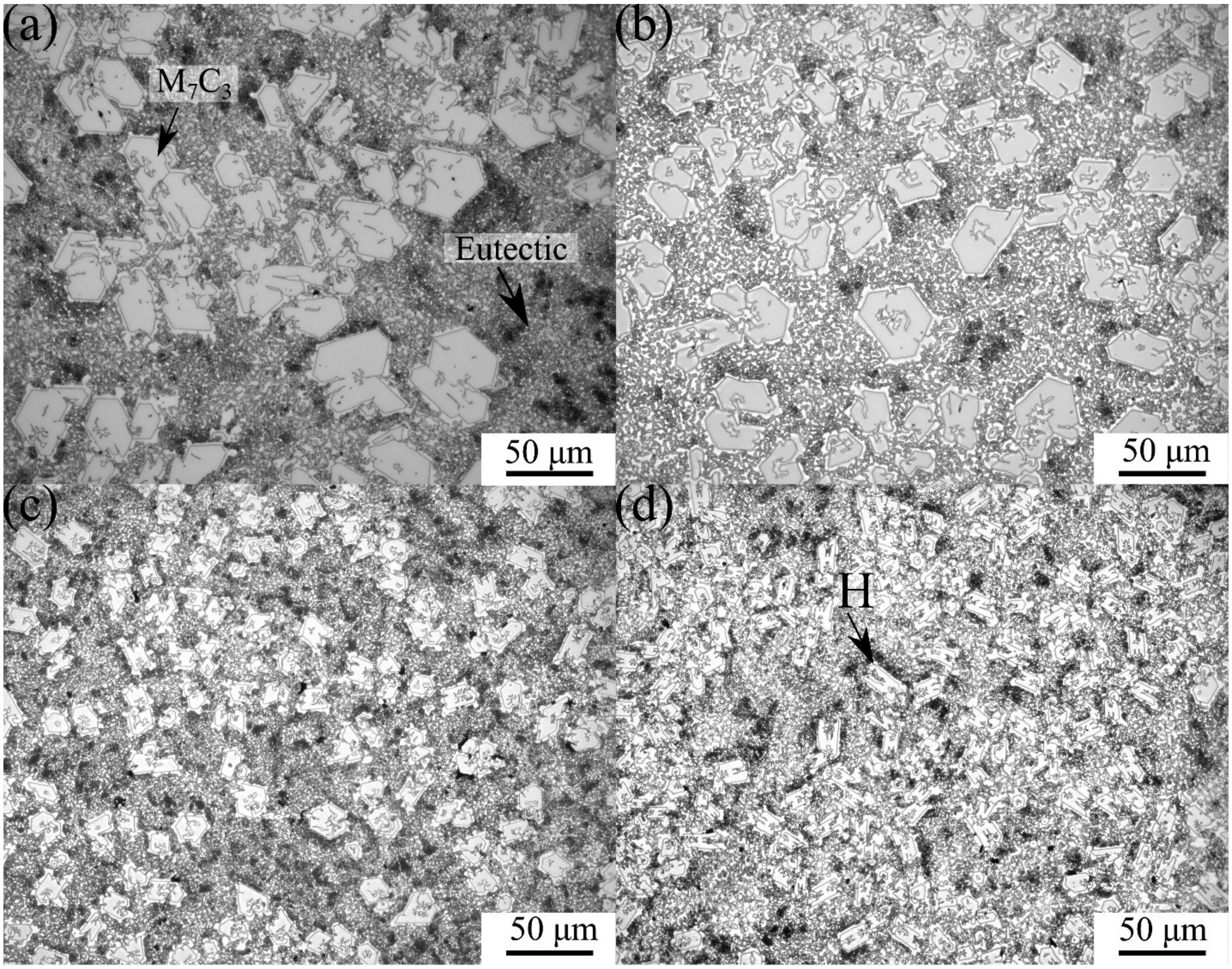

Figure 7.2: Optical microscopy of the cross-section perpendicular to the cooling direction of the melted overlay samples with (a) 0 wt.%, (b) 0.1 wt.%, (c) 0.5 wt.%, and (d) 1.0 wt.% aluminum.

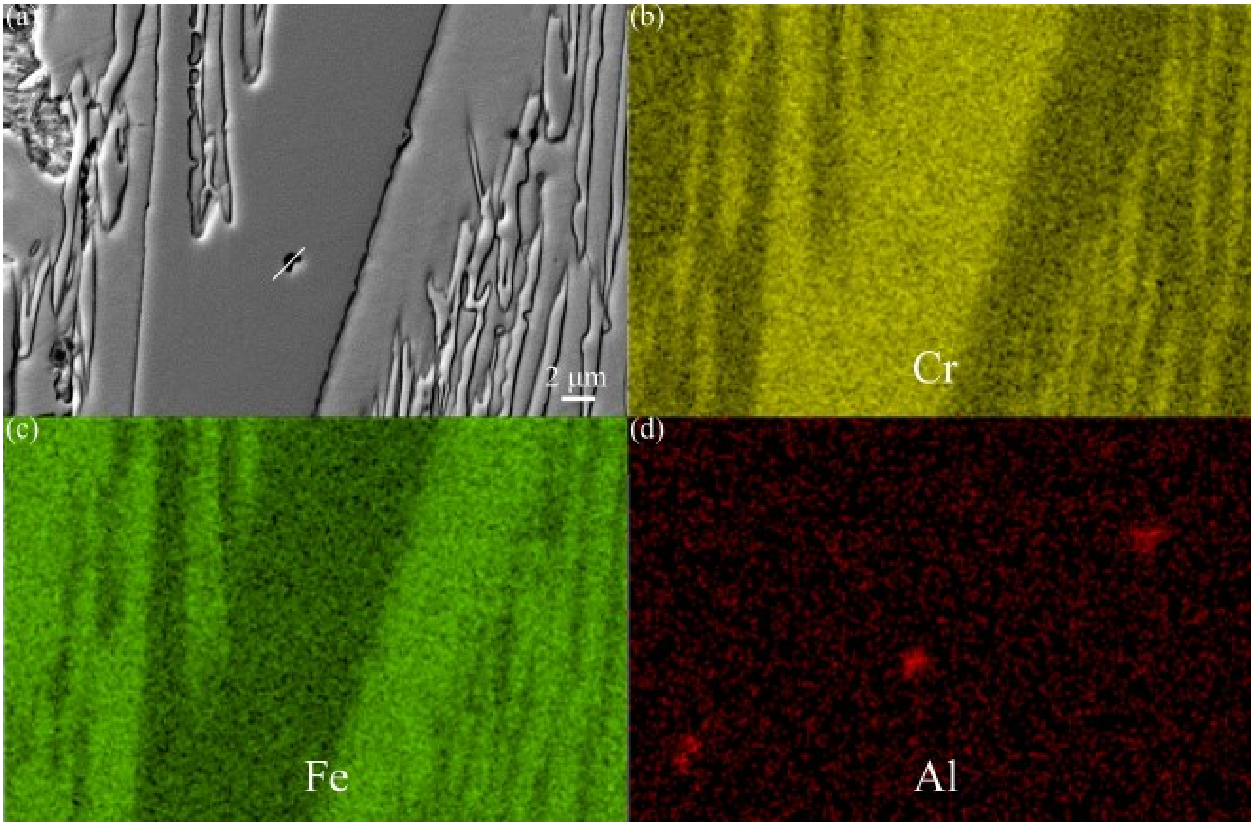

Figure 7.3: SEM/EDX images of the cross-section parallel to the cooling direction of the 0.5% Al sample. (a) secondary electron image, (b) to (d) are EDX maps for Cr, Fe, and Al, respectively.

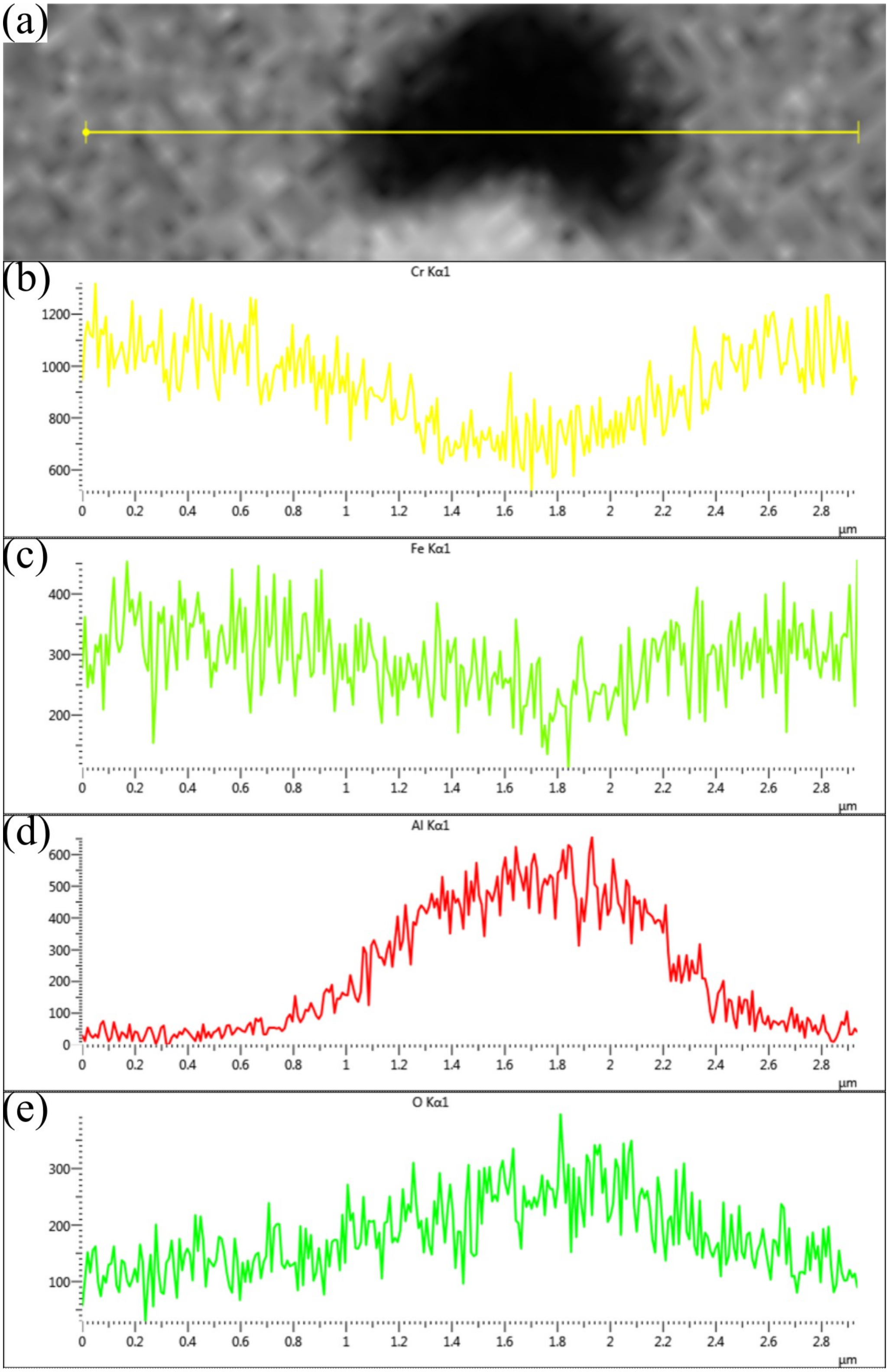

Figure 7.4: SEM/EDX line scan of the particle at the center of Figure 7.3. (a) secondary electron image, (b) to (f) are EDX line scans for Cr, Fe, Al, and O, respectively.

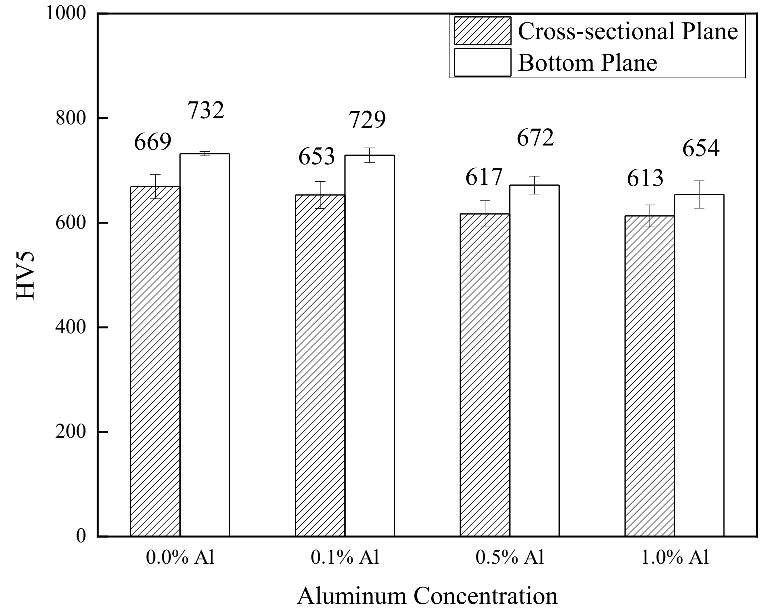

Figure 7.5: Microhardness of the four samples on the cross-section parallel to the cooling direction, and on the bottom surface (i.e., perpendicular to the cooling direction).

7.3.2. X-ray Diffraction

As shown in Figure 7.6, the main phases detected in the four overlay specimens include M_7C_3, austenite (γ), and ferrite/martensite (α/α’). Since the addition of aluminum is low, and most aluminum is expected to be lost as surface slag during melting, there is no Al_2O_3 peak detected, even for the 1 wt.% aluminum specimen. One distinction comparing the four plots is that the relative intensity of the α/α’ peak decreases with the increase of aluminum levels. The Rietveld refinement result with phase fractions is shown in Table 7.1. The phase fraction of primary Cr_7C_3 is almost unchanged at 48% for the four samples. The phase fraction of ferrite is also a constant, only varying between 4.6% and 6.6%. The retained austenite phase fraction is stable at around 35.0 % to 36.1 %, when increasing aluminum levels from 0 wt.% to 0.1 wt.%. However, a significant increase from 36.1% to

46.4% for the austenite phase fraction has been observed for the 0.1 wt.% to 0.5 wt.% aluminum specimens. Further increases in aluminum have produced a stable austenite phase fraction at 45.6%. This confirms the reported stabilization of the austenite phase in TRIP steels [127].

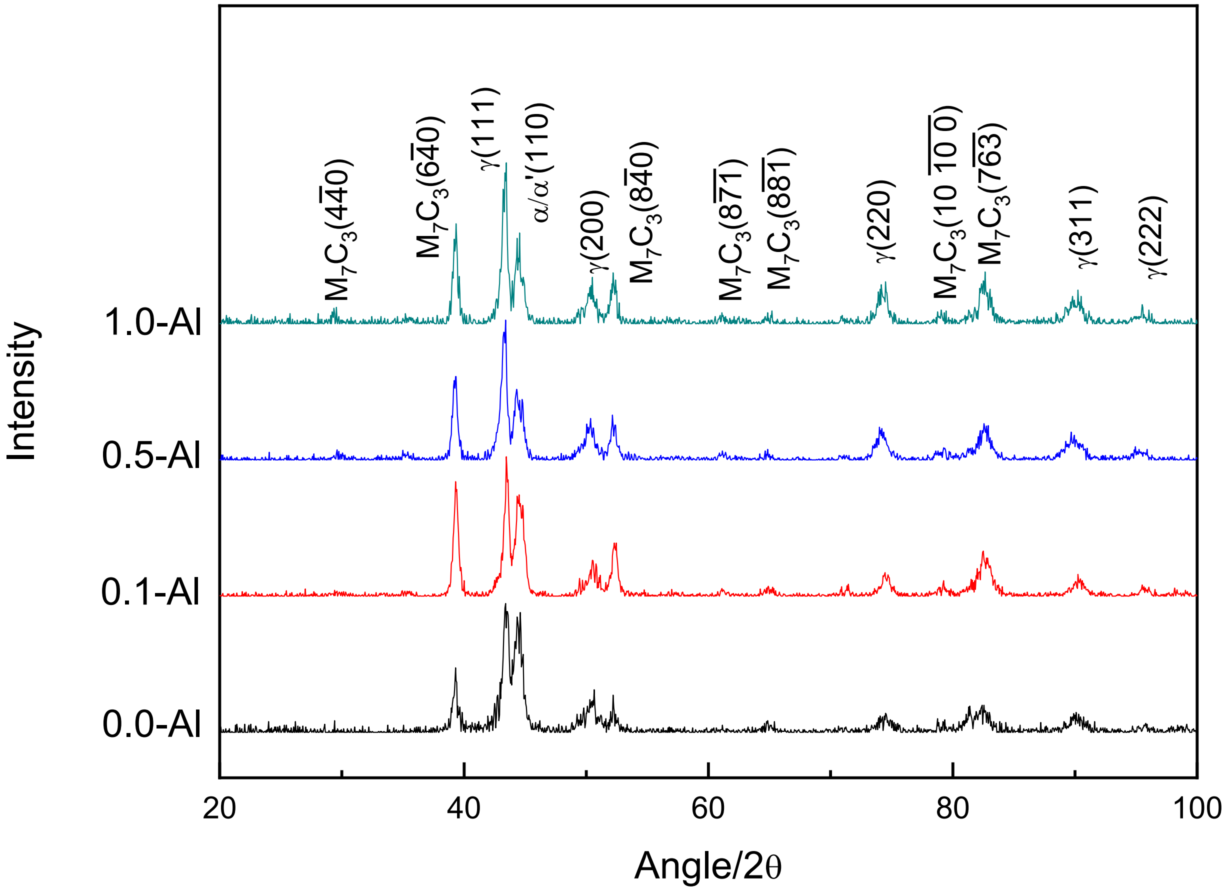

Figure 7.6: X-ray diffraction patterns of overlay samples containing 0 wt.%, 0.1 wt.%, 0.5 wt.%, and 1.0 wt.% Al. (M=Cr in M_7C_3)

Table 7.1: Phase fractions from quantitative XRD analysis.

Phase	0-Al	0.1-Al	0.5-Al	1.0 Al
Cr_7C_3	48.2%	48.6%	48.3%	48.2%
Austenite	35.0%	36.1%	46.4%	45.6%
Martensite	10.8%	8.8%	0.7%	0.5%
Ferrite	6.0%	6.6%	4.6%	5.7%

On the other hand, the martensite phase fraction in the matrix has decreased from 10.8% to 0.5% when increasing aluminum levels from 0 to 1 wt.%. Because the hard M_7C_3 phase fraction stays unchanged, a higher fraction of the soft austenite phase and a lower fraction of the martensite phase in the matrix will decrease the overall hardness of the CCO (Figure 6.5). With a 1 wt.% addition of aluminum, the martensite fraction is almost down to zero, even though fast water cooling was used during the melting and cooling.

7.3.3. Nano Scratch Test

The penetration depths as a function of scratch location in a 1 mm section for the 0 wt. % aluminum and 1 wt.% aluminum specimens have been plotted (Figure 7.7a and Figure 7.8a). The corresponding locational microstructure shown in Figure 7.7b and Figure 7.8b is stitched from a series of SEM images over the entire 1 mm length. For both samples, the indenter penetrates progressively deeper on each pass. From Pass #1 to Pass #2, the penetration depth across the entire scratch length increases nonuniformly. For example, the vertical distance between Pass #1 and Pass #2 curves at location B is larger than that at location A, meaning that at location B the penetration is deeper than location A during Pass #2. The penetration depth increases slightly slower for the subsequent passes due to strain hardening by the previous pass. One exception is the sudden peak on Pass #5 curve at 0.35 mm location as marked in Figure 7.7a. As the microstructure evidence in Figure 7.7b shows, there is a crack in the primary M_7C_3 carbide found in that location. It is believed that the crack happened during Pass #5.

Figure 7.7a, the penetration depth, can be compared with the microstructure shown in Figure 7.7b. During the first scratch pass, the lowest penetration depth for the 0 wt. % aluminum specimen is located at about 0.6 mm (location C), where a large M_7C_3 carbide is found with its hexagonal shape exposed to the wear surface. Another location with a low penetration depth is at about 0.72 mm (location D) for the same reason. The size of the carbide at location C is bigger than that at location D. This may explain why location C shows the lowest penetration depth upon the first pass. The lowest penetration depth location has shifted from location C upon Pass #3 to location D upon Pass #4. Cracking of the primary carbides is believed to have happened during the scratch tests. On the other hand, the penetration depth after 5 passes for locations A and B has become the lowest. Correlating Figure 7.7b, A and B locations contain smaller carbides and have not fractured during the tests. It results in a lower penetration and better wear resistance after 5 tests.

For the 1 wt.% aluminum specimen shown in Figure 7.8a, the range of fluctuations in the penetration depth along the scratch length is smaller compared to the 0 wt.% aluminum specimen shown in Figure 7.7a. Unlike the non-uniform depth change from Pass #1 to Pass #2 for the 0 wt.% aluminum specimen, Pass #2 penetrates deeper uniformly (for 0.4 μm) for the 1 wt.% aluminum specimen. However, the third pass only adds a small amount to the penetration depth of 0.1 μm. Very interestingly, during Pass #3 to Pass #5, the penetration depth does not grow again, meaning that not much more materials are removed by later scratches. The locations with the lowest penetration depth (E, F, G, and H) remain the lowest after 5 scratch passes. Correlating the four locations (E, F, G, and H) in Figure 7.8b, the scratch mark shows uniform microstructure, without a noticeable difference in features. This is due to the improved microstructural homogeneity with aluminum inoculation, with which, both the hard M_7C_3 phase and soft austenite phase are refined, and the variance of wear resistance is decreased.

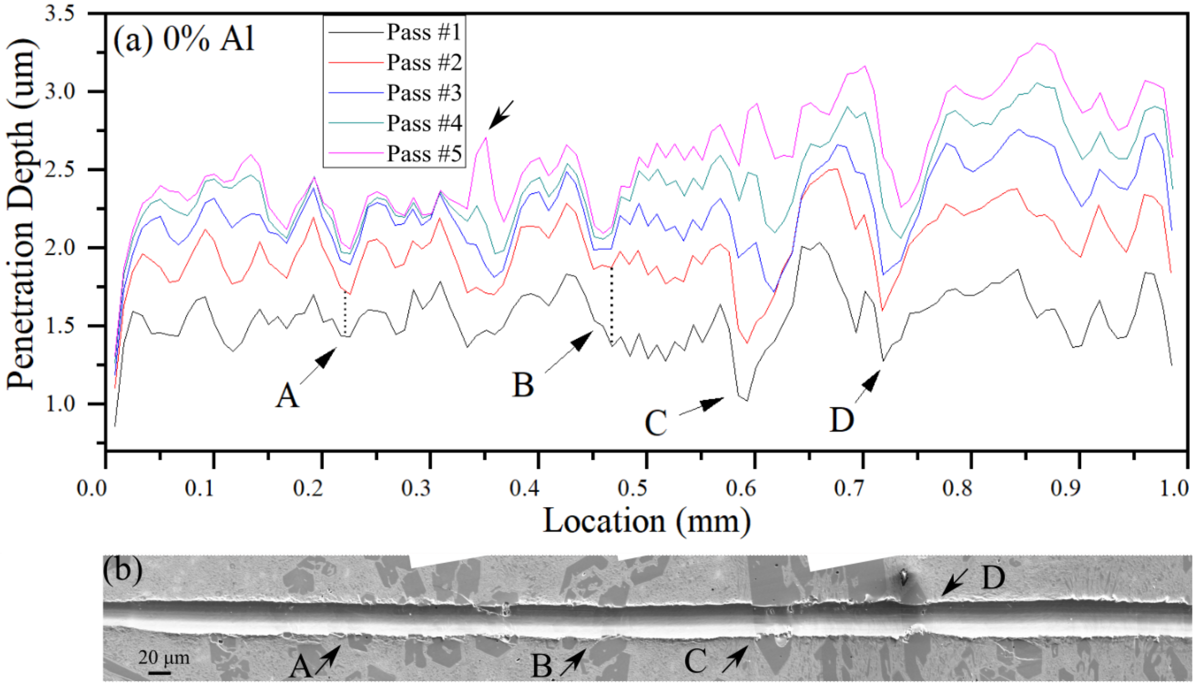

Figure 7.7: (a) Penetration depth as a function of scratch location on a 1 mm section for 0 wt.% Al sample. (b) SEM image of the corresponding 1 mm section with the scratch mark.

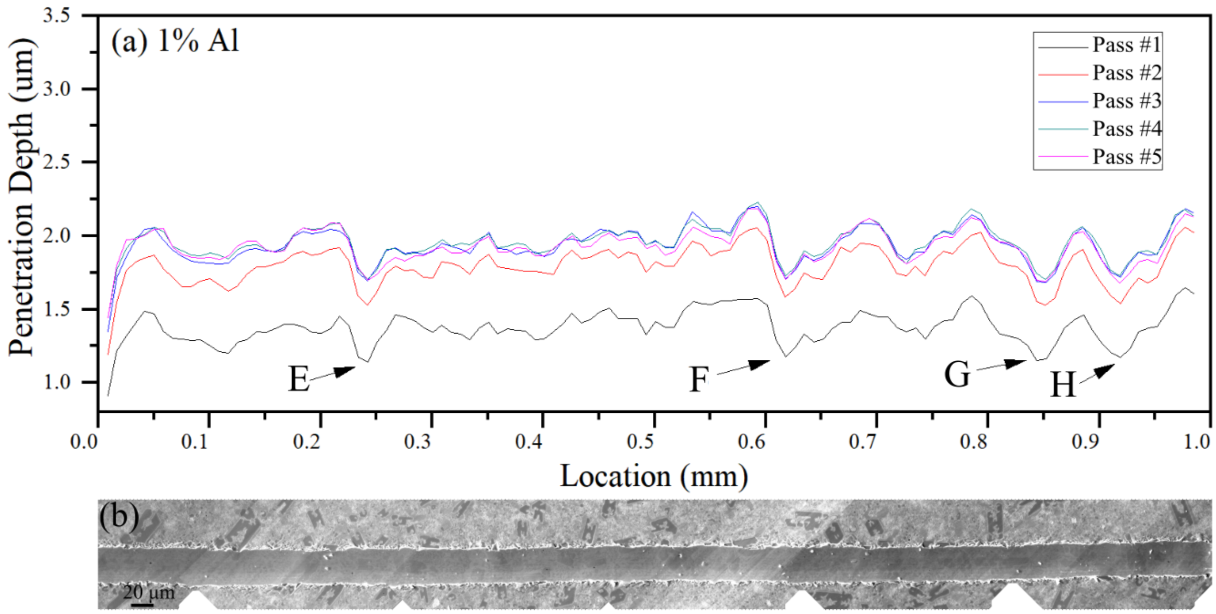

Figure 7.8: (a) Penetration depth as a function of scratch location on a 1 mm section for the 1 wt.% Al sample. (b) SEM image of the corresponding 1 mm section with the scratch mark.

The average penetration depth for both samples along the 1 mm scratch length is calculated. The average penetration depths for the 0 wt.% aluminum and 1 wt.% aluminum specimens during each scratch pass are listed in Table 7.2. Quantitatively, the test indenter penetrates 0.44, 0.25, 0.18, and 0.17 µm further upon each pass for the 0 wt.% aluminum specimen. However, the penetration depth reaches the peak value of around 1.94 µm at Pass #3 for the 1 wt.% aluminum specimen. The average penetration depth is much greater for the 0 wt.% aluminum specimen than the 1 wt.% aluminum specimen. The standard deviation shows the range of fluctuations where the 1 wt.% aluminum specimen is smaller at around 0.11 µm, while the standard deviation for the 0 wt.% aluminum specimen is twice as large. Another difference between Figures 7.7b and 7.8b is that the width of the scratch marks varies according to the local microstructure for the 0 wt.% Al.

Table 7.2: Average penetration depth (micro-meters) and standard deviation for 0 wt.% and 1 wt.% Al sample during 5 scratch passes.

		Pass #1	Pass #2	Pass #3	Pass #4	Pass #5
0% Al	Penetration Depth	1.56	2.00	2.25	2.43	2.60
	Standard deviation	0.18	0.22	0.24	0.27	0.32
1% Al	Penetration Depth	1.37	1.80	1.94	1.95	1.93
	Standard deviation	0.10	0.12	0.11	0.11	0.11

A closeup view of locations C and D in Figure 7.7 is shown in Figure 7.9. After 5 scratch passes, both carbides are broken during the scratching, and the carbide at location C has shown multiple cracks after the 5 passes. This confirms a previous study that showed the cracking of coarse tungsten carbide at a grain size of 65 – 250 µm during the wear test [22]. A close-up view of the 1 wt.% aluminum specimen in Figure 7.10 shows a uniform scratch mark. The mark has passed a few primary carbides where some wear marks start to generate. However, only very few small crack-like features have been found on the primary carbides across the entire scratch mark. A uniform microstructure allows the material to withstand the same wear condition without deteriorating the wear-resistant performance.

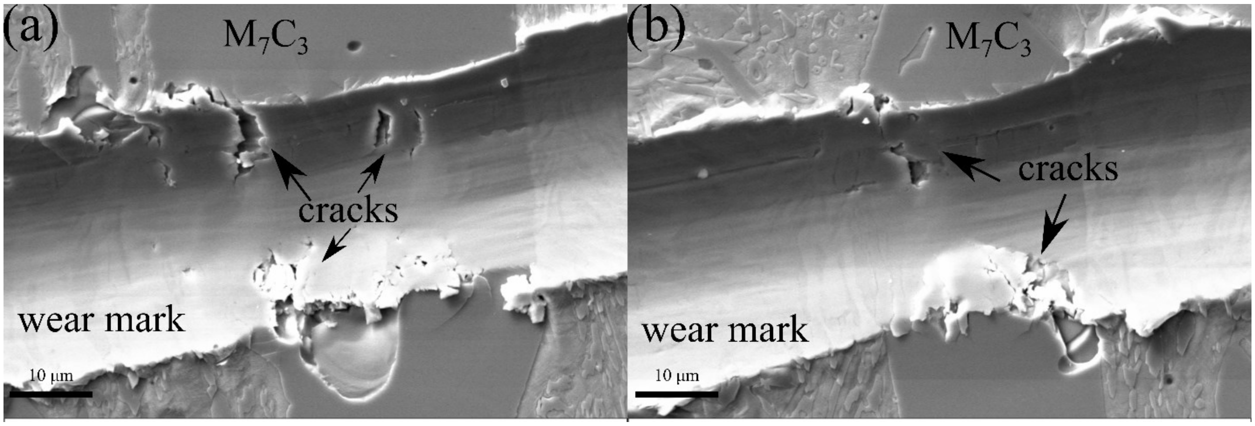

Figure 7.9: Closeup views of the 0 wt.% Al overlay sample at locations C and D as indicated in Figure 8.

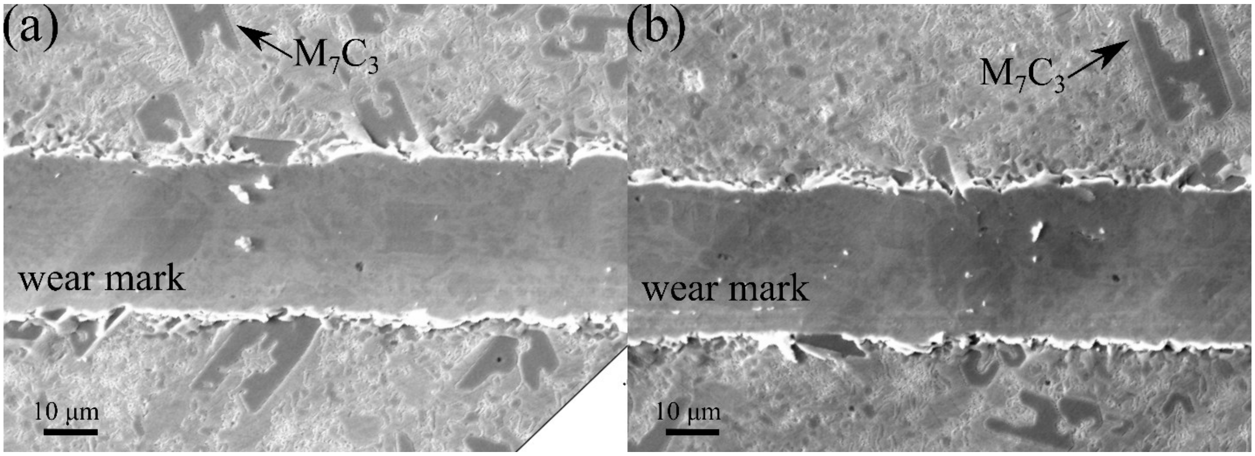

Figure 7.10: Closeup views of the 1 wt.% Al overlay sample at locations A and D as indicated in Figure 9.

The coefficient of friction (COF) for the 0 wt.% and 1 wt.% aluminum specimens is shown in Figure 7.11. For the 1 wt.% aluminum specimen, the COF decreases with more scratch passes until Pass #5, when the COF becomes stable. The COF for 0 wt.% aluminum specimen is more complicated. The average COF during each scratch pass is larger for the 0 wt.% aluminum specimen than that for the 1 wt.% aluminum specimen. The fluctuation amplitude for the 0 wt.% aluminum specimen is also larger than that for the 1 wt.% aluminum specimen, possibly due to the larger microstructural variance in the 0 wt.% aluminum specimen.

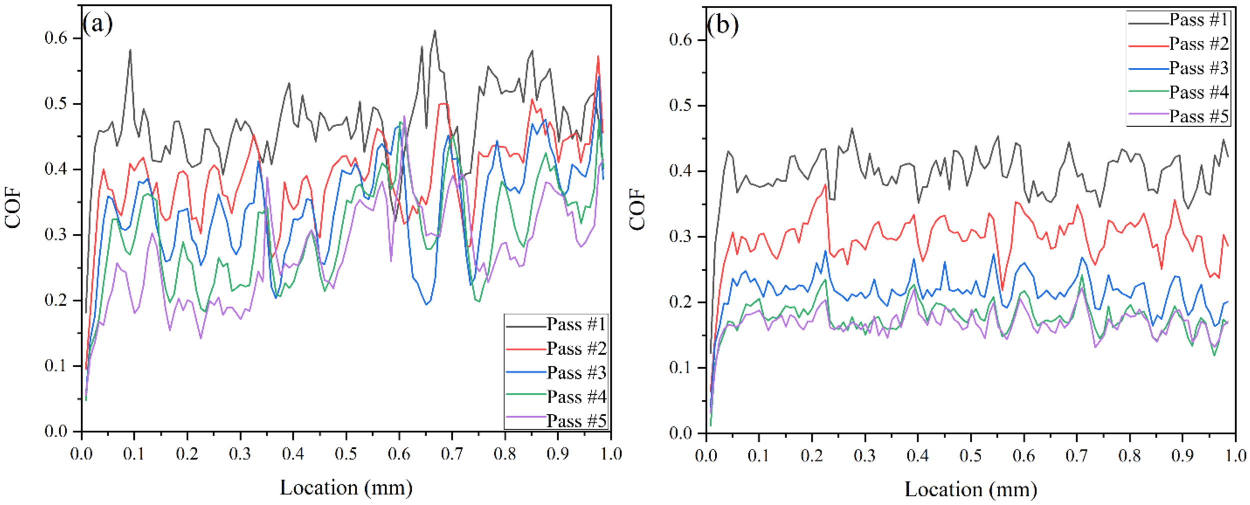

Figure 7.11: Coefficient of friction as a function of distance for (a) 0 wt.% Al sample and (b) 1 wt.% Al sample.

7.4 Discussion

The effect of aluminum on the microstructure of the chromium carbide overlay can be discussed from two angles. First, aluminum reacts with oxygen in the arc environment during melting to form Al_2O_3. The formation temperature of Al_2O_3 is higher than the solidification temperature (1400 °C) of primary M_7C_3 carbide [8]. As seen in Figure 7.12, for 0.5 wt.% aluminum and oxygen containing CCO system, Al_2O_3 forms first at 2000 °C with a 0.02 mol volume. The Al_2O_3 phase remains the amount at 0.02 mol until room temperature. The primary M_7C_3 carbide as the second solid phase from the melt will form around Al_2O_3 particles. Since many Al_2O_3 particles are serving as heterogeneous nucleation sites, more numerous M_7C_3 carbide particles will nucleate and grow for a given supercooling. Previous work has shown a similar result when nanoscale $LaAlO_3$ provided heterogeneous nucleation cores for primary M_7C_3 carbide to grow [118]. Wu et al [119] reported that using TiC could improve the morphology of M_7C_3 carbides since TiC can act as effective heterogeneous nuclei of M_7C_3 carbide. The eutectic reaction, in which the remaining liquid phase transforms to austenite (FCC_A1) and secondary M_7C_3, occurs at a small temperature range of around 1300°C. Finally, the austenite phase transfers to the ferrite phase (BCC_A2) in solid-state cooling.

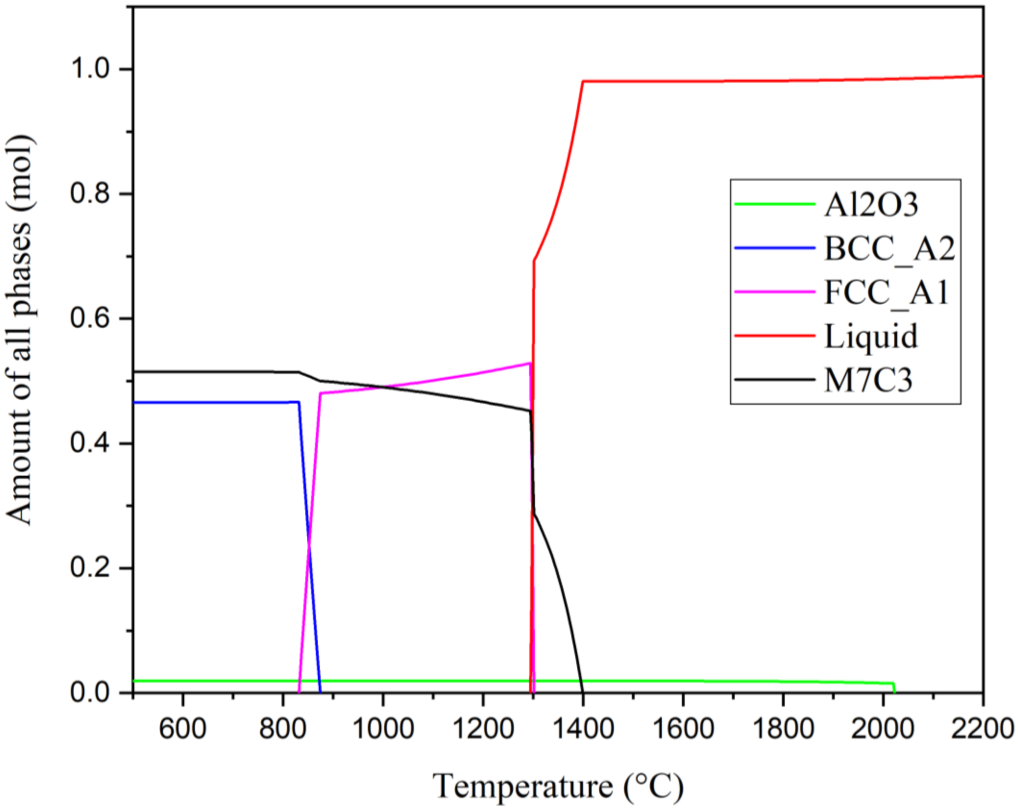

Figure 7.12: Phase vs. temperature curves by Thermo-Calc simulations of the sample containing 0.5 wt.% of Al and O.

Second, the aluminum addition raises the eutectic temperature and increases the austenite stability for the matrix. The eutectic reaction temperature can be viewed as the start of the eutectic austenite. A higher austenite temperature means a higher eutectic reaction temperature. The concentrations of aluminum in the solidified overlay are estimated as 0 wt.%, 0.01 wt.%, 0.05 wt.%, and 0.1 wt.% for Thermo-Calc calculations by considering the loss of the majority of aluminum during melting and only leaving 10% in the weld after cooling. The 10% transfer coefficient was verified for our experimental setup. As shown in Figure 7.13(a), aluminum shows some solubility in the austenite phase. On the other hand, aluminum does not show much solubility in the M_7C_3 phase as shown in Figure 7.13(a). The Gibbs free energy of the liquid, eutectic austenite, and eutectic M_7C_3 phases are shown in Figures 7.13(b) to (d). In the temperature range of 1500°C to 1200°C on cooling, a higher aluminum level decreases the Gibbs free energy, indicating that the aluminum addition would promote the formation of austenite. Therefore, the eutectic reaction is promoted to a higher temperature on cooling due to aluminum addition. The other change in the microstructure by aluminum addition is the martensitic and austenitic phase fractions. As the increase of aluminum content from 0 wt.% to 1 wt.%, the eutectic matrix has shown an increase in retained austenite fraction from 35% to over 45%. As a consequence, less martensite has been seen in the microstructure. It confirms a similar observation where an increase in the aluminum content has provided better stability of the austenite phase during fast cooling for TRIP steels [128].

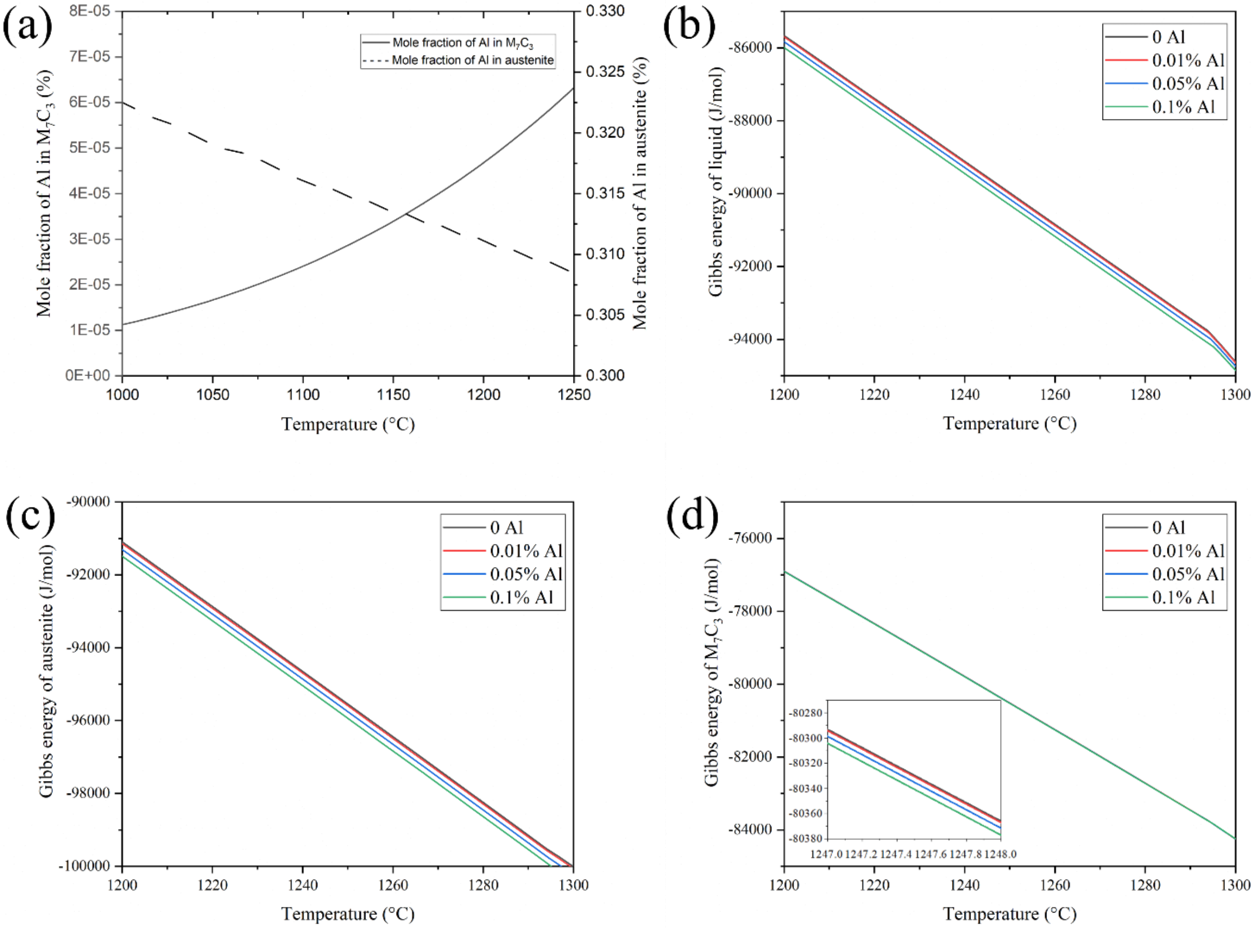

Figure 7.13: Thermo-Calc calculations of (a) mole fraction of Al in M_7C_3 and austenite phases for the sample containing 0.1 wt.% Al. (b), (c), and (d) are Gibbs free energy of the liquid, austenite, M_7C_3 for samples containing various Al levels, respectively.

Another noticeable change by the addition of aluminum is the shape of primary M_7C_3 carbides. As described previously, the addition of aluminum not only refined the M_7C_3 carbide size, but also changed the M_7C_3 carbide chape. To analyze the simultaneous effect of the M_7C_3 carbide morphology on the wear property, a mesoscale finite element model is set up in ABAQUS. Figure 7.14(a) shows a domain consisting of the ferrite matrix and an M_7C_3 carbide which contains imperfect hexagonal shape as found in Figure 7.2(a).

Another model is set up by decomposing the single hexagonal-shaped carbide into 24 smaller “H” shape Cr_7C_3 carbides while keeping the total area of the carbide the same in the domain as shown in Figure 7.14(b).

The ferrite matrix follows a bilinear hardening behaviour with an initial young’s modulus of 200 GPa and tangent modulus of 16 GPa in the hardening stage after the stress passes the yield strength of 275 MPa. Only young’s modulus of 371 GPa is used for the Hexagonal-shaped Cr_7C_3 carbide [129]. A fixed boundary condition is applied to the bottom surface and a horizontal shear deformation corresponding to 25% of shear strain is applied to the top surface. The geometry is meshed with CPS4R elements, and the von Mises stress of the carbides are shown in Figure 7.14. The maximum stress within the carbides is 7.3 ×104 MPa for the large hexagonal carbide and 2.0×104 MPa for the small “H” shape carbides, respectively. Therefore, the refined carbides would be less prone to fracture during deformation.

7.5 Conclusions

With an increased aluminum content, the microstructure of the chromium carbide overlay (CCO) is refined due to the heterogeneous nucleation of M_7C_3 on dispersed Al_2O_3. As the aluminum content increases, the overlay hardness decreases both parallel and perpendicular to the cooling direction. XRD results indicate that the addition of aluminum increases the austenite fraction and reduces the martensite fraction while maintaining the M_7C_3 and ferrite fractions almost constant.

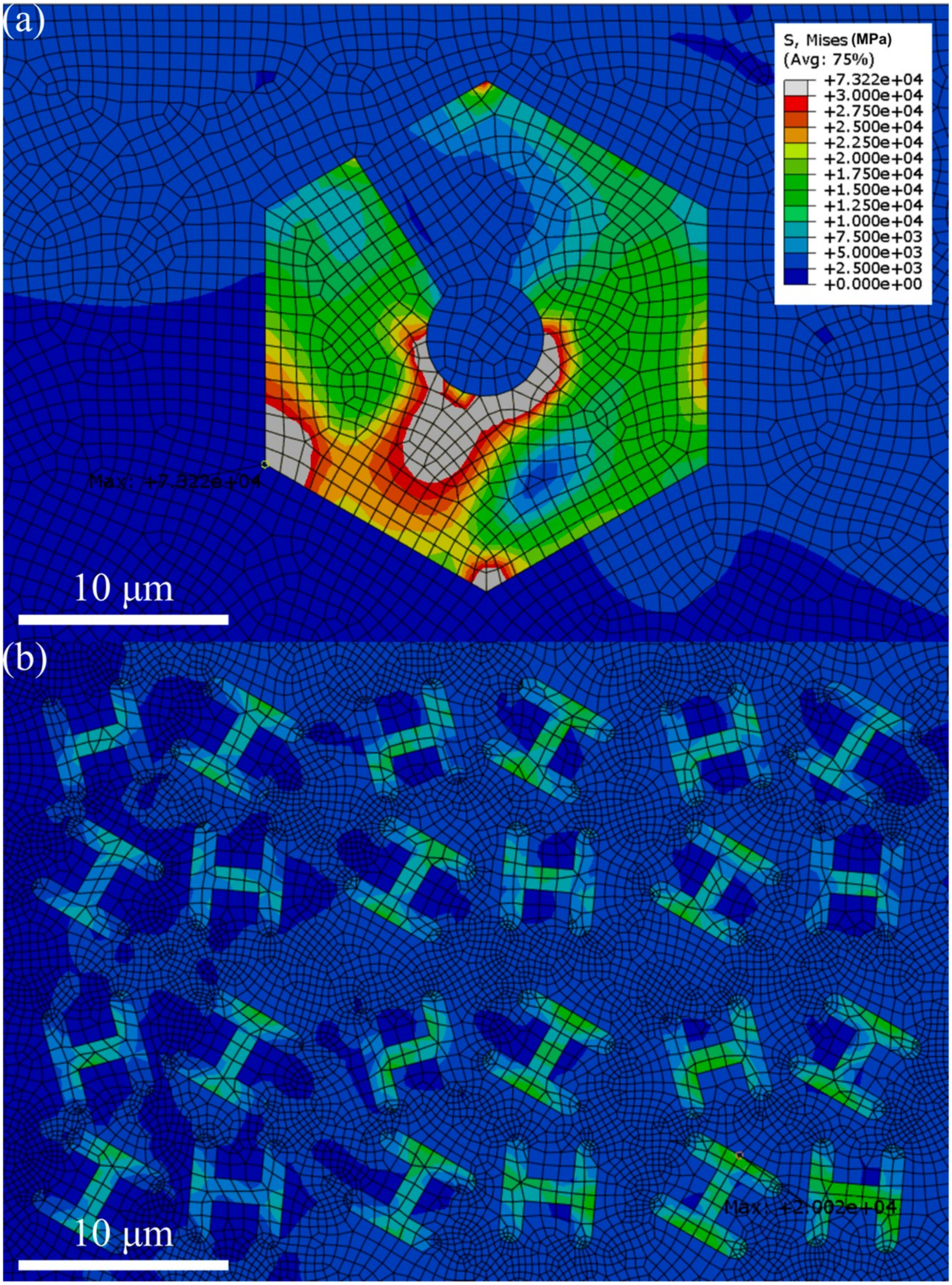

Figure 7.14: von Mises stress (MPa) distributions under 0.25 plastic strain in the large M_7C_3 carbide (a) and in the smaller “H” shape M_7C_3 carbide.

During scratch testing, the most wear-resistant areas with the presence of large M_7C_3 primary carbides became less wear-resistant as the large carbides were broken under the testing load. However, no primary carbides were broken during tests for the 1 wt.% aluminum specimen, in which the primary carbides were refined. The Al_2O_3 is believed to form first during solidification and serves as heterogeneous nucleation sites for the later formed primary M_7C_3 carbide, leading to a refined overlay microstructure.

Aluminum also stabilizes the austenite, which remains in the matrix without transforming into martensite. The retained austenite in the CCO is shown to enhance carbide fracture resistance under scratch conditions. This study presents a new approach to refine the particle size of primary M_7C_3 carbide in CCO without introducing new hard phases, allowing for the investigation of the effect of primary M_7C_3 carbide size on scratch resistance.

Chapter 8

Summary and Future Work

8.1 Summary

The main conclusions and scientific contributions of the present work on the effect of microstructure on the wear resistance of the chromium carbide overlay are summarized as follows:

Cooling condition is critical for the primary carbide distribution in the chromium carbide overlay. Little work has been done over the years to verify the effect of cooling condition on the growth of primary carbides. The predominant directional temperature gradients during arc furnace button melting results in the uniform distribution of primary M_7C_3 carbides and promotes the primary M_7C_3 carbides to orient along the temperature gradient. The arc furnace button melted sample displays higher hardness compared to the welded sample, primarily due to a greater proportion of martensite resulting from a faster cooling rate, together with more primary carbides orientated parallel to the temperature gradient. Button melting has emerged as a successful approach in the design and production of welding overlay wires, offering improved efficiency and cost-effectiveness.

As the main hard phase in the overlay, the primary carbide, its type, size, and distribution are critical to the overall wear resistance of the chromium carbide overlay. Compared to the primary M_7C_3 carbide in commercial CCO, the primary MX carbide exhibits superior properties in the CCO. The novel overlay shows a more uniform microstructure with the MX type primary carbide/boride. Unlike the commercial CCO with a eutectic M_7C_3 carbide and austenite matrix, the novel CCO contains a eutectic of M_2B and austenite. With a finer, harder, and uniform distributed MX primary phase, and more ductile austenitic dendrites and a networked eutectic matrix, it offers an improved welding crack and overlay wear resistance.

The traditional alloy design method is a time-consuming process. Machine learning has been proved to be effective to develop a model to visualize the relationship between the chemical composition input and hardness output. This model provides quantitative guidance on how the strong carbide formers contribute to the overlay hardness for a given matrix. The addition of titanium, vanadium, and niobium as carbide formers affects the overlay hardness differently. Ti addition has the most significant impact on increasing the overlay hardness, followed by V and Nb. The model is adjusted and verified using new data, establishing a closed feedback loop. The XRD analysis indicates that Nb promotes the formation of austenite in the matrix, while Ti fosters the formation of martensite, which enhances the hardness of the overlay. This approach offers a novel method for rapidly designing the chemical composition of chromium carbide overlays.

The size of primary carbides decreases as the increase of aluminum content from 0 to

1wt.%. The eutectic phases are also refined with the increase in aluminum levels. The refined microstructure has been shown to increase the resistance to scratch. In the scratch testing process, areas with high wear resistance containing large M_7C_3 primary carbides experienced a decrease in wear resistance as the large carbides fractured under the applied load. However, no primary carbides were observed to break during the tests conducted on the specimen with 1 wt.% aluminum, where the primary carbides had been refined. It is believed that Al_2O_3 disperses initially during solidification and acts as heterogeneous nucleation sites for the subsequent formation of primary M_7C_3 carbides, resulting in a more refined microstructure of the overlay. Besides, XRD results indicate that the addition of aluminum increases the austenite fraction and reduces the martensite fraction while maintaining the M_7C_3 and ferrite fractions almost constant. The presence of retained austenite in the CCO has been demonstrated to improve the resistance of carbide fracture under scratch conditions. This study introduces a novel method for refining the particle size of the primary M_7C_3 carbide in CCO, without introducing additional hard phases. This approach enables the investigation of how the size of the primary M_7C_3 carbide affects the resistance to scratching.

8.2 Future Work

Further research on chromium carbide overlay can explore several areas to advance the understanding and application of this material. Here are some potential areas for future work following this work:

Optimal composition: Investigate the effects of varying the composition of CCO, including different carbide formers and alloying elements, to identify the optimal combination for specific applications. This thesis discussed the simultaneous effect of Nb, Ti, and V on the hardness of CCO and established a machine learning model. However, the size of the input data was limited due to the scarcity of related research. Additionally, there is a lack of a quantitative model that considers a wider variety of elements and a broader range of compositions. Furthermore, the model's output should not only encompass hardness but also encompass impact toughness, wear resistance, and other mechanical properties.

Multiscale modeling: Develop advanced computational models that integrate microstructure, material properties, and loading conditions to predict the behavior and performance of CCO. This can aid in understanding the of primary carbide size, morphology, and distribution on the wear resistance of the overlay and help the design and optimization of CCO for specific applications, reducing the need for extensive experimental testing.

Bibliography

[1] G. of C.N.R.C. Canada, A strategy for tribology in Canada: enhancing reliability and efficiency through the reduction of wear and friction - NRC Publications Archive, (1987). https://nrc-publications.canada.ca/eng/view/object/?id=e4d2deb1-d0ff-4a0d-a9ff-b6747ecb187a (accessed May 14, 2023).

[2] R.B. Nair, G. Perumal, A. McDonald, Effect of Microstructure on Wear and Corrosion Performance of Thermally Sprayed AlCoCrFeMo High-Entropy Alloy Coatings, Adv. Eng. Mater. 24 (2022) 2101713. https://doi.org/10.1002/adem.202101713.

[3] A. Vardelle, C. Moreau, J. Akedo, H. Ashrafizadeh, C.C. Berndt, J.O. Berghaus, M. Boulos, J. Brogan, A.C. Bourtsalas, A. Dolatabadi, M. Dorfman, T.J. Eden, P. Fauchais, G. Fisher, F. Gaertner, M. Gindrat, R. Henne, M. Hyland, E. Irissou, E.H. Jordan, K.A. Khor, A. Killinger, Y.-C. Lau, C.-J. Li, L. Li, J. Longtin, N. Markocsan, P.J. Masset, J. Matejicek, G. Mauer, A. McDonald, J. Mostaghimi, S. Sampath, G. Schiller, K. Shinoda, M.F. Smith, A.A. Syed, N.J. Themelis, F.-L. Toma, J.P. Trelles, R. Vassen, P. Vuoristo, The 2016 Thermal Spray Roadmap, J. Therm. Spray Technol. 25 (2016) 1376–1440. https://doi.org/10.1007/s11666-016-0473-x.

[4] N. Kahraman, B. Gülenç, Abrasive wear behaviour of powder flame sprayed coatings on steel substrates, Mater. Des. 23 (2002) 721–725. https://doi.org/10.1016/S0261-3069(02)00075-4.

[5] B.V. Krishna, V.N. Misra, P.S. Mukherjee, P. Sharma, Microstructure and properties of flame sprayed tungsten carbide coatings, Int. J. Refract. Met. Hard Mater. 20 (2002) 355–374. https://doi.org/10.1016/S0263-4368(02)00073-2.

[6] A.B. Elshalakany, T.A. Osman, W. Hoziefa, A.V. Escuder, V. Amigó, Comparative study between high-velocity oxygen fuel and flame spraying using MCrAlY coats on a 304 stainless steel substrate, J. Mater. Res. Technol. 8 (2019) 4253–4263. https://doi.org/10.1016/j.jmrt.2019.07.035.

[7] J. Li, Y. Wang, Z. Lyu, N. Sharma, S.D. Choudhury, L. Li, Fracture of Ni-Cr-Si-B thermal sprayed and fused reciprocating pump rods during straightening, Eng. Fail. Anal. 127 (2021) 105576. https://doi.org/10.1016/j.engfailanal.2021.105576.

[8] J. García, V. Collado Ciprés, A. Blomqvist, B. Kaplan, Cemented carbide microstructures: a review, Int. J. Refract. Met. Hard Mater. 80 (2019) 40–68. https://doi.org/10.1016/j.ijrmhm.2018.12.004.

[9] M. Jones, U. Waag, The influence of carbide dissolution on the erosion–corrosion properties of cast tungsten carbide/Ni-based PTAW overlays, Wear. 271 (2011) 1314–1324. https://doi.org/10.1016/j.wear.2011.01.046.

[10] M. Jones, R.J. Llewellyn, Erosion-Corrosion Assessment of Tungsten Carbide-Based Plasma-Tranferred Arc-Welded Overlays, Corrosion. 68 (2012) 026003–1. https://doi.org/10.5006/1.3683231.

[11] J.M. Tarragó, S. Dorvlo, J. Esteve, L. Llanes, Influence of the microstructure on the thermal shock behavior of cemented carbides, Ceram. Int. 42 (2016) 12701–12708.

https://doi.org/10.1016/j.ceramint.2016.05.024.

[12] H. Wang, T. Webb, J.W. Bitler, Study of thermal expansion and thermal conductivity of cemented WC–Co composite, Int. J. Refract. Met. Hard Mater. 49 (2015) 170–177. https://doi.org/10.1016/j.ijrmhm.2014.06.009.

[13] I.A. Choudhury, M.A. El-Baradie, Machinability of nickel-base super alloys: a general review, J. Mater. Process. Technol. 77 (1998) 278–284. https://doi.org/10.1016/S0924-0136(97)00429-9.

[14] E.O. Ezugwu, Z.M. Wang, A.R. Machado, The machinability of nickel-based alloys: a review, J. Mater. Process. Technol. 86 (1999) 1–16. https://doi.org/10.1016/S0924-0136(98)00314-8.

[15] M.A. Khan, K. Gupta, A study on machinability of nickel based superalloy using micro-textured tungsten carbide cutting tools, Mater. Res. Express. 7 (2020) 016537. https://doi.org/10.1088/2053-1591/ab61bf.

[16] W. Liu, D. Gao, Microstructure and wear of Ni-WC hardfacing used for steel-body PDC bits, Int. J. Refract. Met. Hard Mater. 101 (2021) 105683. https://doi.org/10.1016/j.ijrmhm.2021.105683.

[17] A. Czupryński, Microstructure and Abrasive Wear Resistance of Metal Matrix Composite Coatings Deposited on Steel Grade AISI 4715 by Powder Plasma Transferred Arc Welding Part 2. Mechanical and Structural Properties of a Nickel-Based Alloy Surface Layer Reinforced with Particles of Tungsten Carbide and Synthetic Metal–Diamond Composite, Materials. 14 (2021) 2805. https://doi.org/10.3390/ma14112805.

[18] K. Günther, J.P. Bergmann, Experimental approach to determine the impact of the droplet transfer mode on the degradation of fused tungsten carbides during GMAW, Int. J. Refract. Met. Hard Mater. 101 (2021) 105692. https://doi.org/10.1016/j.ijrmhm.2021.105692.

[19] S.D. Guest, J. Chapuis, G. Wood, P.F. Mendez, Non-wetting behaviour of tungsten carbide powders in nickel weld pool: New loss mechanism in GMAW overlays, Sci. Technol. Weld. Join. 19 (2014) 133–141. https://doi.org/10.1179/1362171813Y.0000000178.

[20] G. Fisher, T. Wolfe, K. Meszaros, The Effects of Carbide Characteristics on the Performance of Tungsten Carbide-Based Composite Overlays, Deposited by Plasma-Transferred Arc Welding, J. Therm. Spray Technol. 22 (2013) 764–771. https://doi.org/10.1007/s11666-012-9877-4.

[21] K. Günther, J.P. Bergmann, Understanding the dissolution mechanism of fused tungsten carbides in Ni-based alloys: An experimental approach, Mater. Lett. 213 (2018) 253–256. https://doi.org/10.1016/j.matlet.2017.11.088.

[22] E. Badisch, M. Kirchgaßner, Influence of welding parameters on microstructure and wear behaviour of a typical NiCrBSi hardfacing alloy reinforced with tungsten carbide, Surf. Coat. Technol. 202 (2008) 6016–6022. https://doi.org/10.1016/j.surfcoat.2008.06.185.

[23] D. Serate, C. Showalter, S. Yuen, Y. Li, 50 Years of Oilsands Operation: Comprehensive Review of Wear Materials, in: OnePetro, 2021.

https://onepetro.org/NACECORR/proceedings/CORR21/9-CORR21/D091S036R004/463941 (accessed November 28, 2021).

[24] D. Serate, N. Wang, R. Robinson, J. Liu, H. Caouette-Fritsch, S. Kompally, Optimizing Composition, Fabrication, and Inspection of Chromium Carbide Overlay (CCO) For Oil Sands Sliding and Impact Wear Applications, in: NACE International, 2017. https://www.onepetro.org/conference-paper/NACE-2017-9636 (accessed December 1, 2019).

[25] S.D. Carpenter, D.E.O.S. Carpenter, J.T.H. Pearce, The nature of stacking faults within iron-chromium carbide of the type (Fe,Cr)7C3, J. Alloys Compd. 494 (2010) 245–251. https://doi.org/10.1016/j.jallcom.2009.12.197.

[26] S.D. Carpenter, D. Carpenter, J.T.H. Pearce, XRD and electron microscope study of a heat treated 26.6% chromium white iron microstructure, Mater. Chem. Phys. 101 (2007) 49–55. https://doi.org/10.1016/j.matchemphys.2006.02.013.

[27] M. Filipovic, E. Romhanji, Z. Kamberovic, Chemical Composition and Morphology of M_7C_3 Eutectic Carbide in High Chromium White Cast Iron Alloyed with Vanadium, ISIJ Int. 52 (2012) 2200–2204. https://doi.org/10.2355/isijinternational.52.2200.

[28] S.D. Carpenter, D. Carpenter, J.T.H. Pearce, XRD and electron microscope study of an as-cast 26.6% chromium white iron microstructure, Mater. Chem. Phys. 85 (2004) 32–40. https://doi.org/10.1016/j.matchemphys.2003.11.037.

[29] F. Ernst, D. Li, H. Kahn, G.M. Michal, A.H. Heuer, The carbide M7C3 in low-temperature-carburized austenitic stainless steel, Acta Mater. 59 (2011) 2268–2276.

https://doi.org/10.1016/j.actamat.2010.11.058.

[30] S. Imurai, C. Thanachayanont, J.T.H. Pearce, K. Tsuda, T. Chairuangsri, Effects of Mo on microstructure of as-cast 28wt.% Cr–2.6wt.% C–(0–10) wt.% Mo irons, Mater. Charact. 90 (2014) 99–112. https://doi.org/10.1016/j.matchar.2014.01.014.

[31] A. Wiengmoon, J.T.H. Pearce, T. Chairuangsri, Relationship between microstructure, hardness and corrosion resistance in 20wt.%Cr, 27wt.%Cr and 36wt.%Cr high chromium cast irons, Mater. Chem. Phys. 125 (2011) 739–748. https://doi.org/10.1016/j.matchemphys.2010.09.064.

[32] J. Xie, N. Chen, J. Shen, L. Teng, S. Seetharaman, Atomistic study on the structure and thermodynamic properties of Cr7C3, Mn7C3, Fe7C3, Acta Mater. 53 (2005) 2727–2732. https://doi.org/10.1016/j.actamat.2005.02.039.

[33] A. Ganguly, V. Murthy, K. Kannoorpatti, Structural and electronic properties of chromium carbides and Fe-substituted chromium carbides, Mater. Res. Express. 7 (2020) 056508. https://doi.org/10.1088/2053-1591/ab8cf9.

[34] Y. Zhang, R. Song, Y. Wang, C. Cai, K. Wang, The stepped growth mechanisms of micro-sized hexagonal M7C3 carbides: Self-assembly shell and epitaxial-layered core, Mater. Charact. 198 (2023) 112747. https://doi.org/10.1016/j.matchar.2023.112747.

[35] K. Wieczerzak, P. Bala, R. Dziurka, T. Tokarski, G. Cios, T. Koziel, L. Gondek, The effect of temperature on the evolution of eutectic carbides and M7C3 → M23C6 carbides reaction in the rapidly solidified Fe-Cr-C alloy, J. Alloys Compd. 698 (2017) 673–684. https://doi.org/10.1016/j.jallcom.2016.12.252.

[36] A.I. Gorunov, Investigation of M7C3, M23C6 and M3C carbides synthesized on austenitic stainless steel and carbon fibers using laser metal deposition, Surf. Coat. Technol. 401 (2020) 126294. https://doi.org/10.1016/j.surfcoat.2020.126294.

[37] K. Vecchio, J.L. Cheney, Methods of selecting material compositions and designing materials having a target property, US10345252B2, 2019. https://patents.google.com/patent/US10345252B2/en (accessed September 14, 2023).

[38] J.L. Cheney, A. Castells, J. Bracci, Impact resistant hardfacing and alloys and methods for making the same, US10465269B2, 2019. https://patents.google.com/patent/US10465269B2/en?oq=10465269 (accessed September 14, 2023).

[39] D.J. Branagan, B.E. MEACHAM, W.D. Kiilunen, J.N. MILLOWAY, B.D. Merkle, Glass forming hardbanding material, US8474541B2, 2013. https://patents.google.com/patent/US8474541B2/en?oq=8474541 (accessed September 14, 2023).

[40] D.J. Branagan, Spray clad wear plate, US20090123765A1, 2009. https://patents.google.com/patent/US20090123765A1/en?q=(SPRAYCLADWEAR+PLATE)&oq=SPRAYCLADWEAR+PLATE (accessed September 14, 2023).

[41] D.J. Branagan, B. Meacham, Wear resistant materials, US8795448B2, 2014. https://patents.google.com/patent/US8795448B2/en?oq=+Patent+No.:+US+8%2c795%2c448+B2 (accessed September 14, 2023).

[42] P. Xu, D. Zhou, L. Li, Fiber laser welding of WC-Co and carbon steel dissimilar

materials, Weld. J. 96 (2017) 1s–10s.

[43] D.K. Dwivedi, Microstructure and abrasive wear behaviour of iron base hardfacing, Mater. Sci. Technol. 20 (2004) 1326–1330. https://doi.org/10.1179/026708304225017418.

[44] M. Ban, N. Hasegawa, Y. Ueno, H. Shinozaki, T. Aoki, H. Fukumoto, Wear Resistance Property of Hardfacing Weld Overlays Containing Metal Carbides, Tribol. Online. 7 (2012) 207–212. https://doi.org/10.2474/trol.7.207.

[45] B. Lu, J. Luo, S. Chiovelli, Corrosion and wear resistance of chrome white irons—A correlation to their composition and microstructure, Metall. Mater. Trans. A. 37 (2006) 3029–3038. https://doi.org/10.1007/s11661-006-0184-x.

[46] H. Berns, A. Fischer, Microstructure of Fe-Cr-C hardfacing alloys with additions of Nb, Ti and, B, Metallography. 20 (1987) 401–429. https://doi.org/10.1016/0026-0800(87)90017-6.

[47] D.S. Liu, Y.H. Wei, R.P. Liu, Microstructure and wear mechanism change by Nb added in slag free self-shielded flux cored wire, Sci. Technol. Weld. Join. 20 (2015) 693–701. https://doi.org/10.1179/1362171815Y.0000000056.

[48] D. Liu, M. Wu, W. Long, L. Li, P. Wei, Effect of simultaneous addition of ferroniobium and ferrotitanium on properties of hardfacing, Mater. Sci. Technol. 34 (2018) 2231–2240. https://doi.org/10.1080/02670836.2018.1524053.

[49] S. Liu, Z. Wang, Z. Shi, Y. Zhou, Q. Yang, Experiments and calculations on refining mechanism of NbC on primary M7C3 carbide in hypereutectic Fe-Cr-C alloy, J. Alloys

Compd. 713 (2017) 108–118. https://doi.org/10.1016/j.jallcom.2017.04.167.

[50] C. Zhao, X. Xing, J. Guo, Z. Shi, Y. Zhou, X. Ren, Q. Yang, Micro-properties of (Nb,M)C carbide (M = V, Mo, W and Cr) and precipitation behavior of (Nb,V)C in carbide reinforced coating, J. Alloys Compd. 788 (2019) 852–860. https://doi.org/10.1016/j.jallcom.2019.02.284.

[51] C. Zhao, Y. Zhou, X. Xing, S. Liu, X. Ren, Q. Yang, Precipitation stability and micro-property of (Nb, Ti)C carbides in MMC coating, J. Alloys Compd. 763 (2018) 670–678. https://doi.org/10.1016/j.jallcom.2018.05.318.

[52] Q. Wang, X. Li, Effects of Nb, V, and W on Microstructure and Abrasion Resistance of Fe-Cr-C Hardfacing Alloys, Weld. J. (2010) 7.

[53] C. He-Xing, C. Zhe-Chuan, L. Jin-Cai, L. Huai-Tao, Effect of niobium on wear resistance of 15%Cr white cast iron, Wear. 166 (1993) 197–201. https://doi.org/10.1016/0043-1648(93)90262-K.

[54] J.M.S. de Sousa, G.S. Gil, M. dos S. Barbosa, D.N. Garcia, M.Q. Lobato, P.C. Machado, Tribological performance under abrasive wear of Fe-Cr-C+Nb coating deposited by FCAW process, Wear. 523 (2023) 204824. https://doi.org/10.1016/j.wear.2023.204824.

[55] M.M. Arikan, H. Çimenoğlu, E.S. Kayali, The effect of titanium on the abrasion resistance of 15Cr–3Mo white cast iron, Wear. 247 (2001) 231–235. https://doi.org/10.1016/S0043-1648(00)00523-8.

[56] D. Liu, R. Liu, Y. Wei, Effects of titanium additive on microstructure and wear performance of iron-based slag-free self-shielded flux-cored wire, Surf. Coat. Technol. 207 (2012) 579–586. https://doi.org/10.1016/j.surfcoat.2012.07.078.

[57] S. Wang, Y. Li, J. Wang, T. Luo, Z. Zheng, J. Long, K. Zheng, J. Zhang, Effect of in-situ (Ti&W)C multiphase particles on three-body abrasive wear of high chromium cast iron, Mater. Chem. Phys. 295 (2023) 127161. https://doi.org/10.1016/j.matchemphys.2022.127161.

[58] A.A. Artem'ev, G.N. Sokolov, V.I. Lysak, Effect of microparticles of titanium diboride and nanoparticles of titanium carbonitride on the structure and properties of deposited metal, Met. Sci. Heat Treat. 53 (2012) 603–607. https://doi.org/10.1007/s11041-012-9442-2.

[59] A. Takeuchi, A. Inoue, Classification of Bulk Metallic Glasses by Atomic Size Difference, Heat of Mixing and Period of Constituent Elements and Its Application to Characterization of the Main Alloying Element, Mater. Trans. 46 (2005) 2817–2829. https://doi.org/10.2320/matertrans.46.2817.

[60] H. Wang, S.F. Yu, A.R. Khan, A.G. Huang, Effects of Vanadium on Microstructure and Wear Resistance of High Chromium Cast Iron Hardfacing Layer by Electroslag Surfacing, Metals. 8 (2018) 458. https://doi.org/10.3390/met8060458.

[61] F. Lapointe, S. Dallaire, Erosion and Abrasion Resistance of Boride and Carbide-Based Weld Overlays, Therm. Spray 2003 Adv. Sci. Appl. Technol. (2003) 7.

[62] J.H. Kim, K.H. Ko, S.D. Noh, G.G. Kim, S.J. Kim, The effect of boron on the

abrasive wear behavior of austenitic Fe-based hardfacing alloys, Wear. 267 (2009) 1415–1419. https://doi.org/10.1016/j.wear.2009.03.017.

[63] S. Dallaire, Slurry erosion resistance of boride-based overlays containing boride crystals oriented perpendicularly to the wearing surface, Wear. 297 (2013) 1006–1015. https://doi.org/10.1016/j.wear.2012.11.059.

[64] D.S. Liu, P. Wei, Properties of silicon-added, iron-based, slag-free, self-shielded flux-cored wire, Weld. J. 94 (2015) 351s–357s.

[65] Z. Chen, H. Fu, F. Wang, N. Yuan, J. Lin, Effect of Si on Microstructure and Wear Resistance of Hypereutectic High-Chromium Cast Iron, J. Mater. Eng. Perform. (2022). https://doi.org/10.1007/s11665-022-07475-z.

[66] C. Scandian, C. Boher, J.D.B. de Mello, F. Rézaï-Aria, Effect of molybdenum and chromium contents in sliding wear of high-chromium white cast iron: The relationship between microstructure and wear, Wear. 267 (2009) 401–408. https://doi.org/10.1016/j.wear.2008.12.095.

[67] K.F. Pinho, C. Boher, C. Scandian, Effect of molybdenum and chromium contents on sliding wear of high-chromium white cast iron at high temperature, Lubr. Sci. 25 (2013) 153–162. https://doi.org/10.1002/ls.1171.

[68] K. Shimizu, K. Kusumoto, X. Yaer, Y. Zhang, M. Shirai, Effect of Mo content on erosive wear characteristics of high chromium cast iron at 1173K, Wear. 376–377 (2017) 542–548. https://doi.org/10.1016/j.wear.2016.12.030.

[69] D. Liu, J. Wang, Y. Zhang, R. Kannan, W. Long, M. Wu, Y. Wang, L. Li, Effect of Mo on microstructure and wear resistance of slag-free self-shielded metal-cored welding overlay, J. Mater. Process. Technol. 270 (2019) 82–91. https://doi.org/10.1016/j.jmatprotec.2019.02.024.

[70] A. Hadji, K. Bouhamla, H. Maouche, Improving Wear Properties of High-Chromium Cast Iron by Manganese Alloying, Int. J. Met. 10 (2016) 43–55. https://doi.org/10.1007/s40962-015-0003-5.

[71] N. Doebelin, R. Kleeberg, Profex: a graphical user interface for the Rietveld refinement program BGMN, J. Appl. Crystallogr. 48 (2015) 1573–1580. https://doi.org/10.1107/S1600576715014685.

[72] R. Chotěborský, P. Hrabě, M. Müller, R. Válek, J. Savková, M. Jirka, Effect of carbide size in hardfacing on abrasive wear, Res. Agric. Eng. 55 (2009) 149–158. https://doi.org/10.17221/1/2009-RAE.

[73] Y. Xie, J. (Jimmy) Jiang, K.Y. Tufa, S. Yick, Wear resistance of materials used for slurry transport, Wear. 332–333 (2015) 1104–1110. https://doi.org/10.1016/j.wear.2015.01.005.

[74] S.-P. Wang, J. Xu, (TiZrNbTa)-Mo high-entropy alloys: Dependence of microstructure and mechanical properties on Mo concentration and modeling of solid solution strengthening, Intermetallics. 95 (2018) 59–72. https://doi.org/10.1016/j.intermet.2018.01.017.

[75] T.D. Anderson, M.J. Perricone, J.N. DuPont, A.R. Marder, The influence of

molybdenum on stainless steel weld microstructures, Weld. J. 86 (2007) 281S-292S.

[76] M. Balmforth, J. Lippold, A Preliminary ferritic-martensitic stainless steel constitution diagram, Weld. J. 77 (1998) 1-s.

[77] M. Balmforth, J. Lippold, A New Ferritic-Martensitic Stainless Steel Constitution Diagram, Weld. J. (2000) 339-s.

[78] N. Barnes, T. Joseph, P.F. Mendez, Issues associated with welding and surfacing of large mobile mining equipment for use in oil sands applications, Sci. Technol. Weld. Join. 20 (2015) 483–493. https://doi.org/10.1179/1362171815Y.0000000060.

[79] Ö.N. Doğan, J.A. Hawk, Effect of carbide orientation on abrasion of high Cr white cast iron, Wear. 189 (1995) 136–142. https://doi.org/10.1016/0043-1648(95)06682-9.

[80] Z.H. Wang, Q.B. Wang, L. Cui, A.D. Yang, D.Y. He, Influence of cooling rate and composition on orientation of primary carbides of Fe–Cr–C hardfacing alloys, Sci. Technol. Weld. Join. 13 (2008) 656–662. https://doi.org/10.1179/174329308X370175.

[81] R. Chotěborský, P. Hrabě, M. Müller, J. Savková, M. Jirka, Abrasive wear of high chromium Fe-Cr-C hardfacing alloys, Res. Agric. Eng. 54 (2008) 192–198. https://doi.org/10.17221/1/2008-RAE.

[82] B.B. Straumal, P. Zięba, W. Gust, Grain boundary phase transitions and phase diagrams, Int. J. Inorg. Mater. 3 (2001) 1113–1115. https://doi.org/10.1016/S1466-6049(01)00108-8.

[83] I. Konyashin, F. Lachmann, B. Ries, A.A. Mazilkin, B.B. Straumal, Chr. Kübel, L.

Llanes, B. Baretzky, Strengthening zones in the Co matrix of WC–Co cemented carbides, Scr. Mater. 83 (2014) 17–20. https://doi.org/10.1016/j.scriptamat.2014.03.026.

[84] COMSOL Multiphysics v. 6.1., COMSOL AB Stockh. Swed. (n.d.).

[85] J. Li, R. Kannan, M. Shi, L. Li, Solidified Microstructure of Wear Resistant Fe-Cr-C-B Overlays, Metall. Mater. Trans. B. (2020) Accepted. https://doi.org/DOI: 10.1007/s11663-020-01863-3.

[86] Y. Wang, L. Li, Microstructure evolution of fine-grained heat-affected zone in type IV failure of P91 welds, Weld. J. 95 (2016) 27s–36s.

[87] Z. Shi, W. Shao, L. Rao, T. Hu, X. Xing, Y. Zhou, S. Liu, Q. Yang, Effects of Y dopant on mechanical properties and electronic structures of M7C3 carbide in Fe-Cr-C hardfacing coating, Appl. Surf. Sci. 538 (2021) 148108. https://doi.org/10.1016/j.apsusc.2020.148108.

[88] A. Zikin, I. Hussainova, C. Katsich, E. Badisch, C. Tomastik, Advanced chromium carbide-based hardfacings, Surf. Coat. Technol. 206 (2012) 4270–4278. https://doi.org/10.1016/j.surfcoat.2012.04.039.

[89] B. Cao, L.A. Adutwum, A.O. Oliynyk, E.J. Luber, B.C. Olsen, A. Mar, J.M. Buriak, How To Optimize Materials and Devices via Design of Experiments and Machine Learning: Demonstration Using Organic Photovoltaics, ACS Nano. 12 (2018) 7434–7444. https://doi.org/10.1021/acsnano.8b04726.

[90] F. Häse, L.M. Roch, A. Aspuru-Guzik, Next-Generation Experimentation with Self-

Driving Laboratories, Trends Chem. 1 (2019) 282–291. https://doi.org/10.1016/j.trechm.2019.02.007.

[91] B.P. MacLeod, F.G.L. Parlane, T.D. Morrissey, F. Häse, L.M. Roch, K.E. Dettelbach, R. Moreira, L.P.E. Yunker, M.B. Rooney, J.R. Deeth, V. Lai, G.J. Ng, H. Situ, R.H. Zhang, M.S. Elliott, T.H. Haley, D.J. Dvorak, A. Aspuru-Guzik, J.E. Hein, C.P. Berlinguette, Self-driving laboratory for accelerated discovery of thin-film materials, Sci. Adv. 6 (n.d.) eaaz8867. https://doi.org/10.1126/sciadv.aaz8867.

[92] A. Borjali, K. Monson, B. Raeymaekers, Predicting the polyethylene wear rate in pin-on-disc experiments in the context of prosthetic hip implants: Deriving a data-driven model using machine learning methods, Tribol. Int. 133 (2019) 101–110. https://doi.org/10.1016/j.triboint.2019.01.014.

[93] T. Sharma, S. Maria, D.K. Dwivedi, Abrasive Wear Behaviour of Fe-30Cr-3.6C Overlays Deposited on Mild Steel, ISIJ Int. 45 (2005) 1322–1325. https://doi.org/10.2355/isijinternational.45.1322.

[94] L. Wu, Y. Wang, Z. Yan, J. Zhang, F. Xiao, B. Liao, The phase stability and mechanical properties of Nb–C system: Using first-principles calculations and nano-indentation, J. Alloys Compd. 561 (2013) 220–227. https://doi.org/10.1016/j.jallcom.2013.01.200.

[95] J.F. Shackelford, Y.-H. Han, S. Kim, S.-H. Kwon, CRC Materials Science and Engineering Handbook, 4th ed., CRC Press, Boca Raton, 2016. https://doi.org/10.1201/b18971.

[96] C.K.N. Oliveira, C.L. Benassi, L.C. Casteletti, Evaluation of hard coatings obtained on AISI D2 steel by thermo-reactive deposition treatment, Surf. Coat. Technol. 201 (2006) 1880–1885. https://doi.org/10.1016/j.surfcoat.2006.03.036.

[97] A. Gualco, H.G. Svoboda, E.S. Surian, Effect of welding parameters on microstructure of Fe-based nanostructured weld overlay deposited through FCAW-S, Weld. Int. 30 (2016) 573–580. https://doi.org/10.1080/09507116.2015.1096533.

[98] M.C. Carvalho, Y. Wang, J.A.S. Souza, E.M. Braga, L. Li, Characterization of phases and defects in chromium carbide overlays deposited by SAW process, Eng. Fail. Anal. 60 (2016) 374–382. https://doi.org/10.1016/j.engfailanal.2015.11.058.

[99] R. Zahiri, R. Sundaramoorthy, P. Lysz, C. Subramanian, Hardfacing using ferro-alloy powder mixtures by submerged arc welding, Surf. Coat. Technol. 260 (2014) 220–229. https://doi.org/10.1016/j.surfcoat.2014.08.076.

[100] T. Liyanage, G. Fisher, A.P. Gerlich, Microstructures and abrasive wear performance of PTAW deposited Ni–WC overlays using different Ni-alloy chemistries, Wear. 274–275 (2012) 345–354. https://doi.org/10.1016/j.wear.2011.10.001.

[101] J.J. Coronado, H.F. Caicedo, A.L. Gómez, The effects of welding processes on abrasive wear resistance for hardfacing deposits, Tribol. Int. 42 (2009) 745–749. https://doi.org/10.1016/j.triboint.2008.10.012.

[102] R. Arabi Jeshvaghani, E. Harati, M. Shamanian, Effects of surface alloying on microstructure and wear behavior of ductile iron surface-modified with a nickel-based alloy using shielded metal arc welding, Mater. Des. 32 (2011) 1531–1536.

https://doi.org/10.1016/j.matdes.2010.10.006.

[103] S. Liu, Y. Zhou, X. Xing, J. Wang, X. Ren, Q. Yang, Growth characteristics of primary M7C3 carbide in hypereutectic Fe-Cr-C alloy, Sci. Rep. 6 (2016) 32941. https://doi.org/10.1038/srep32941.

[104] L. Ma, C. Huang, J. Jiang, R. Hui, Y. Xie, Z.-S. Liu, Cracks formation and residual stress in chromium carbide overlays, Eng. Fail. Anal. 31 (2013) 320–337. https://doi.org/10.1016/j.engfailanal.2013.01.050.

[105] K. Van Acker, D. Vanhoyweghen, R. Persoons, J. Vangrunderbeek, Influence of tungsten carbide particle size and distribution on the wear resistance of laser clad WC/Ni coatings, Wear. 258 (2005) 194–202. https://doi.org/10.1016/j.wear.2004.09.041.

[106] S.D. Borle, I. Le Gall, P.F. Mendez, Primary chromium carbide fraction control with variable polarity SAW, Weld. J. 94 (2015) 1s–7s.

[107] M.H. Amushahi, F. Ashrafizadeh, M. Shamanian, Characterization of boride-rich hardfacing on carbon steel by arc spray and GMAW processes, Surf. Coat. Technol. 204 (2010) 2723–2728. https://doi.org/10.1016/j.surfcoat.2010.02.028.

[108] J.T.H. Pearce, Examination of M7C3 carbides in high chromium cast irons using thin foil transmission electron microscopy, J. Mater. Sci. Lett. 2 (1983) 428–432. https://doi.org/10.1007/BF00723685.

[109] T.H. North, H.B. Bell, Slag/Metal Interaction, Oxygen and Toughness in Submerged Arc Welding, Weld. J. (1978) 63-s.

[110] J. Singh, J. Mazumder, Microstructure and wear properties of laser clad Fe−Cr−Mn−C alloys, Metall. Mater. Trans. A. 18 (1987) 313–322. https://doi.org/10.1007/BF02825712.

[111] H. Berns, Comparison of wear resistant MMC and white cast iron, Wear. 254 (2003) 47–54. https://doi.org/10.1016/S0043-1648(02)00300-9.

[112] G.L.F. Powell, Solidification of Undercooled Bulk Melts of Fe–Cr–C, Co–Cr–C and Ag–Ge Alloys of Near-Eutectic Composition, Mater. Trans. JIM. 31 (1990) 110–117. https://doi.org/10.2320/matertrans1989.31.110.

[113] L.-E. Svensson, B. Gretoft, B. Ulander, H.K.D.H. Bhadeshia, Fe-Cr-C hardfacing alloys for high-temperature applications, J. Mater. Sci. 21 (1986) 1015–1019. https://doi.org/10.1007/BF01117388.

[114] C.-M. Chang, Y.-C. Chen, W. Wu, Microstructural and abrasive characteristics of high carbon Fe–Cr–C hardfacing alloy, Tribol. Int. 43 (2010) 929–934. https://doi.org/10.1016/j.triboint.2009.12.045.

[115] N. Barnes, S. Clark, S. Seetharaman, P.F. Mendez, Growth mechanism of primary needles during the solidification of chromium carbide overlays, Acta Mater. 151 (2018) 356–365. https://doi.org/10.1016/j.actamat.2018.03.050.

[116] S. Ma, J. Xing, Y. He, Y. Li, Z. Huang, G. Liu, Q. Geng, Microstructure and crystallography of M7C3 carbide in chromium cast iron, Mater. Chem. Phys. 161 (2015) 65–73. https://doi.org/10.1016/j.matchemphys.2015.05.008.

[117] N. Barnes, S. Borle, M. Dewar, J. Andreiuk, P.F. Mendez, 3D microstructure reconstruction of chrome carbide weld overlays, Sci. Technol. Weld. Join. 19 (2014) 696–702. https://doi.org/10.1179/1362171814Y.0000000244.

[118] J. Wang, X. Xing, Y. Zhou, S. Liu, X. Qi, Q. Yang, Formation mechanism of ultrafine M7C3 carbide in a hypereutectic Fe-25Cr-4C-0.5Ti-0.5Nb-0.2N-2LaAlO3 hardfacing alloy layer, J. Mater. Res. Technol. 9 (2020) 7711–7720. https://doi.org/10.1016/j.jmrt.2020.05.039.

[119] X. Wu, J. Xing, H. Fu, X. Zhi, Effect of titanium on the morphology of primary M7C3 carbides in hypereutectic high chromium white iron, Mater. Sci. Eng. A. 457 (2007) 180–185. https://doi.org/10.1016/j.msea.2006.12.006.

[120] Y. Zhou, Y. Yang, J. Yang, F. Hao, D. Li, X. Ren, Q. Yang, Effect of Ti additive on (Cr, Fe)(7)C-3 carbide in arc surfacing layer and its refined mechanism, Appl. Surf. Sci. 258 (2012) 6653–6659. https://doi.org/10.1016/j.apsusc.2012.03.101.

[121] K.H.Z. Gahr, Microstructure and Wear of Materials, in: Tribol. Ser., Elsevier, 1987: pp. v–vi. https://doi.org/10.1016/S0167-8922(08)70718-1.

[122] K.-H.Z. Gahr, Wear by hard particles, Tribol. Int. 31 (1998) 587–596. https://doi.org/10.1016/S0301-679X(98)00079-6.

[123] M.A. Quintana, J. McLane, S.S. Babu, S.A. David, Inclusion Formation in Self-Shielded Flux Cored Arc Welds, Weld. J. April (2001) 91-s-97-s.

[124] S.S. Babu, S.A. David, Inclusion Formation and Microstructure Evolution in Low

Alloy Steel Welds., ISIJ Int. 42 (2002) 1344–1353. https://doi.org/10.2355/isijinternational.42.1344.

[125] X. Zhi, Y. Han, J. Lui, Effect of aluminum on the primary carbides of a hypereutectic high chromium cast iron, Mater. Werkst. 46 (2015) 33–39. https://doi.org/10.1002/mawe.201400258.

[126] J. Li, R. Kannan, M. Shi, Z. Lyu, L. Li, Viability of button melting for accelerated development of chromium carbide overlay, Mater. Lett. 278 (2020) 128455. https://doi.org/10.1016/j.matlet.2020.128455.

[127] A. El-Sherbiny, M.K. El-Fawkhry, A.Y. Shash, T. El-Hossany, Replacement of silicon by aluminum with the aid of vanadium for galvanized TRIP steel, J. Mater. Res. Technol. 9 (2020) 3578–3589. https://doi.org/10.1016/j.jmrt.2020.01.096.

[128] E. Jimenez-Melero, N.H. van Dijk, L. Zhao, J. Sietsma, S.E. Offerman, J.P. Wright, S. van der Zwaag, The effect of aluminium and phosphorus on the stability of individual austenite grains in TRIP steels, Acta Mater. 57 (2009) 533–543. https://doi.org/10.1016/j.actamat.2008.09.040.

[129] M. Shi, M. Di, J. Zhang, R. Kannan, J. Li, X. Yuan, L. Li, Effect of Initial Microstructure on the Toughness of Coarse-Grained Heat-Affected Zone in a Microalloyed Steel, Materials. 14 (2021) 4760. https://doi.org/10.3390/ma14164760.

Appendix: Machine Learning Algorithms

Below shows the detailed programs for the model.

```
import pandas as pd
import numpy as np
import matplotlib.pyplot as plt
import matplotlib as mpl
from sklearn.pipeline import Pipeline
from sklearn.preprocessing import StandardScaler
from sklearn.linear_model import LinearRegression
from sklearn import svm
from sklearn.preprocessing import PolynomialFeatures
from sklearn.model_selection import GridSearchCV



import plotly.figure_factory as ff
from plotly.offline import plot

# Get data
df = pd.read_csv('/Users/Bing/Downloads/hardness-average.csv')

# Add color labels to the data

colors = plt.cm.tab20(np.linspace(0,1,20)[0:len(df.label.unique())])
color_dic = {label:color for label, color in zip(df.label.unique(), colors)}
df['color'] = df.label.map(color_dic)
```

```
# Machine learning fit

names = ('Nb', 'Ti', 'V')
variables = df.loc[:,names]

#Define the pipeline without specifying the PolynomialFeatures degree for the purpose
of hyperparameter tuning.
hardness_model = Pipeline([('scl', StandardScaler()),
                           ('poly', PolynomialFeatures()),
                            ('regr', LinearRegression())])

#Use GridSearchCV to identify choice for polynomial degree
param_grid = {'poly__degree':[1,2]} #define the grid of hyperparameters to try
search = GridSearchCV(hardness_model, param_grid, cv=3,
scoring="neg_root_mean_squared_error") #define the gridsearch
search.fit(variables, df.hardness) #fit gridsearch

#print some information
print('Best hyperparameter: {}'.format(search.best_params_))
print('Mean test scores: {}'.format(search.cv_results_['mean_test_score']))

#Define a pipeline tht scales the data and applies the model
hardness_model = Pipeline([('scl', StandardScaler()),
                           ('poly', PolynomialFeatures(degree =2)),
                            ('regr', LinearRegression())])

# hardness_model = Pipeline([('scl', StandardScaler()),
#                              ('clf', svm.SVR(kernel='rbf', gamma=0.01))])



# Fit the variables to the hardness
hardness_model.fit(variables, df.hardness)
```

```
# Get the predicted hardness from the model and save it to the DataFrame
df['hardness_pred'] = hardness_model.predict(variables)

df.to_csv('predict.csv')
#%%
# make a plot of the real value vs the predicted values
#print(df[['hardness', 'hardness_pred']]) # print datea

fig, ax1 = plt.subplots(1,1, clear=True,figsize=(5,4))
plt.scatter(df.hardness, df.hardness_pred)
# for label, data in df.groupby('label'):
#     plt.plot('hardness', 'harness_pred', 'o', color=data['color'].iloc[0],
#              data=data, label=label)

plt.legend()
plt.autoscale(enable=True)
plt.plot([500,700], [500,700], ls="--", c=".3")
ax1.set_ylabel('Predicted Hardness')
ax1.set_xlabel('Measured Hardness')
plt.tight_layout()


#%%

#generate synthetic data
numpy_data = np.random.rand(1000, 3)
pesudo_variables = pd.DataFrame(data = numpy_data, columns = ['Nb', 'Ti', 'V'])
#pesudo_variables['sum'] = pesudo_variables.sum(axis=1)
test_data = pesudo_variables.div(pesudo_variables.sum(axis=1), axis=0)

#Add cornor and edges
a, b = np.mgrid[0:1:20j, 0:1:20j]
```

```
mask = a+b <=1
a,b = a[mask], b[mask]
c = 1 - a -b

df_coge = pd.DataFrame({'Nb':a, 'Ti':b, 'V':c})
# add corner and edges to the synthetic data
test_data = test_data.append(df_coge)
# fit model



enthalpy = hardness_model.predict(test_data)


fig = ff.create_ternary_contour(np.array([test_data['Nb'], test_data['Ti'], test_data['V']]),
enthalpy,
                                pole_labels=['Nb','Ti','V'],
                                interp_mode='cartesian',
                                ncontours=20,
                                colorscale='Viridis',
                                showscale=True,
                                showmarkers= False)
plot(fig)



#%%


def anova(data, prop, variables):
    devi_list = []
    for var in variables:
        data_mean = data[prop].mean()
        level_mean = data.groupby(var)[prop].mean()
        devi = ((level_mean - data_mean)**2).sum()
        devi_list += [devi]
    devi_a = np.array(devi_list)
```

```
    anova = devi_a/devi_a.sum()*100

    figname = f"{prop} {', '.join(variables)}"
    plt.figure(figname + ' ANOVA', constrained_layout=True, clear=True)
    plt.bar(variables, anova)
    plt.xlabel('Variables')
    plt.ylabel(f'Contribution to {prop} (%)')
anova(df, 'hardness', names)
```